Point Defect Engineering in Germanium

by

Corentin Monmeyran

B.Sc., Mathematics and Physics,
Ecole Polytechnique, France, 2011
M.Sc., Physics,
Ecole Polytechnique, France, 2012

Submitted to the Department of Materials Science and Engineering in partial fulfillment of the requirements for the degree of

DOCTOR OF PHILOSOPHY IN MATERIALS SCIENCE AND ENGINEERING AT THE MASSACHUSETTS INSTITUTE OF TECHNOLOGY

SEPTEMBER 2016

Signature of Author:____
Department of Materials Science and Engineering
August 29, 2016

Certified by:____
Lionel C. Kimerling
Thomas Lord Professor of Materials Science and Engineering
Thesis Supervisor

Certified by:____
Anuradha M. Agarwal
Principal Research Scientist, Materials Processing Center
Thesis Supervisor

Accepted by:____
Donald Sadoway
Professor of Materials Science and Engineering
Chair, Departmental Committee on Graduate Student

Point Defect Engineering in Germanium

by

Corentin Monmeyran

Submitted to the Department of Materials Science and Engineering
on August 31, 2016, in partial fulfillment of the
requirements for the degree of
Doctor of Philosophy in Materials Science and Engineering

Abstract

In 1947, the first transistor was made of germanium, but soon silicon became the core material of computer chips because of its processability. However, as the typical dimensions of transistors are getting closer to the atomic size, the traditional approach of scaling down transistors to improve performance is reaching its limits, and other elements need to be used in conjunction with silicon. Germanium is one of the key materials to empower silicon based devices because it possesses electronic and optoelectronic properties complementary to those of silicon, among them higher carrier mobilities and a direct band gap (Γ-valley) at 1.55 µm (the telecom C-band, therefore adding new capabilities to silicon integrated microphotonics). Furthermore, good quality Ge layers can be grown epitaxially on a Si substrate, allowing a monolithic integration of devices.

However, compared to silicon, little is known about the point defects in germanium. The goal of the present doctoral work is to remedy this gap. To this end, we have used radiation (gamma rays, alpha particles, and neutrons) to controllably introduce point defects in crystalline germanium, which were then characterized by Deep-Level Transient Spectroscopy (DLTS), a technique that allows the determination of the activation energy, capture cross-section, and concentration of the said defects. By studying their electronic properties, annealing kinetics, and introduction rates, we were able to separate vacancy-containing from interstitial-containing defects and gain insight on their physical nature and formation process. We especially identified a di-interstitial defect and a tri-interstitial defect. In addition, we proved that in the case of alpha particles and neutron irradiation, the fact that defects are generated in a collision cascade influences their carrier capture rates and annealing behaviors. We have also characterized the impact of radiation on commercial germanium-on-silicon photodetectors, and showed that point defects associate with dislocations in epitaxial Ge-on-Si layers. Finally, we have investigated the passivation of midgap states by implanting germanium with fluorine, and showed how the interaction between the halogen element, the amorphous/crystalline interface during the solid phase epitaxy, and the implantation damage is key in obtaining a high performance material.

Thesis Supervisor: Lionel C. Kimerling
Title: Thomas Lord Professor of Materials Science and Engineering

Thesis Supervisor: Anuradha M. Agarwal
Title: Principal Research Scientist, Materials Processing Center

A Christelle Tassevil

Acknowledgement

A Ph.D. is a long and difficult adventure, and one does not successfully achieve it alone. I would not be where I am today without the support, the advice and the presence of the many people with whom I have been lucky to cross path. I am fortunate that they have been a part of my life and would like to express my gratitude in the following paragraphs.

First and foremost, I want to thank my thesis committee, professor Polina Anikeeva, who smoothened my transition from being a physicist by training to a full-fledged material scientist, professor Geoffrey Beach, with whom I had the chance to teach the "Electrical, Optical and Magnetic Properties of Materials" class, and my two thesis advisor, doctor Anuradha Agarwal ("Anu") and professor Lionel C. Kimerling ("Kim"). Without their time and feedback, I would not have been able to write this document. My doctoral education happened in the Electronic Materials group (EMAT) at MIT, and it was a fantastic work environment. Since the day when I met the "triumvirate" of the group, Anu, Jürgen Michel and Kim, it has been an honor to become a researcher with people that both have the highest academic standards and put the human first. Anu and Kim, my two advisors, complement each other well. Their insight on both my scientific and "soft" skills, their humanity and their benevolence is an inspiration that will drive me in my future career. At heart, a Ph.D. is an apprenticeship, and I am the proud pupil of some masters of the art.

If Kim, Jürgen and Anu are the parents of the EMAT family, then the other students, my labmates, are my siblings. Sharing my every day routine with you was always fun. We are an exceptionally collaborative laboratory and I keep being amazed by how everyone was always ready to lend a hand when something breaks, to share their thoughts when data seems to not make any sense and to suggest ways to make other people's projects better. The enthusiasm and selflessness of EMAT is invaluable and shapes the special culture of our lab. I would like to especially thank some of my closest labmates. Rodolfo Camacho, who recruited me to EMAT when I was a prospective student, and whose energy seems endless. Your optimism and eccentricity are an inspiration to always go further, and never settle in a comfortable situation. Neil Patel, with whom I have worked the closest on DLTS. Your ability with machines, your in-depth, uncompromising scientific thinking, your persistence in front of difficulties are a model for the experimental scientist I tried to become. Brian Albert, who initiated me to research when I started my Ph.D. Your dry sense of humor can illuminate even the most frustrating days in the lab. Zhaohong Han, who started his Ph.D. at the same time as me, and will graduate a within a week of my own defense. Your relaxed attitude was always refreshing. Yan Cai, Michiel Van Houtte, Vivek Singh, Vivek Raghunathan, Brian Pearson, Wei Yu, Lirong Broderick, Peter Su and Danhao Ma, thanks for all the discussions and good times that we shared in EMAT. Finally, I want to thank Lisa Sinclair, without whom the lab would not run.

EMAT is a group of people which is part of a greater community: the Department of Materials Science and Engineering (DMSE). MIT. Since my first day at MIT, I have shared most of my Cambridge experience with friends from this extended department. When I was first visiting MIT, I remember how struck I was by how enthusiastic the students were, and how much fun they were having, both inside and outside the lab. Here I have had the deepest discussion as well as the craziest parties. Brent Keller, Alex Toumar, Michelle Ehret-Sing, Dina Yuryev, Thomas Batcho, William Richards, Raffi Mardirosian, Mira D'Souza, Chris Heidelberger, Scott Grindy, Michael Campion, Brendan Smith, Olivia Hentz, Anna Turskaya, Jérôme Michon, Owen Morris, you all made my travel to the Americas much more than an academic trip. Thanks to you, it was an initiatic journey during which I discovered more than I thought I could.

The decision to cross the Atlantic and do a Ph.D. in Boston was not lightly taken, and I am indebted to many of my professors and friends that drove my thirst for knowledge and my curiosity for science and condensed matter physics. Especially determinant to my intellectual formation were professor Roca i Cabarrocas, with whom I first entered a laboratory, professor Quéré and professor Lehoucq who showed me a playful aspect of physics, behind the mathematical formalism, and professor Dalibard for his inspiring introduction to quantum physics. Furthermore, I want to thank in particular Dr. Ricardo Marino. These long discussions on physics and research on the campus of Polytechnique have been instrumental in my decision to jump ahead and pursue a doctoral formation.

In addition, I would like to acknowledge the impact on my research of my diverse collaborators. Bill O'Mara, from *Analog Device Incorporated* for providing us with some state of the art germanium photodetectors, doctor Marshall Bautz, doctor Gregory Prigozhin and doctor Catherine Grant from the MIT Kavli institute with whom I worked on the annealing of the *Chandra* CCDs, and the international team with whom I worked on the co-implantation of germanium with phosphorus and fluorine: Doctor Iain F. Crowe, from the University of Manchester, professor Russel Gwilliam, from the University of Surrey, doctor David Pastor, Mr. Hemi Gandhi and professor Michael Aziz, from Harvard university.

Not all the people without whom this Ph.D. would not have reached completion live in Boston. My family has been an important part of this adventure, even if they were physically distant. My parents, Patrick and Danièle, have always pushed me to give the best of my self and to not be afraid of difficulties. They taught me the resilience needed when things do not work out as expected. They fed my curiosity since I am a kid and I am grateful that they always gave me the resources to succeed, while always letting me free to pursue my own interests. My siblings, Cassandre and Amaury are also an important part of my well-being, and I am looking forward to spend more time with them when I return to France.

Finally, words are failing me to describe the importance of Christelle Tassevil in my life. She has always supported and encouraged my choices, even if it meant letting me go to a different continent until she could eventually join me. She made the difficult moments easier and filled the joyful periods with bliss. This thesis owes her a lot and I dedicate this work to her.

Table of Contents

Table of figures

Chapter 1. Introduction

Since the late sixties, Moore's law has been a staple of the semiconductor industry, dictating the rate of miniaturization of processor chips. However, production lines will reach the 10 nm node in 2017, and the 7 nm node is already being developed in R&D laboratories: the scaling down of transistors will soon reach a roadblock as the gate length get closer to the atomic size. Two approaches are possible to tackle this issue: using materials with better performance than silicon or shifting paradigm, i.e. using device architectures that are more efficient than the traditional metal oxide semiconductor field-effect transistors (MOSFETS). These two strategies are complementary, as using new material can enable new functionalities. Furthermore, due to the sheer price of modern semiconductor foundries, an important attribute of a new technology complementing silicon chips is the ability to blend harmoniously in industrial process flows. This criterion makes germanium a material of choice. It is fully Si-CMOS compatible, and its lattice constant is close enough to silicon's that it can be grown epitaxially on it. Germanium has good electronic properties: its electron mobility is higher than that of silicon, and its hole mobility is the highest among traditional semiconductors. It also can be used as a stressor to allow strain engineering and boost the performance of devices. As a result, commercial devices are already using SiGe alloys to make faster transistors.

In addition to its electronic usage, a very promising application for germanium is in microphotonics, which is a key technological platform to overcome the difficulties intrinsic to traditional electronics. Photonics is a device-oriented branch of optics, similar to what electronics is to the physics of electron in solids. Photons have multiple advantages over electrons for the transmission of data. Especially, in the linear regime, photons don't interact with one another. This paves the way for wavelength multiplexing, the idea of stacking signals at different wavelengths to multiply the capacity of a fiber or a waveguide. Optical fibers also have a higher bandwidth, lower latency, lower dispersion and lower loss than copper cable. Since the late eighties, copper cables has been gradually replaced by optical fibers as the price of the latter went down, starting first with long distance telecom applications (≈100 km) in the 80s, to Datacom applications (≈100 m) in the 90s, to board to board (≈1 m) communication in data center and super computers in the 2010s. Photonics penetrates homes through fiber internet connections. Nowadays, the challenge is to shrink photonic devices even more to allow cost effective chip-to-chip (≈cm) optical communication and ultimately replace the back-end metallic wiring that connect transistors to one another. Because germanium is Si-CMOS compatible and has good optoelectronic properties in the appropriate wavelength range (in particular a direct bandgap in the near infra-red, around 1.55 µm, also called the telecom C-band), it offers the possibility of a maximal monolithic integration and is therefore critical to a low cost, silicon-based microphotonic platform.

A microphotonic circuit require five major elements: a multiplexer/demultiplexer, a waveguide, a modulator, a light source and a detector. While the three first can be done out of silicon, the direct bandgap of silicon (4 eV) is too large to make a good light source and its indirect bandgap at 1.1 eV (corresponding to a wavelength of 1.1 µm) is also too high for photodetectors in the telecom C-band. On the other hand, germanium is a quasi-direct band gap semiconductor with an appropriate direct band gap energy of 0.8 eV (1.5 µm), which makes it suitable to complement silicon: in a silicon microphotonic device, the active layers are made of germanium. Ge-on-Si light sources[1], [2], detectors[3]–[5] and modulators [6], [7] have already been fabricated, with the added bonus in the case of modulators that these devices are electro-absorption based and do not need a resonant structure, making them more tolerant to temperature change and fabrication variability.

Despite germanium being the material of the first transistor in 1947, the existence of a stable native oxide in silicon which also acts as a diffusion barrier made silicon easier to process and the superior material for most applications. It became the backbone of the integrated circuit industry, quickly eclipsing germanium in term of industrial use and research effort. Due to this prevalence of silicon, the knowledge on germanium is lacking. Now that high speed electronics and microphotonics have put germanium back to the spotlight, it is time for fundamental research to be pursued. Of special interest are point defects which are, as their name suggest, zero-dimensional irregularities in the lattice of a crystal, such as vacancies, interstitials, impurities and any combination of them. They are imperfections that create states in the otherwise forbidden bandgap of a semiconductor and thus affect its properties by impacting the generation and recombination mechanisms of free carriers in the conduction and valence bands. More precisely, their most harmful effects are: reducing lifetimes (especially problematic in the case of solar cells), promoting non-radiative recombinations (decreasing the efficiency of lasers and LED), increasing leakage current of rectifying devices, and intensifying generation-recombination noises in optoelectronic detectors. However, not all point defects are harmful. By controlling their properties and promoting chosen defects, they can improve the quality of devices. For instance, oxygen impurities can act as gettering centers, removing harmful metallic impurities from the active region of devices, lifetime reducing defects can be used to increase the switching speed of diodes[8, p.], impurity band photodetectors can be created for sub-bandgap photo-absorption, and, more recently, the spin properties of point defects (especially the nitrogen-vacancy in diamond) have become the heart of quantum computing research. Defects are imperfection, but it does not mean they should be suppressed at all cost: defect engineering is a critical and necessary step toward the design of reliable high performance devices.

However, defect engineering is only possible after a thorough understanding of the point defect themselves has been reached. In silicon, "maps" of point defects, their nature, electronic signature, annealing behavior, etc. exist, but it is not the case for germanium. The object of this doctoral work is to fill this knowledge gap. To this end, we have used Deep-Level Transient Spectroscopy (DLTS). This technique extracts information of the activation energy, capture cross-section and concentration of point defects by measuring the transients of capacitance observed after pulses of voltages are applied on a reverse bias rectifying junction. In conjunction with this spectroscopy technique, we have used radiation to generate defects. This is because even if defects are always present above 0 K, their concentration in high quality material is often too small to be measured by DLTS. When irradiating particles hit a material, they can collide with the atoms and the lattice and displace them, leaving behind point defects. By varying the nature of the radiation (e.g. gamma rays, neutrons, light ions, etc.), as well as the energy and the dose, it is possible to control what defects are introduced and in what proportion, and therefore to study them in a controlled environment. This is the reason why irradiation studies are a common way to investigate the nature of defects in semiconductors. Moreover, in addition to their interest for a fundamental research on defects, irradiation studies are critical for the reliability of technologies deployed in extreme environments such as space, nuclear facilities and battlefields.

The present doctoral thesis is structured around the following parts. Chapter 2 is a methodology section. It describes Deep-Level Transient Spectroscopy (DLTS), the technique that we used to measure the electronic properties of the point defects in germanium. In addition, it explains how irradiation generates damage in a material. Chapter 3 uses DLTS to investigate the properties of point defects induced by ^{60}Co gamma rays in a Czochralski (CZ) grown germanium wafer. CZ-Ge has a low impurity content, no dislocations and nearly no native defects, making it an ideal platform to study simple defects, all the more that gamma rays only generate single displacements in germanium (self-interstitials and mono-vacancies). Chapter 4 investigates the defect generated in CZ-Ge by neutrons and alpha particles which, contrary to gamma rays, cause collision cascades and thus point defect clusters. Chapter 5 focuses on the irradiation defects on commercial germanium on silicon photodetector made by *Analog Device Inc.* The germanium of these devices is a thin film grown epitaxially on silicon and therefore contains dislocations. Moreover, the fabrication induces the formation of processing damage, resulting in a starting material containing native defects and impurities, contrary to the pristine CZ-Ge wafers. Therefore, these diodes are a good platform to both study the difference of bulk and thin film defects, as well as processing defects. Chapter 6 is a case study on how to use the point defect "map" of a material (in this case, silicon's) to solve a real life problem. More precisely, it investigates why the (silicon) CCDs of the *Chandra* spatial X-ray telescope saw a decrease of their charge transfer efficiency after an irradiation due to low energy protons in orbit, and more surprisingly why an anneal supposed to remove these defects only further aggravated the issue. Chapter 7 goes past the characterization of point defects in germanium and describes a point defect engineering strategy: leveraging the high electronegativity of fluorine to passivate the vacancies in highly doped epitaxial germanium co-implanted by phosphorus and fluorine.

Chapter 2. Methodology

I. Deep-Level Transient Spectroscopy

a) Semiconductors

A crystal is a material whose atoms are arranged in a periodic fashion (i.e. a lattice). Due to this translation symmetry along the vectors describing the periodicity, the Hamiltonian of the electrons inside a crystal also have a translation symmetry, and thus commutes with the translation operator. The eigenstates of the translation operator have the general form of a complex exponential modulated by a periodic function (in the sense of the considered translation operator). The commutation of the Hamiltonian with the translation operator means that the eigenstates of the system have to be eigenstates of both operators, which directly results in the electron wave functions having the specific form shown on Equation 1 (where k denotes the wave vector of the particular state and u_k a modulation periodic on a primitive cell of the reciprocal lattice) and are called “Bloch States”.

$$\left|\Psi_k\right\rangle(\vec{r}) = e^{i\vec{k}.\vec{r}}u_k(\vec{r}) \qquad \text{(Equation 1)}$$

An important property of the Bloch states is that they describe spatially delocalized electrons (i.e. whose probability density is spread over the whole lattice) that are localized in the reciprocal space (also called k-space or momentum space): their crystalline impulsion is well-defined. In addition to their k-vectors, and because the Bloch states are eigenstates of the Hamiltonian, their energy is also well-defined. An appropriate framework to study the properties of electrons in solids is therefore the reciprocal space and the energy space. A graph of the relationship between the energy of the electrons in a solid and their momentum is called a band structure diagram (also called E-k diagram). An important feature of this graph is that not all energy states are allowed, which results in exclusion areas called bandgaps. For instance, the band structure of germanium (centered around the highest energy state occupied at 0 K) is shown in Figure 1, in which a band of energy between 0 eV and 0.66 eV does not have any state. If the Fermi energy intersects with an allowed state of the system (a line on the band structure), the material is a metal. When the position of the Fermi energy (which at usual temperatures corresponds to the chemical potential of the electrons) is inside such a band gap, the material is called either a semiconductor (for moderate width of the bandgap) or an insulator (large width of the bandgap). Then, the highest energy occupied band at 0 K is called the valence band and the lowest energy unoccupied state at 0 K is called the conduction band.

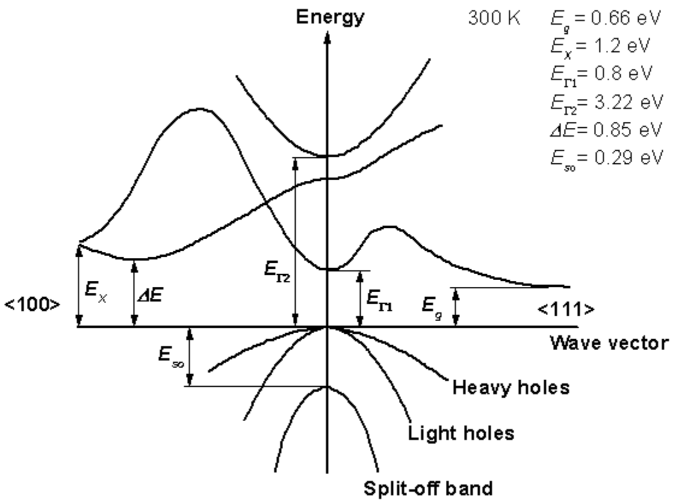

Figure 1: Band structure of Germanium[9]

b) Point defects in semi-conductors

A point defect is a point where the translation symmetry is broken, either under the form of a missing atom (vacancy), an extra atom in the lattice (interstitial), the presence of the wrong atom on a lattice site (substitutional impurity) or a combination of any of these (for instance, the pair of a vacancy and an impurity). A schematic of different point defects is shown in Figure 2.

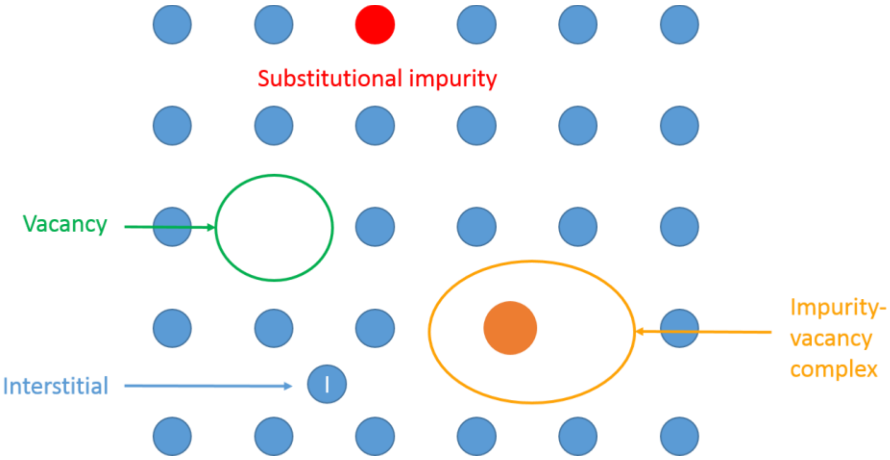

Figure 2: Schematic of a lattice of atoms with different point defects.

Because point defects are a deviation to the translation symmetry of the lattice, they introduce electronic states in the otherwise forbidden bandgap of semiconductors. This states interact with vthe carriers in the valence band and the conduction band by either capturing or releasing them, as is schematically shown on Figure 3, and are also called trap states. The filling of a trap by an electron or a hole follows a Fermi-Dirac distribution and is therefore defined by its position in the E-k diagram with respect to the Fermi energy. Note that traps are always filling and emptying. The occupancy of a point defect is a statistical average: when the Fermi energy is below the trap level, it means that the emission process is much faster than the capture process, not that there is no carrier absorption. The capture rate of a free carrier is connected to the capture cross-section of the trap, as well as the thermal velocity and concentration of the carrier, following Equation 2. The emission rate is thermal and follows an Arrhenius behavior (Equation 3, in which A denotes a pre-factor and E_T the position of the trap with respect to the conduction band (resp. valence band) for an electron (resp. hole) trap.

Without loss of generality, we will now derive the form of this prefactor in the case of an electron trap. Using the fact that when the Fermi energy is equal to the trap energy, the emission rate is equal to the capture rate (notwithstanding degeneracy effects) and that, in a semiconductor, $n=N_C \exp(-(E_C-E_F)/kT)$, we can write Equation 4 (in which N_C, E_C, E_F, σ and v respectively denote the density of states of the conduction band, the energy of the conduction band, the Fermi energy, the capture cross-section of the trap and the thermal velocity of the electrons). It follows that the prefactor A is equal to the product of the capture cross-section, thermal velocity and density of states of the relevant band.

$$c_n = \sigma v n \qquad \text{(Equation 2)}$$

$$e_n = A e^{-\frac{E_C - E_T (resp. E_T - E_F)}{kT}} \qquad \text{(Equation 3)}$$

$$c_n = \sigma v N_C e^{-\frac{E_C - E_F}{kT}} = A e^{-\frac{E_C - E_F}{kT}} = e_n \qquad \text{(Equation 4)}$$

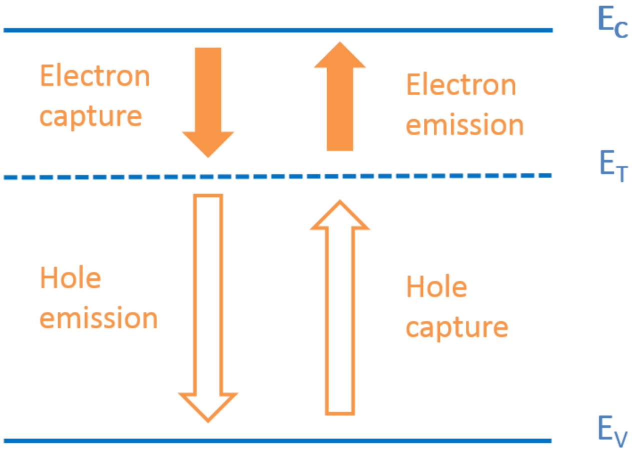

Figure 3: Schematic of the interaction of a trap state with carriers in a semiconductor

Point defects can have a tremendous impact on the properties of a material or the performance of a device. Because they capture carriers, they reduce the life-time of free electrons and holes, which affects minority carrier devices like solar cells. They also offer a non-radiative recombination path for carriers and thus decrease the efficiency of light emitting devices such as LEDs. They also increase the recombination-generation rate in a material, which for instance results in an increase of the leakage current in diodes and MOSFETs, which ultimately translates into lower sensitivities. By associating with other point defects and impurities, they can affect the diffusivity of species (most dopants in germanium diffuse by a vacancy assisted mechanism) or compensate the material.

c) Capacitance transients

When a rectifying junction (either Schottky or PN) is under bias, it behaves like a parallel plate capacitor (the parallel plates being the the edges of the neutral regions on each side of the depletion region), with $C=\varepsilon A/x_d$, where C is the capacitance of the junction, ε the dielectric permittivity of the material, A the area of the junction and x_d the width of the depletion region. Because the width of the depletion region is voltage dependent (Equation 5, in which x_d, ε, q, N_A, N_D, V_{bi} and V_a respectively denote the depletion width, the dielectric permittivity, the number of acceptors on the p-side, the number of donors on the n-side, the built-in voltage and the applied voltage), it is possible to modulate this capacitance by modulating the voltage. Moreover, because the capacitance of a device is the ratio of the stored charge on one electrode to the applied voltage, if the number of charges varies, so does the capacitance. Deep-Level Transient Spectroscopy (DLTS) is a technique that leverages this fact to extract information on defect states in semi-conductors. Its principle is shown in Figure 4. A DLTS scan follows 4 steps. First, the junction is under a constant reverse bias. There are no carriers in the depletion region (in white) and the defect states (in red) there are empty, while they are filled in the neutral region (in blue). Secondly, a pulse of (forward) voltage is applied. The capacitance spikes as the depletion region shrinks and trap states that were previously depleted are quickly filled with carriers. Thirdly, the voltage at the junction is reverted to its original reverse value. The depletion region goes quickly back to close to its original position, but the occupancy of the traps that were filled during the voltage pulse does not go back to equilibrium as quickly, because it is rate-limited by the thermal emission of the carriers (Equation 3). The thermal emission of carriers can be tracked by recording the capacitance transient of the reverse bias junction, as shown in Figure 4 in the case of a majority carrier trap, because the capacitance is the ratio of the number of charges to the (constant) voltage. A complimentary view of this transient phenomenon is that the filled traps are effectively compensating the material, resulting in a modulation of the depletion region width (Equation 5) and ultimately of the capacitance ($C=\varepsilon A/x_d$). Finally, once all the traps have released their charges, the material is at steady state again. Note that only traps below the Fermi energy for a 0 V bias can be filled during the pulse and therefore characterized. In addition, if one side of a PN junction is more doped than the other, most of the movement of the depletion region will happen in the lightly doped side (or the semiconductor side in the case of a Schottky junction), which means that only the lightly doped side is probed. In the rest of this thesis, we will always assume such a PN junction or a Schottky junction and neglect any effect of the voltage pulse on the highly doped side.

In the small signal regime (small number of traps with respect to the free carrier concentration), the amplitude of the capacitance transient is proportional to the number of traps emitting carriers. In the case of a single trap contributing to the capacitance transient, we can show by solving the Poisson equation that the amplitude of the signal follows Equation 6, in which ΔC, C_R, C (t), N_T, $N_{D/A}$, c_n, e_n, and t_p denote respectively the capacitance transient, capacitance at reverse bias, the capacitance as a function of time, the total trap density, the concentration of donors/acceptors, the capture rate, the emission rate of the trap and the duration of the forward voltage pulse. This equation has three parts. The first links the ratio of capacitance transient to total capacitance to the ratio of traps to dopant concentration and is a direct consequence of C=Q/V. The $(1-\exp(-c_n t_P))$ and $(1-\exp(-e_n t))$ respectively control for the proportion of traps that were filled during the forward voltage pulse and the thermal release of the carriers during the transient. The C_R^2/ C_P^2 is a correction factor taking into account the fact that the depletion region shrinks but does not disappear during the forward pulse. The last term relates to the fact that there is a transition region at the edge of the depletion region in which the material is depleted but the trap state is still below the depletion energy, as shown in Figure 5. The length of this transition region is the parameter λ, defined in Equation 7, which is dependent of the position the position of the defect state vis-à-vis the Fermi energy level in the neutral region. An important consequence of Equation 6 is that the ratio of traps to dopants is of the same order of magnitude as the ratio of capacitance transient to reverse bias capacitance. Practically, this means that the sensitivity if DLTS is in the range of 10^{-5}- to 10^{-1} of the total dopant concentration: if there are less traps, the capacitance meter is not sensitive enough, if there are more, the small regime hypothesis is not true anymore, and the depletion regions moves too much during the transient to precisely estimate the number of traps.

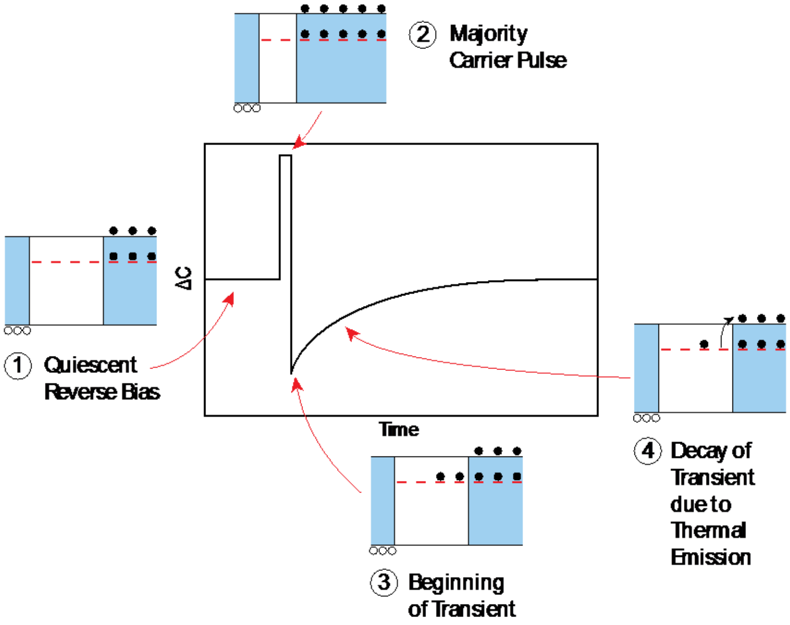

Figure 4: Schematic of the source of capacitance transients in DLTS experiments. The insets represent the bands on the y-axis and a spatial coordinate along the depletion region on the x-axis. The depletion region is in white, the neutral region in blue and a defect state is represented in red.

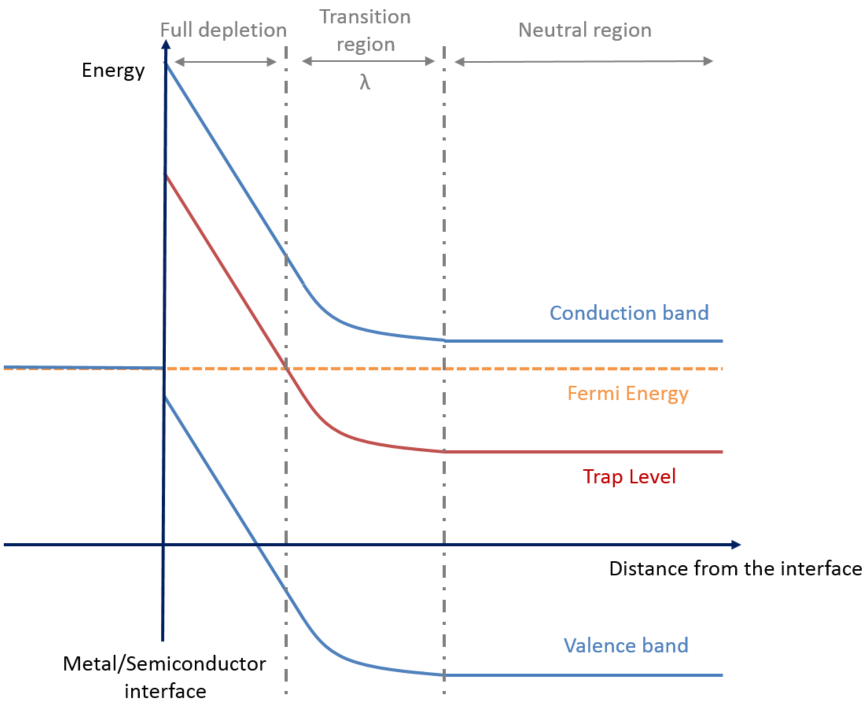

Figure 5: Schematic of the band bending happening at a Schottky junction. The transition region of length λ is the region where the materials is depleting but not the trap state.

$$x_d = \sqrt{\frac{2\varepsilon}{q}\left(\frac{1}{N_A}+\frac{1}{N_D}\right)\left(V_{bi}-V_a\right)} \tag{Equation 5}$$

$$\frac{\Delta C}{C_R} = \frac{C_R - C(t)}{C_R} = \frac{1}{2}\frac{N_T}{N_{D/A}}\left(1-\exp\left(-c_n t_p\right)\right)\left(1-\exp\left(-e_n t\right)\right)\left(1-\frac{C_R{}^2}{C_P{}^2}-2\lambda\frac{C_R}{\varepsilon A}\left(1-\frac{C_R}{C_P}\right)\right) \tag{Equation 6}$$

$$\lambda = \sqrt{\frac{2\varepsilon(E_F - E_T)}{q^2 N_{D/A}}} \tag{Equation 7}$$

d) Data extraction

DLTS uses pulses of voltage in order to generate transients of capacitance on a reverse bias junction. The emission rate has an Arrhenius behavior (Equation 8, in the case of an electron trap, and in which, in addition to previous notations, m^*, k_B and M respectively denote the effective carrier mass, the Boltzmann constant and the degeneracy of the band minimum), for which the activation energy is difference between the trap state level and the free carrier band. The emission rate can be measured by two different methods. The first one, used in conventional DLTS uses a rate filter called rate window and proceeds in a temperature sweep. The second is performed at a constant temperature and uses and algorithm (an inverse Laplace transform) to deconvolve the exponential components of a transient. This scheme is called Laplace DLTS (or LDLTS)

The principle of a rate window is shown in Figure 6. The signal measured during a temperature varying scan is equal to the difference of capacitance measured at two times (t_1 and t_2), chosen such as the difference is maximal when the emission rate is equal to a the rate window (defined by

R.W.=ln(t_2-t_1)/(t_2-t_1), with t_2=2.5t_1). A temperature sweep with a fixed rate window can therefore measure at which temperature a defect has a given emission rate. A typical scan obtained by such conventional DLTS is shown in Figure 7. Each peak corresponds to a point defect state, labelled according to their apparent activation energy (e.g. E_{38} is 0.38 eV below the conduction band). Then, by varying the rate window, a map of emission rate versus temperature can be drawn. Experimentally, we have used rate windows between 5 s^{-1} and 2000s^{-1}. Sometimes, defect states are too close to one another and, contrary to the case of Figure 7, a peak is due to the convolution of multiple peaks. In this case, the isothermal Laplace DLTS can be preferred because it will be able to discriminate the presence of multiple peaks more easily. Of course, this last technique needs to be done at multiple temperatures in order to obtain the temperature dependence of the emission rate.

Both measurement schemes result in the same data, the establishment of an Arrhenius plot of the emission rate (Figure 8). Note that on these graphs, the y-axis is the emission rate divided by the temperature squared, in order to take into account the temperature dependence of the effective density of state and thermal velocity of the carriers, in accordance with Equation 8). From the slope of the Arrhenius plot and its intersection with the y-axis, the apparent activation energy of the trap and its apparent capture-cross section can be extracted. Note that these are only apparent parameters because, as shown in Equation 9 (in which σ_∞, E_σ, ΔG, ΔH and ΔS respectively denote the prefactor of the capture cross-section, its activation energy, the free energy, the enthalpy and the entropy of ionization of the defect), the eventual temperature dependence of the capture cross-section and the entropy term of the free energy results in a difference between measured (i.e. apparent) and real parameters. The correspondence between the apparent and real parameters is shown in Equation 10 and Equation 11.

In order to assess the real parameters, it is necessary to measure the value of the capture cross-section independently from a DLTS measurement. This is done by the pulse filling method, which leverages the fact that the capture of carriers during the voltage pulse of a DLTS measurement is not instantaneous. If pulses of various length are used, different fractions of the defects will be filled, according to Equation 12. By combining equation 6 and equation 12, we can obtain Equation 13 (with ΔC the amplitude of the transient for a pulse of duration t_p and C_∞ the amplitude of a transient generated by an infinitely long filling pulse). This equation is the core of the pulse filling method which uses the amplitude of the capacitance transients as a function of the filling pulse to extract the capture rate of the trap, which then allows for the extraction of the real capture cross-section of the trap. Then, by repeating this measurement at multiple temperature, the Arrhenius behavior of the capture cross-section can be inferred and both the prefactor and activation energy can be calculated. This knowledge can finally be used to determine the free enthalpy and entropy of ionization measured from the apparent parameters.

$$e_n = \sigma v N_C e^{-\frac{E_C-E_T}{kT}} = \sigma \sqrt{\frac{3k_B}{m^*}} 2M \left(\frac{2\pi m^* k_B}{h^2}\right)^{\frac{3}{2}} T^2 e^{-\frac{E_C-E_T}{kT}} \qquad \text{(Equation 8)}$$

$$e_n = \sigma v N_C e^{-\frac{E_C-E_T}{kT}} = \sigma_\infty e^{-\frac{\sigma_\infty}{kT}} v N_C e^{-\frac{\Delta G = \Delta H - T\Delta S}{kT}} = \sigma_\infty e^{\frac{\Delta S}{k}} v N_C e^{-\frac{\Delta H + \sigma_\infty}{kT}} \qquad \text{(Equation 9)}$$

$$E_a = \Delta H + E_\sigma \qquad \text{(Equation 10)}$$

$$\sigma_a = \sigma_\infty e^{\frac{\Delta S}{k}} \qquad \text{(Equation 11)}$$

$$N_{filled} = N_{total}\left(1-\exp\left(-c_n t_p\right)\right) = N_{total}\left(1-\exp\left(-\sigma v n t_p\right)\right) \qquad \text{(Equation 12)}$$

$$\frac{C_\infty - \Delta C}{C_\infty} = \exp\left(-c_n t_p\right) \qquad \text{(Equation 13)}$$

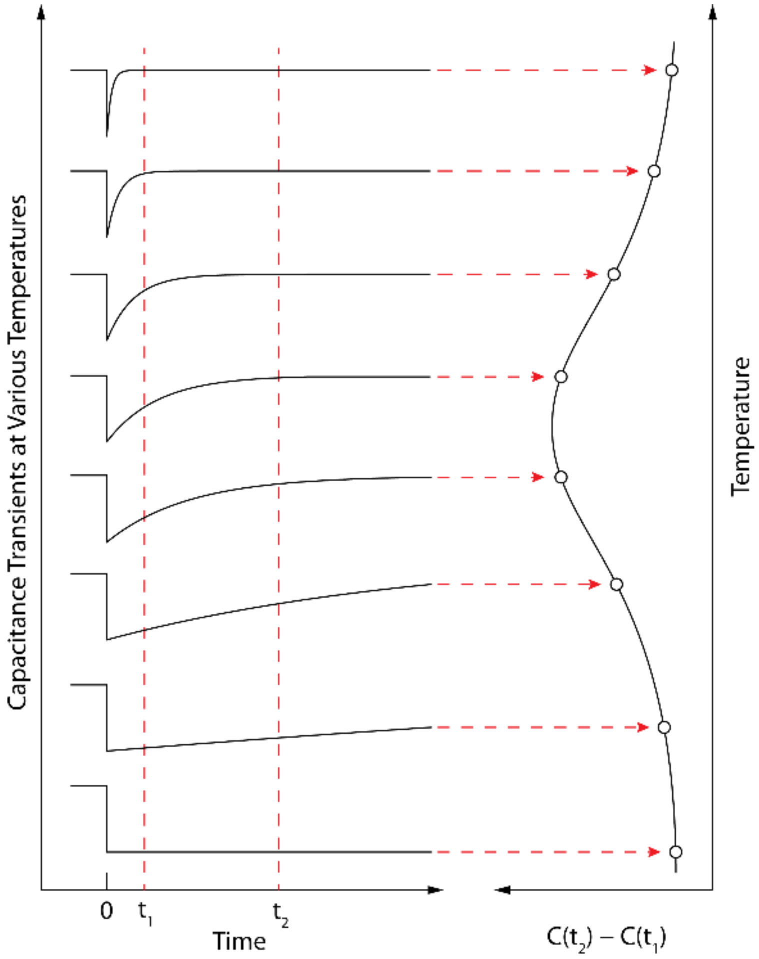

Figure 6: Schematic of the underlying principles of a rate window filter in conventional DLTS.

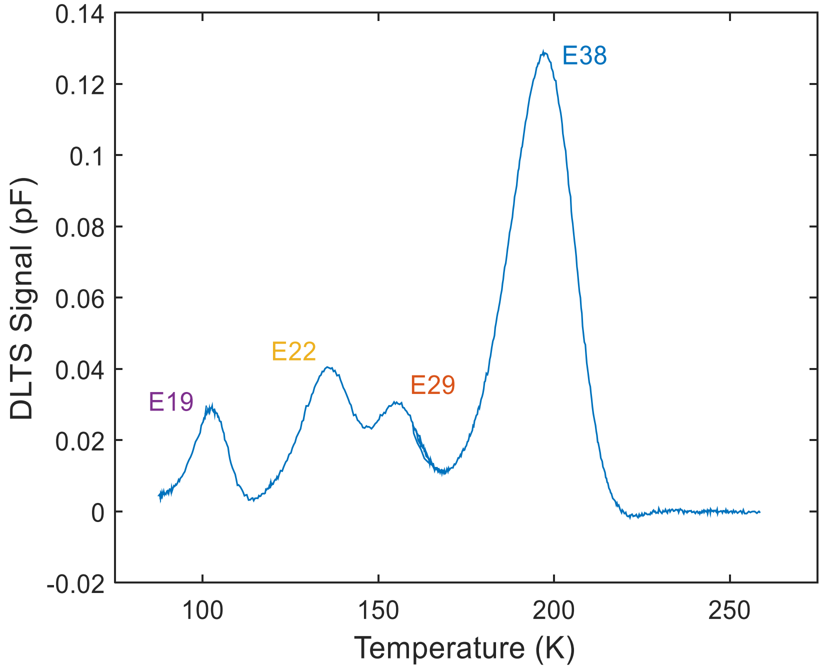

Figure 7: Conventional DLTS scan. The sample is a piece of 10^{15} cm^{-3} Sb-doped n-type germanium irradiated by 10 Mrad of ^{60}Co gamma rays. The rate window is 200 s^{-1}, the reverse voltage is -5 V, the pulse voltage 0 V, and the pulse duration is 5 ms.

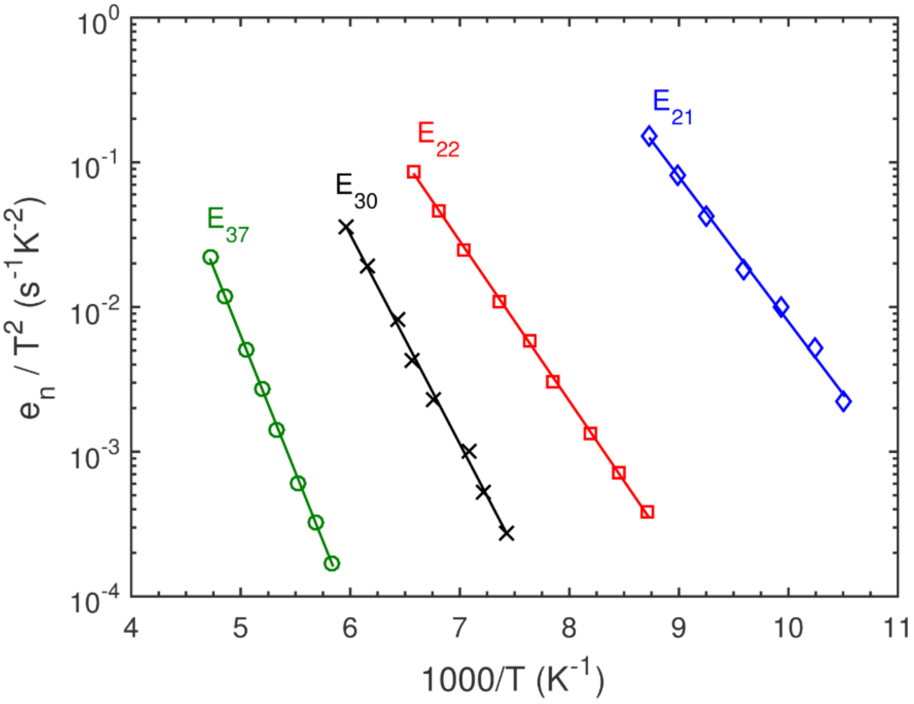

Figure 8: Arrhenius plot of the four defects observed after the ^{60}Co gamma ray irradiation of n-type germanium.

II. Irradiation damage

a) Generation of point defect through irradiation

Defects are naturally present in materials above 0K because such is the nature of entropy. However, their nature and concentration depends strongly of the history of the material: how was it grown, how was it processed, what happened during its lifetime, etc. Reproductibility is therefore an issue to study poinf defects. In addition, defects are often in concentrations high enough to affect the performances of a device (higher leakage current, lower lifetime, generation recombination noise, etc.), they might be in concentration outside of the sensitivity range of DLTS (10^{-2}-10^{-5}) of the doping lelvel. This is why, instead of studying the defects naturally present in a material or a device, it is easier to study the defects that have been artificially and controllably introduced. To this end, radiations are especially convenient, because they provide a reliable, reproducible mean to generate defects.

Defects are created by irradiation when the irradiating particle collides with an atom of the lattice and transmits enough energy to knock it out of site. This energy threshold is around 20 eV in the case of silicon and germanium[10]. After the collision, one or multiple vacancies and self-interstitials appear in the material. If one vacancy and a self-interstitial are close from one another, they are called a Frenkel pair. Above 100 K in germanium[11], [12], the Frenkel pair is not stable: it either self-annihilate, or each of its constituent breaks from the other and diffuse through the material until it forms a stable defect complex, for instance the association of a vacancy with a donor impurity or a self-interstitial with a substitutional carbon. Note that the vacancies and interstitials are the building blocks of point defects, and only disappear from the material when they either recombine with a defect of the other type or when they anneal out at a free surface. The defects that are created during or right after the collision event are called primary defects. Those formed by association of primary defects with another defects are called secondary defects. The energy transmitted to the lattice atom during the collision is critical for the nature of the primary defects. According to the Kinchin-Pease model[13], if the transmitted energy is between one and around four times the threshold formation energy for the creation of a Frenkel pair, only one Frenkel pair can be generated (single displacement event). If the energy is even higher, a collision cascade with multiple displacements can occur, as the displaced atom itself can knock the neighboring atoms off-site. This can result in the formation of much more complex defects, such as voids or even amorphized regions.

By varying the dose, the nature of the radiation and the irradiation conditions (rate, energy, etc.), it is possible to fine-tune what defects are introduced and therefore obtain more insights on the physics of the material. In addition, more than just damaging the target, irradiation can be used to affect the properties of a device (e.g. control the dopant concentration and their activation). In the following subsections, we will describe the specifics of how gamma ray and heavy particles introduce damage in a material.

b) Gamma ray damage

Historically, gamma rays have been used on germanium to make high resistivity material [14], because the defects generated by this irradiation compensate it homogeneously and at a slow rate (it is easy to control what dose is optimal). Gamma rays are photons whose energy is above a hundred keV ($\lambda<0.01$ nm). They interact with matter by three different mechanisms: photo-electric effect (absorption of the photon and excitation of an electron from a core shell, dominant for energies below 50 keV), Compton scattering (inelastic scattering of the photon, resulting in the emission of a lower energy photon and an excited electron, as shown in Figure 9, dominant from 100 keV to 5 GeV) and pair production (annihilation of the photon and creation of an electron-positon pair, dominant for higher energy photons). In this doctoral work, we have used the gamma rays produced the radioactive decay of ^{60}Co as a source. ^{60}Co is an unstable isotope of cobalt with a half-life of 5.3 years. It decays into ^{60}Ni, emitting in the process two photons of energy 1.17 MeV and 1.33 MeV. At this energy, Compton scattering is the dominant dissipation process. Note that the gamma ray itself does not interact directly with the nuclei of the material, but only with the electrons. After the Compton scattering, the electrons have a certain kinetic energy determined by the angle of scattering and conservation of momentum and energy. The probability density of scattering is given by the Klein-Nishina formula. We applied this equation to the Compton scattering of a 1.33 MeV photon (the highest energy gamma ray emitted during the decay of a ^{60}Co source) to obtain Figure 10. After its formation, it is the Compton electron itself that interact with the nuclei in the lattice and generates the Frenkel pairs. In a binary collision model, we can calculate what is the maximum energy transferred to a nuclei after interaction with a Compton electron. In Figure 11, such a relation is shown in the case of silicon and germanium. Because of the large difference of mass between an electron and a nucleus, the conservation of momentum results in the transfer of only a small fraction of the kinetic energy of the electron to the nucleus, on the order of 0.01%. Using Figure 10 and Figure 11, we see that Compton scattering of ^{60}Co gamma rays generates photons of high enough energy to create lattice damage in germanium, but not enough for multiple displacements. This means that the primary damage induced by ^{60}Co gamma irradiation only consists in mono-vacancies and self-interstitials, which, as will be describe in a later chapter will tremendously help the analysis of the physical nature of the irradiation defects. The case of silicon is slightly different. Due to its smaller mass, Compton electron can share more of their kinetic energy with a silicon nucleus, and multiple displacements are possible after a ^{60}Co gamma irradiation. This is consistent with experimental data in silicon that shows the primary formation (i.e. during the collision cascade) of divacancies in silicon after irradiation by gamma rays and 1 MeV electrons [15]. Finally, another important feature of gamma rays is that Compton scattering is a rare event: gamma rays interact weakly with materials. In the case of germanium, the interaction length is a few centimeters, effectively resulting in an homogeneous defect generation in the 0.55 mm thick germanium wafer pieces we used for our study.

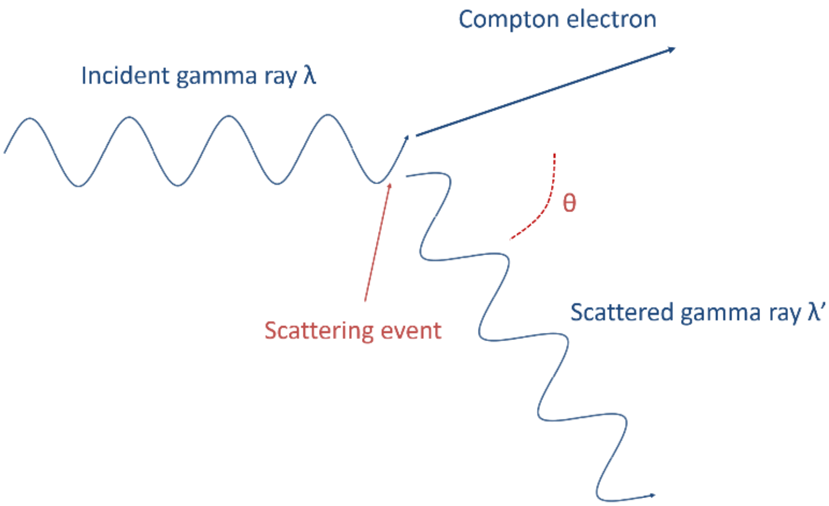

Figure 9: Schematic of Compton scattering.

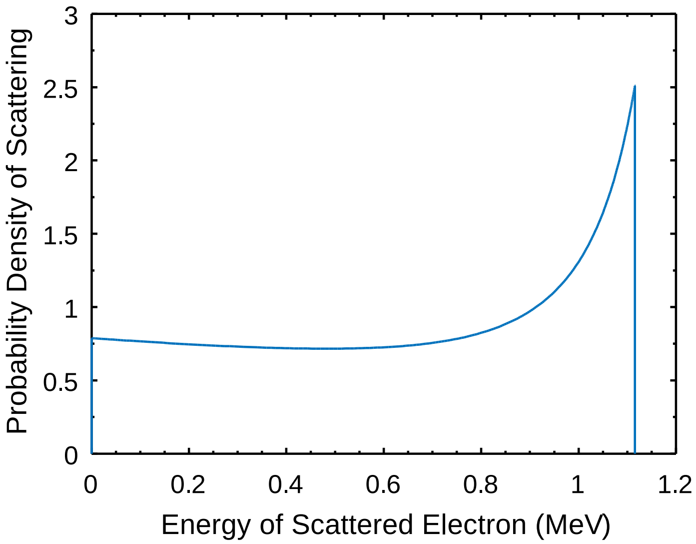

Figure 10: Probability density of scattering versus energy of the scattered electron after Compton diffusion of a 1.33 MeV gamma ray.

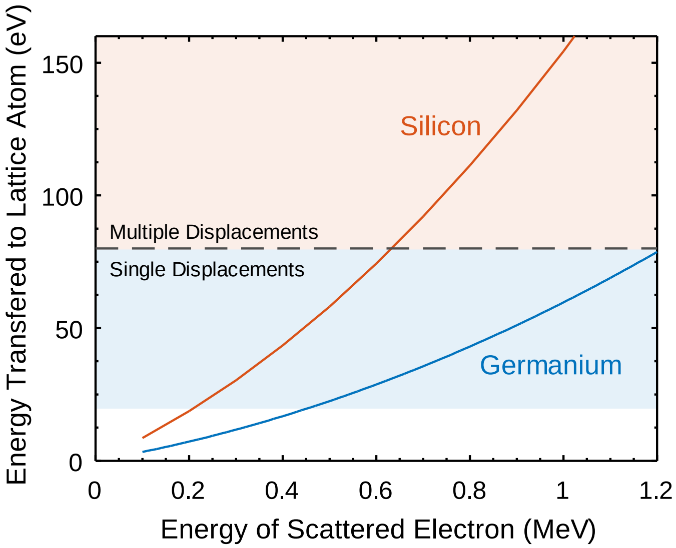

Figure 11: Maximum energy transferred to a silicon or germanium atom after collision with a high energy electron, in a binary collision model. The white zone denotes a transferred energy below the single displacement threshold energy of 20 eV, the blue zone is the single displacement zone (energy between one and four times the threshold energy) while the orange zone denotes possible multiple displacements. The x-axis scales corresponds to the range of kinetic energy of the electrons that can be generated by Compton scattering of ^{60}*Co photons.*

c) Irradiation by particles

Besides gamma rays, we have irradiated our material with light (neutrons, helium nuclei) and heavy (germanium, phosphorus) particles. In this case, the impact of the particle on an atom of the lattice can result in multiple displacements and a collision cascade: the energy and momentum transmitted are so high that the displaced atom also collides with others and generate more defects. The heavier the particle, the bigger the collision cascade. In natural environments (space, nuclear power plants, etc.), radiations are mostly made of light particles. In an industrial setting however, heavy particles are common: the most common way to dope semiconductors in state of the art Integrated Circuit (IC) foundries is by irradiation (in this case, a more proper term is “implantation”, which we will use from now on when referring to an irradiation whose goal is not to generate defects but to introduce an impurity), which leverages the high controllability of energy and dose allowed by modern implanters to deposit impurities (mostly donors) at a target location and at a chosen concentration in a semiconductor.

Usually, the dose required to achieve the desired concentration level of the implanted ions generates so much defect that the material is amorphized, as shown in Figure 12. In this case, crystallinity can be recovered by annealing the sample to provoke a Solid Phase Epitaxy (SPE). At high enough temperatures (>350°C for germanium), the mobility of the atomshas increased enough for the crystalline side of the amorphous/crystalline (a/c) interface to behave as an epitaxial template, leading to a regrowth front, consuming the energetically unfavorable amorphous phase until crystallinity is fully recovered. This process anneals out most of the defects generated by the implantation step and yields high quality material, to the point that pre-amorphization implants are often done prior to other implantations, partially in order to insure a good quality SPE can happen.

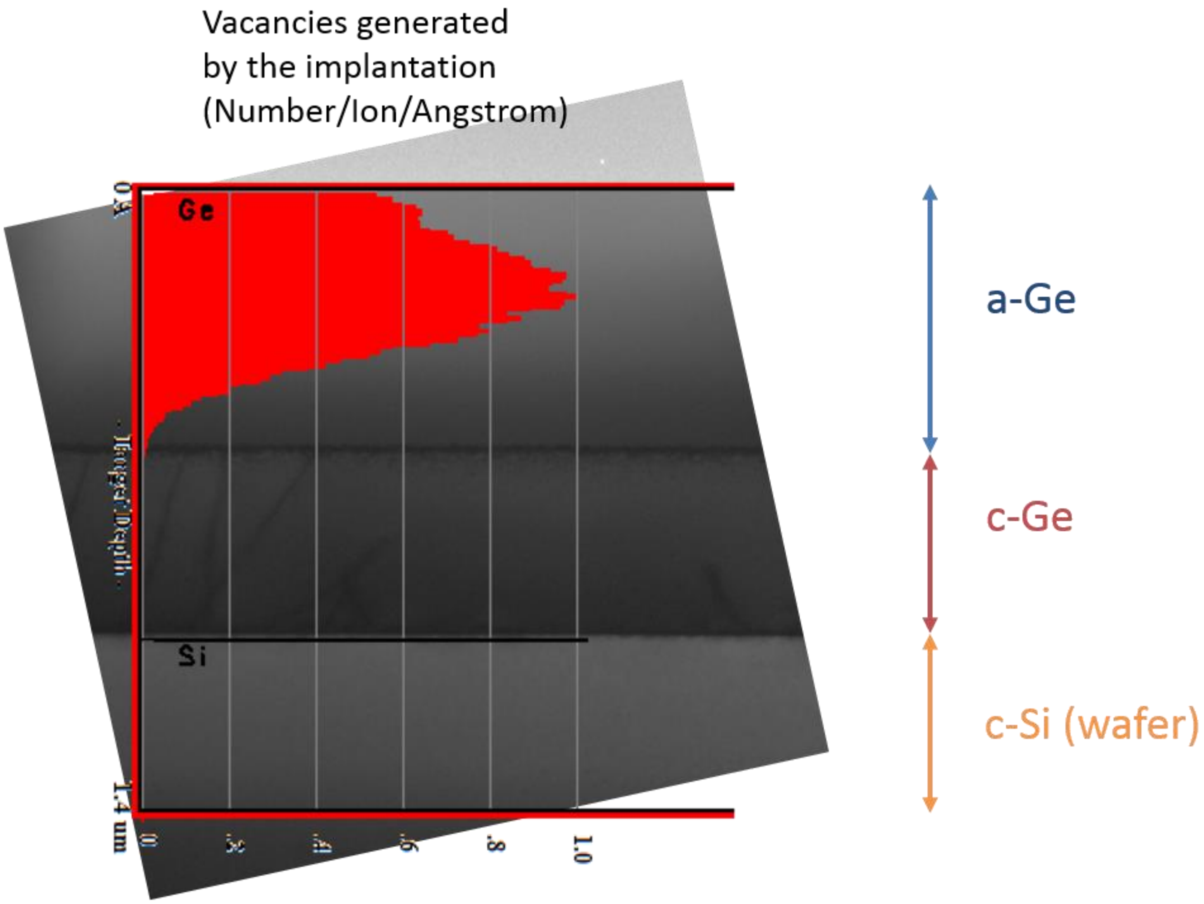

Figure 12: Superposition of the TEM micrograph of a germanium on silicon epi-layer, as-implanted by 4.6x10^{15} cm^{-2} 350 keV phophosrus, and the distribution of defects as predicted by SRIM. The dose is high enough that all of the implanted region is amorphized while the material below it is still crystalline.

Chapter 3. Point defects in ^{60}Co gamma irradiated n-type Czochralski germanium

The following chapter is partially reprinted from *Journal of Applied Physics*[16], with the permission of AIP Publishing, and was performed in collaboration Neil S. Patel, who also was a member of the Kimerling group at MIT.

I. Introduction

Despite the recent renewed interest in germanium, little is known about the point defects in this material. This is partially a consequence of the limited success of electron paramagnetic resonance (EPR) studies in germanium, due to its varied isotopic composition[17] and large spin orbit coupling which yields a short spin-lattice relaxation time[18], [19]. In addition, knowledge of defects in silicon is not directly applicable to germanium, as was shown in Si_xGe_{1-x} studies[20]. Because EPR currently does not provide direct identification of defects in germanium, identifications must be obtained through more indirect methods. In this chapter, we use ^{60}Co gamma irradiation to generate homogenously distributed and isolated Frenkel pair primary defects in Sb-doped germanium. The generated vacancies and interstitials diffuse and react with each other or impurities resulting in the formation of secondary defects which we characterize by Deep-Level Transient Spectroscopy (DLTS). Similar DLTS studies of defects in germanium[21]–[27] have been performed in the past, however, as is often noted, there is little consensus and considerable scatter between different studies as to the properties and identification of previously observed defects. In conjunction with the analysis of defect state properties by DLTS, we studied the growth and decay of the defects by room temperature annealing of samples irradiated at 77 K and isothermal anneals at temperatures ranging from 50 °C to 200 °C for samples irradiated at 300 K. We show in this chapter that all the vacancies have reacted to form Sb donor-vacancy associates (E-center), while the interstitials are spread between three distinct defects states whose annealing reactions are coupled.

II. Experimental procedures

The tested germanium wafers were grown by Czochralski (CZ) method with an Sb concentration of $\sim 1\times10^{15}$ cm^{-3} as measured by C-V analysis at 300 K. Schottky contacts were formed by thermal evaporation of Au onto Ge immediately after an adaptation of RCA cleaning procedures for germanium (5 minutes in a 1:4 $NH_4OH:H_2O$ bath, followed by 30 seconds in 1:6 $H_2O_2:H_2O$, 15 seconds in HF and finally 30 seconds in 1:4 $HCl:H_2O$, all done at room temperature). Ohmic contacts were formed by scratching InGa eutectic alloy onto the backside of the wafer.

Gamma irradiations were performed at MIT using a cobalt-60 source which radioactively decays emitting gamma rays with energies of 1.17 MeV and 1.33 MeV in equal proportions. Samples were irradiated in a circular chamber lined with ^{60}Co rods providing homogenous irradiation of the material. In order to prevent oxidation of the surface during irradiation by ozone generated from the reaction of gamma rays with oxygen in the air, samples were irradiated either inside vacuum ampoules or with their surface in contact with a piece of silicon wafer. Both methods prevent sample surfaces from directly contacting the air in the irradiation chamber and yielded similar defect profiles. Radiation dose rates were approximately 7 krad/min. Reported irradiation doses are calibrated with reference to water. This radiation source only generates isolated Frenkel pairs and rules out the direct generation of complex defects such as the divacancy or the di-interstitial. While secondary formation of uncorrelated defects is possible, the divacancy is not expected to form due to coulombic repulsion between negatively charged mono-vacancies.

Irradiation doses were chosen such that measured defect concentrations were not greater than 1% of the carrier concentration. This allowed for a more accurate determination of defect concentrations when using DLTS. Gamma irradiations were performed after deposition of Schottky contacts. Gamma radiation with energies around 1 MeV are highly penetrative with absorption lengths close to 10 cm in germanium. Therefore, generated defects are expected to be homogenously distributed through the irradiated 500 µm thick wafer samples.

Anneals were performed by rapid submersion of samples, wrapped in aluminum foil, into a heated oil bath, followed by air quenching. DLTS signal was collected digitally using a lock-in amplifier algorithm allowing for measurement of defect concentrations ~10^{-5} cm^{-3} below carrier concentrations. Samples are placed in a cryogenic chamber which can be cooled to 85 K during measurements. DLTS scans of unirradiated diodes showed no defects with measureable concentrations.

III. Point defect states in germanium

A DLTS spectrum for 10^{15} cm^{-3} Sb-doped germanium irradiated with ^{60}Co gamma radiation at room temperature (300 K) is shown in Figure 13. For coherence with previous convention, defects will be labelled by their apparent activation enthalpies; E_{37} denotes an electron trap with an apparent activation enthalpy of 0.37 eV. Four electron trap states were produced during irradiation in contrast to the numerous defect states seen in previous literature. Figure 14 shows emission rate vs. temperature data for defect states observed after gamma irradiation in this work compared to defect states seen in the literature due to gamma, proton, and electron irradiation sources. Our data was analyzed to extract apparent activation enthalpies and apparent capture cross sections. Pulse-filling measurements were performed at various temperatures to measure real capture cross sections and determine temperature dependencies if present. A summary of properties extracted from DLTS measurements for the observed defect states after irradiation at 300 K is listed in Table I. It should be noted that, even though DLTS has sensitivity to 10^{-5} cm^{-3} below carrier concentrations, we observe variations in introduction rates from sample to sample, making the reported introduction rates accurate to approximately ±10%. When possible, anneals were performed on the same sample in order to remove error from this contact to contact variation. In those cases, the error in defect concentration is close to the limit of DLTS sensitivity. To make comparisons between samples with varying doses, defect concentrations are normalized by the irradiation dose and are reported in units of $cm^{-3}Mrad^{-1}$. We approximate our temperatures to be accurate to ±1 K which allows for accuracy of reported energies to ±1%.

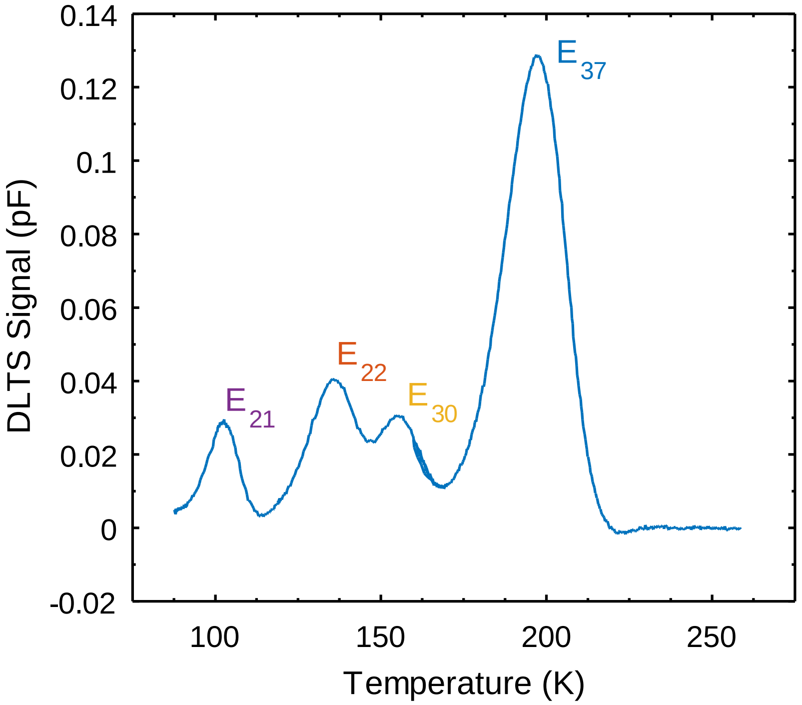

Figure 13. DLTS spectrum obtained after ^{60}Co irradiation at 300 K of 10^{15} cm^{-3} Sb-doped germanium showing the generation of four distinct defects. During measurement, the sample was pulsed for 5 ms from -5 V to 0 V and signal was collected for a 200 s^{-1} rate window.

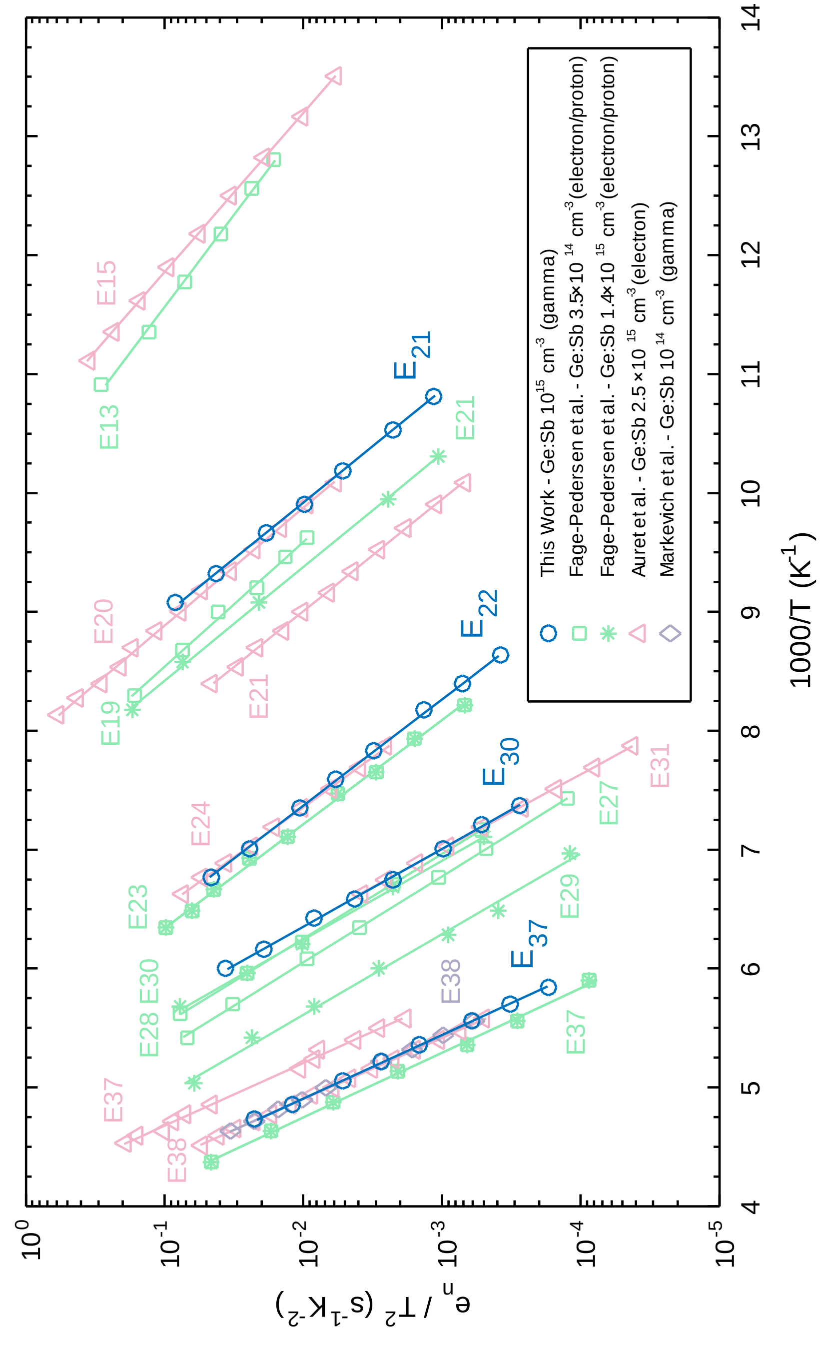

Figure 14. Defect states observed by different groups[25], [27], [28] in studies of Sb-doped n-type germanium irradiated by varying radiation sources. E_{37} is observed in all studies and has previously been assigned to the E-center, a donor-vacancy pair. Defects with states similar to E_{30}, E_{22}, and E_{21} have been seen in some studies but are not consistently detected.

Table I. Summary of defect states in ^{60}Co irradiated Sb-doped germanium

Defect	**Apparent Enthalpy (eV)**	**Free Energy of Ionization (eV)**	**Apparent Capture Cross Section (cm^2)**	**Real Capture Cross Section (cm^2)**	**Introduction Rate (cm^{-3}Mrad^{-1})**
E_{37}	0.37	0.29 - 3.94kT	3.9×10^{-15}	$7.6\times10^{-17}e^{-85meV/kT}$	2.2×10^{11}
E_{30}	0.30	NA[a]	1.2×10^{-14}	$> 10^{-15}$	NA[b]
E_{22}	0.22	0.22 - 1.53kT	4.6×10^{-16}	1.1×10^{-16}	NA[b]
E_{21}	0.21	0.16 - 8.29kT	8.0×10^{-14}	$2.0\times10^{-17}e^{-54meV/kT}$	NA[b]

[a] The experimental apparatus was not fast enough to measure the real capture cross-section of E_{30} preventing calculation of the real enthalpy and entropy of ionization.

[b] Not quantifiable since defect concentrations are not stable at 300 K

The properties of a defect state are more than just an identifying tool and provide information about the physical nature of the defect. A temperature dependent capture cross section indicates the presence of an activation barrier to carrier capture or that capture requires phonons[29] due to rearrangement of bonds upon capture and emission of carriers. The entropy of ionization term in the free energy results from changes in configurational and/or vibrational (i.e. related to the strength of the bond) entropy after carrier capture, which is why it is frequently observed in conjunction with a temperature dependent capture cross section. We can therefore infer that E_{37} and E_{21} experience a structural rearrangement upon absorption of a carrier.

IV. Point defect Reactions

a) Irradiation at 77 K

Samples were irradiated with a 10 Mrad dose while submerged in liquid nitrogen (77 K) to study the diffusion of primary defects and the growth of associates. During and after irradiation, the samples were kept in the dark to prevent any effects from photogeneration of carriers. At the time of the first measurement (20 minutes spent above 200 K), only E_{30} and E_{37} are observable. The concentration of E_{30} is close to the noise level (10^9 cm^{-3}Mrad^{-1}) while the concentration of E_{37} is much higher at 1.7×10^{11} cm^{-3}Mrad^{-1}. Unlike E_{30}, E_{22}, and E_{21}, the concentration of E_{37} remains constant during the duration of the experiment with an introduction rate similar to room temperature irradiation levels. Similar fast formation kinetics were also observed after a 22 K electron irradiation of Sb-doped germanium by Mesli et al.[12] E_{37} has been previously identified as the Sb donor-vacancy associate, also referred to as the E-center. The evidence for this will be discussed in Section V.A. Ionized Sb atoms have a positive charge which can interact strongly with negatively charged mono-vacancies. The identification of E_{37} as the E-center is therefore consistent with the observed formation kinetics.

We expect that there are no competing sinks with Sb since no other impurity is present in as large concentrations in the tested material. In addition, the Sb concentration is much greater than the concentration of generated defects; therefore, the fast defect formation indicates that all of one type of the primary defects, most likely the vacancies, are quickly consumed by the formation of E_{37}. The introduction rate of E_{37} thus provides an estimate of the introduction rate of uncorrelated Frenkel pairs, the vacancy-interstitial pairs which do not recombine and annihilate shortly after generation by incident radiation.

If E_{37} accounts for all the vacancies in the material, then E_{30}, E_{22}, and E_{21} represent defect states of interstitial associates. Figure 15 shows the defect concentrations of E_{30}, E_{22}, and E_{21} plotted as a function of the time spent by the samples above 200 K after irradiation and removal from liquid nitrogen. E_{37} is not plotted because its introduction rate is higher and its concentration constant. The differences in annealing behavior show that none of the observed defect states are different charge states of the same defect. The annealing behavior in Figure 15 has two stages. During the first stage, all the defects grow, which shows that they form after irradiation and are secondary defects. E_{22} is the last defect to be observed, however, once detected, it has the fastest formation kinetics and outgrows E_{21} and E_{30}. This behavior will be addressed in greater detail in Section V.B.2. The second annealing stage starts after approximately four days of annealing when E_{22} continues growing at a slower pace, while the concentration of E_{21} is stable and E_{30} decays.

The existence of two stages in the evolution of the defects can be explained by accounting for the consumption of all the free self-interstitials in the material. During irradiation, interstitials and vacancies are created in equal proportions. All the mono-vacancies might quickly react with Sb to form E-centers, but perhaps self-interstitials cannot find sinks as quickly. They diffuse through the material until they form stable and observable defect associates. This corresponds to the first annealing stage. Note that this would indicate that the self-interstitial is not detectable by DLTS, likely because the defect state is in the lower half of the bandgap or outside the bandgap. If there are enough sinks, eventually all the self-interstitials will have reacted and the second stage begins where defects can only evolve by transforming into one another. The kinetics involved in the second stage are slower than in the first stage as the reactions involve defect associates which are not as reactive as the self-interstitial. The observed defect formation kinetics after irradiation at 77 K are consistent with observations in low temperature studies by Mesli et al.[12] and Kolkovsky et al.[30].

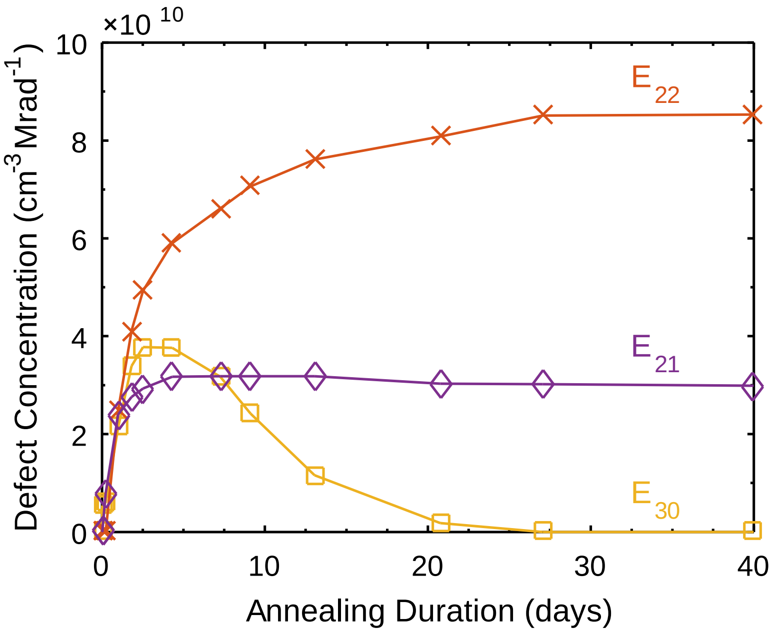

Figure 15. Interstitial containing defect concentrations during room temperature (300 K) annealing of Ge irradiated at 77 K by ^{60}*Co. Annealing duration represents the time the sample spent above 200 K after irradiation. The concentration of* E_{37}*, which accounts for all the vacancies, is constant at* 1.7×10^{11} $cm^{-3}\cdot Mrad^{-1}$ *for the entire annealing duration. Defect concentrations are normalized by the irradiation dose and are reported in units of* $cm^{-3}Mrad^{-1}$*.*

b) Irradiation at 300 K

Irradiation at room temperature was followed by anneals at higher temperatures to provide additional information about the growth and decay of the defects. Defect concentrations after a series of 15 minute isochronal anneals at various temperatures are plotted in Figure 16. E_{37}, E_{22}, and E_{21} are all stable at room temperature. However, at room temperature, E_{30} will slowly decay over weeks, as was observed during room temperature annealing after irradiation in liquid nitrogen, and is already completely removed by annealing at 85 °C for 15 minutes. E_{37} is stable to ~100 °C and is only completely removed in 15 minutes at ~200 °C. At temperatures ~100 °C, E_{22} decays while E_{21} concomitantly grows. E_{21} is stable to ~150 °C.

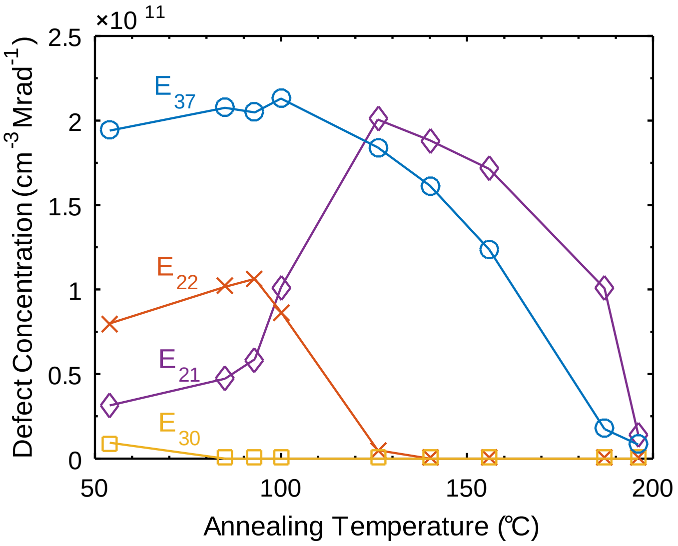

Figure 16. Defect concentrations after 15 minute isochronal anneals of ^{60}*Co irradiated Sb-doped germanium. Defect concentrations are normalized by the irradiation dose and are reported in units of cm*$^{-3}$*Mrad*$^{-1}$*.*

Isothermal anneals at multiple temperatures were used to extract annealing rates for each defect vs. temperature. Figure 17 shows defect concentrations vs. annealing durations for an isothermal anneal at 93 °C. All annealing reactions followed exponential trends indicating first-order reactions. Figure 18 shows a plot of the annealing rate vs. inverse temperature used to extract the frequency prefactors and activation energies of the annealing defect reactions. A summary of the extracted parameters are shown in Table II. Spatial defect profiles were obtained before and after annealing reactions and showed that concentrations for all defects remained homogenously distributed throughout the material after annealing.

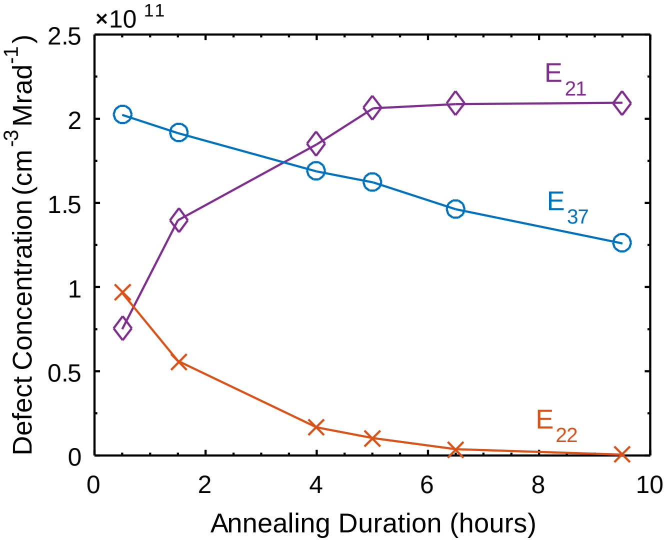

Figure 17. Defect concentration as a function of annealing duration at 93 °C. When E_{22} *has annealed out,* E_{21} *stops evolving whereas the decay rate of* E_{37} *is not affected. Defect concentrations are normalized by the irradiation dose and are reported in units of cm*$^{-3}$*Mrad*$^{-1}$*.*

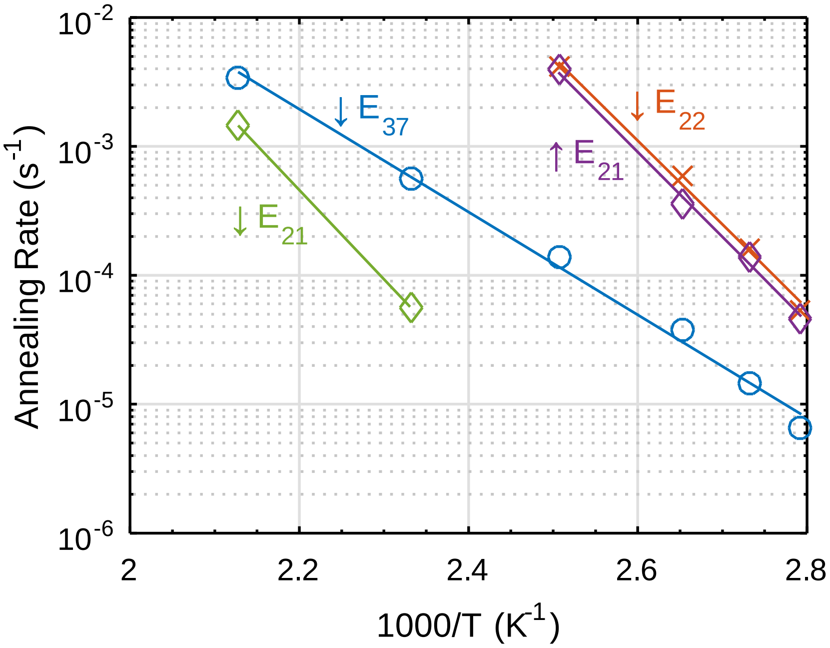

Figure 18. Annealing rate vs. temperature data extracted from isothermal anneals of ^{60}Co irradiated Sb-doped germanium. Up and down arrows next to defect labels indicate whether the defect concentration increases or decreases upon annealing.

Table II. Summary of annealing reaction parameters extracted from isothermal anneals

Annealing Reaction	**Activation energy (eV)**	**Frequency Prefactor (s^{-1})**	**R^2**
E_{37} Decay	0.79	1.2×10^{6}	0.9943
E_{22} Decay	1.29	8.9×10^{13}	0.9956
E_{21} Growth	1.31	1.3×10^{14}	0.9961
E_{21} Decay	1.41	1.9×10^{12}	NA

The isochronal and isothermal annealing data suggests a relationship between E_{21} and E_{22}. After 15 minutes at 100 °C (Figure 16), E_{30} has annealed out and E_{37} is stable, but the concentrations of both E_{22} and E_{21} change. The concentration of E_{22} decreases while the concentration of E_{21} increases. Eventually, the growth of E_{21} stops at ~125 °C which coincides with the removal of E_{22}. E_{37} is not coupled to the two defects as can be inferred from Figure 17 and isothermal anneals at other temperatures not shown here; the growth of E_{21} stops after E_{22} has fully annealed out, while the decay of E_{37} is unaffected and continues at a constant rate. This gives further evidence that E_{21} and E_{22} contain the same primary defect. The increase in the concentration of E_{21} when E_{22} decays shows that the decay reaction of E_{22} provides reactants for the growth of E_{21}. As seen in Table II, the growth of E_{21} and decay of E_{22} have the same activation energy (~1.3 eV) and prefactor (~10^{14} s^{-1}). This indicates that the growth of E_{21} is favorable at these temperatures but is limited by the supply of reactants produced by the decay of E_{22}. The activation energy and prefactor for the growth of E_{21} would differ from the decay of E_{22} if an unobservable defect was providing reactants.

The prefactors in Table II also provide information about annealing mechanisms. The prefactor can be viewed as the attempt frequency (usually equal to the Debye frequency: $7.5\text{x}10^{12}$ s^{-1} at room temperature for germanium) divided by the number of jumps required to reach the sink:

$$\nu_0 = \nu_{attempt}/N \ . \tag{1}$$

The small annealing prefactor of E_{37} is consistent with a diffusion limited annealing reaction. The high annealing prefactors for the interstitial defect reactions indicate that the annealing process is a single jump event, such as dissociation or a configurational transformation of the defect.

V. Defect assignments

a) Donor-vacancy associate: E_{37}

The defect with the largest introduction rate in ^{60}Co irradiated Sb-doped germanium is E_{37}. Its defect state properties match those measured by other groups[25]–[27] (Table I). To date, it is the most studied defect in germanium and is associated in the literature to the second acceptor state of the Sb donor-vacancy associate. This identification is based on observations showing that the introduction rate scales with the doping level in oxygen lean samples[24] and by analogy to silicon, in which the E-center and the divacancy are the most predominate defects in oxygen-lean wafers. Other studies focused on the variability of this defect depending on the group V impurity[28] and also confirmed that this peak is dopant related. The attribution to the second acceptor state is due to its small capture cross section (due to coulombic repulsion between the electrons) and the absence of a Poole Frenkel effect. However, there is no EPR confirmation of the identification of E_{37} as the E-center in germanium due to the difficulties of this technique in this material. The identification of E_{37} as a vacancy defect is therefore not as unambiguous as it is for the E-center in silicon. With this reserve in mind, we will keep using the ideas that E_{37} is the E-center and contains a vacancy in the following discussion, as we have until now. The properties of E_{37} measured in this work are compatible with its identification as the second acceptor state of the Sb-V pair. The high introduction rate and fast formation kinetics are a result of the large concentration of Sb sites as sinks for mono-vacancies. The high entropy of activation and temperature dependent cross-section indicate a bond rearrangement upon absorption/emission of a carrier which can result from the rearrangement of the defect to minimize the coulombic repulsion between two electrons upon transition from a singly to doubly occupied state. As shown in Figure 17, the decay of E_{37} proceeds at a constant rate regardless of fluctuations in the concentrations of the other defects confirming that it contains a primary defect different from the other observed defect associates.

The smaller than Debye frequency prefactor of E_{37} (1.2×10^{6} s^{-1}) indicates removal of the defect by diffusion to a sink. From Eq. (1), the measured prefactor requires the defect to jump $\approx10^{7}$ sites to reach a sink. For a 3D random walk model:

$$\langle r^2 \rangle = 3Na^2. \tag{2}$$

Therefore, 10^{7} jumps correspond to a migration distance of approximately ~1 μm (with nearest neighbor distance, $a = 0.245$ nm). There are two possible sinks for E_{37}:

(1) The surface can act as a sink as was proposed by Fage-Pedersen et al.[25] However, diffusion to the surface would not result in first-order decay behavior nor the uniform depth profile observed after annealing.

(2) The sink can be an impurity present in the bulk of the material which is more consistent with our observations. Based on the required migration distance of 1 μm, the concentration of the sink would have to be ~10^{12} cm^{-3}, which is lower than the observed E_{37} concentration for doses higher than 5 Mrad. Our observation of a first order decay reaction likely means that the sink is not saturated after removal of E_{37}. Therefore, each sink site can possibly accommodate multiple reactants.

The measured activation energy for the decay of E_{37} is not compatible with the Sb migration activation energy measured by diffusion studies at higher temperatures.[31] Therefore, we can assume that it is not the E-center itself that diffuses, but the mono-vacancy, after dissociation of the E-center. Consequently, if we assume that the annealing of E_{37} is diffusion limited, it implies that the annealing coefficient is proportional to the diffusivity of the mono-vacancy times the probability of dissociation of the E-center. In this case, the annealing activation energy is the sum of the activation energy of diffusion (migration energy, E_m) plus the activation energy of dissociation (binding energy, E_b), $E_a = E_m + E_b$. The binding energy contains a coulombic interaction as well as additional contributions. Therefore we can estimate a lower bound for the binding energy from just the coulombic interaction between the dissociating species from

$$E_b = \frac{1}{4\pi\epsilon}\frac{q_1 q_2}{r} , \tag{3}$$

where q_1 and q_2 are the charges of Sb and the vacancy, ϵ is the dielectric constant, and $r = 0.245$ nm is the interatomic distance, which we assume separates the charges. An upper limit on the value of the migration energy can then be roughly approximated from the difference in our measured activation energy and our estimated binding energy. At the temperature of annealing, the E-center is in the single acceptor state and DFT calculations[32] predict the mono-vacancy to be singly negatively charged. This yields two scenarios. If we assume that the vacancy is doubly negatively charged upon dissociation, then we find a value of 0.75 eV for the binding energy of the E-center which gives an experimental estimate for the migration energy of the mono-vacancy of < 0.04 eV. If before dissociation the E-center loses an electron, then the mono-vacancy is only single negatively charged during the dissociation, and the binding energy becomes 0.37 eV which yields an estimate of the migration energy of < 0.4 eV.

b) Interstitial associates: E_{30}, E_{22} and E_{21}

E_{30} is a defect that has been observed before but was not thoroughly characterized. Its measured energy level and annealing behavior are consistent with the defect $E_{0.30}$ reported by Fage-Pedersen et al.[25] Auret et al. [27] and Roro et al.[33] also report defects with similar states but real capture cross sections and annealing behavior were not reported. No defects with matching properties have been reported by Nagesh et al.[24] or Markevitch et al.[26] E_{21} and E_{22}, similarly to E_{30} have been observed before but were not the focus of the studies. The measured defect state and annealing behavior of E_{22} is consistent with $E_{0.23}$ reported by Fage-Pedersen et al.[25] and E_1 reported by Mooney et al.[23]. Its defect state also matches $E_{0.24}$ reported by Auret et al.[27] whose annealing behavior was not reported. It was not observed by Nagesh et al.[24] E_{21} matches the defect state of $E_{0.20}$ reported by Auret et al.[27] but its annealing kinetics were not reported. E_{21}'s defect state is close to Fage-Pedersen et al.'s $E_{0.19}$ and $E_{0.21}$ but the annealing kinetics do not match perfectly. In addition, Fage-Pedersen et al. does not observe $E_{0.21}$ for all doping concentrations tested. It is important to remember that Fage-Pedersen et al. reports more defects than other groups in the literature and does not systematically observe them in all the wafers tested. Due to their use of higher energy irradiation sources, different numbers of defect states would be expected when compared to this study. E_{21} is not observed by Nagesh et al.[24] or Mooney et al.[23]

Based on the assumption that the E-center captures all the mono-vacancies and the observation of coupled annealing reactions, we have concluded that these three defects contain interstitials. However none of these defects are likely the self-interstitial; they are not present immediately after the irradiation at 77 K and their concentrations initially grow after irradiation (Figure 15). Calculations have shown that self-interstitials can exist in multiple configurations[34] (D, H, T, hybrid, etc.) which can each have distinct defect states in the bandgap. Defects associates containing interstitials can also undergo a change in configuration upon change of charge state which is why interstitial associates typically have a large entropy of ionization, as observed for E_{21}. Therefore, in addition to dissociation, transitions occurring in a single jump can possibly be transformation of an associate from one configuration into another with a different defect state. Studying the conversion these defects states undergo during anneals at various temperatures (subject of the next sections) will allow us to investigate whether these states are different configurations of the same associate.

1. Transformation of E_{22} to E_{21}

From the series of high temperature isothermal anneals, we showed that the decay of E_{21} and the growth of E_{22} are coupled (similar activation energy and prefactor for growth and decay reactions as well as the saturation of E_{21} once E_{22} has annealed out). In order to further investigate the link between these defects, their conversion ratio, ($\Delta E_{21}/-\Delta E_{22}$), has been estimated as a function of the annealing temperature in Table III. The data is noisy but appears to be temperature dependent. These ratios are: (a) more than one, (b) less than two, and (c) increase with increasing temperature. Point (a) shows that there is possibly more than one interstitial in E_{22} because there cannot be a conversion ratio higher than the ratio of primary defects per defect. Point (c) shows that there is an activation barrier to the conversion indicating that some interstitials are lost to sinks (surface, impurity, and/or vacancies from dissociation of E_{37}) upon annealing at lower temperatures. Point (b) suggests a saturation of the ratio at two which means that the conversion rate likely cannot be higher than two. It is therefore possible that E_{22} contains two interstitials and E_{21} only one. However, E_{22} containing two interstitials does not mean that E_{22} is the di-interstitial because this reasoning does not rule out the possibility that it is a di-interstitial impurity associate.

The conversion of E_{22} into E_{21} is characterized by a large prefactor, higher than the Debye frequency which is a sign that the limiting step of the transformation consists of a single jump. The larger than the Debye frequency magnitude can be caused by an entropic effect; if the defect transformation results in an increase in entropy, the measured prefactor contains an $\exp(\Delta S/k)$ term. A value of ~2.5k can explain the discrepancy between the annealing prefactor and the Debye frequency. This is consistent with the interpretation that E_{22} contains two interstitials, which implies a large change of configurational and vibrational entropy upon transformation into two E_{21}.

Further evidence that E_{22} contains two interstitials is presented in Figure 19 which shows the number of countable interstitials after room temperature annealing for the sample irradiation in liquid nitrogen, assuming that the E_{30} and E_{21} contain one interstitial and E_{22} contains two interstitials. During the second annealing stage, the total countable interstitial concentration does not vary as expected; if all interstitials are paired with defects, then changes in defect concentrations only occur due to transformations from one defect into another. In addition, the assignment that E_{22} contains multiple interstitials is consistent with its small entropy of ionization compared to E_{21}'s. We might expect that a defect containing multiple interstitials is more configurationally constrained compared to an associate which contains a single interstitial resulting in a smaller entropy of ionization for the multiple interstitial containing defect.

Table III. Conversion ratio of E_{22} to E_{21}

$\Delta E_{21}/(-\Delta E_{22})$	85 °C	93 °C	104 °C	114 °C	126 °C
Average	1.44	1.47	1.59	1.99	1.93
Std. Dev.	0.064	0.09	0.30	0.007	0.15

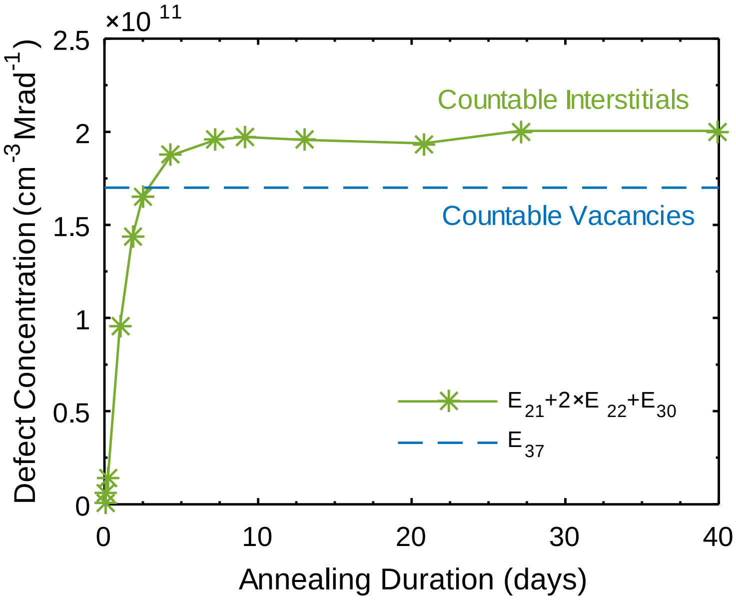

Figure 19. Concentration of interstitials contained in the defects we observe during room temperature (300 K) annealing of Ge irradiated at 77 K by ^{60}Co. If we assume that E_{21} and E_{30} only contain one interstitial and E_{22} contains two, after ~6 days the number of countable interstitials is constant as the defects evolve only by changing from one into another. Defect concentrations are normalized by the irradiation dose and are reported in units of cm^{-3}Mrad^{-1}.

2. Transformation of E_{30} to E_{22}

During the second annealing phase (Figure 15), E_{30} anneals out and fuels the growth of E_{22} but does not affect the concentration of E_{21}. If E_{30} dissociates and creates free self-interstitials, then both E_{22} and E_{21} should grow during the second annealing stage as occurs during the first stage. We propose two possible models to elucidate this problem: (a) dissociation then fusion: E_{30} releases its interstitials, they diffuse and, because of a higher activation barrier for the interstitial to form E_{21} rather than E_{22}, they associate with each other forming E_{22}; (b) diffusion then fusion: E_{30} transforms into E_{22} without dissociating. However, scenario (a) seems unlikely because E_{21} forms during the first stage of the growth when self-interstitials are available. Scenario (b) explains why E_{21} stops growing during the second phase of the annealing, but it also raises some questions. If E_{30} contains only one interstitial, then, assuming that E_{22} contains two interstitials, the transformation either requires one E_{30} to capture an interstitial or two E_{30} to fuse. The capture of interstitials by E_{30} is unlikely for the same reason that scenario (a) is unlikely; if self-interstitials are available for reaction, the concentration of E_{21} should also increase. The fusion of two E_{30} requires that the decay of E_{30} and the growth of E_{22} follow a second order reaction kinetics with the same reaction rate. Currently, there is not enough data to accurately determine the reaction orders for these defect reactions. However, the fact that E_{22} is initially absent during the first 10 hours of room temperature annealing following the liquid nitrogen irradiation but then outgrows both E_{21} and E_{30} indicates that the formation of E_{22} does not only involve self-interstitials. Therefore the presence of E_{30} might be necessary to the formation of E_{22}. This adds to the likelihood of requiring the fusion of two E_{30} in order to form E_{22}.

VI. Summary

The defects generated by ^{60}Co in 10^{15} cm^{-3} Sb-doped germanium were characterized using DLTS to determine their electronic properties. The observed defect assignments and annealing reactions are summarized in Figure 20. We observed four defects states which exhibit two distinct behaviors, which we attributed to their nature as either an interstitial containing or a vacancy containing defect. E_{37}, an Sb donor-vacancy associate, decays by dissociation and vacancy diffusion to a sink present in a concentration of 10^{12} cm^{-3}. E_{30}, E_{22}, and E_{21} account for the interstitials created after irradiation based on the observed formation kinetics and coupled annealing behavior. The conversion ratios of E_{30} into E_{22} and E_{22} into E_{21} suggest that E_{22} contains two interstitials. The formation behavior of E_{22} after irradiation in liquid nitrogen indicates that E_{30} is required for formation of E_{22}. Neither the mono-vacancy nor the self-interstitial could be directly observed, but their introduction rate due to ^{60}Co irradiation was found to be ~2×10^{11} cm$^{-3}\cdot$Mrad^{-1}.

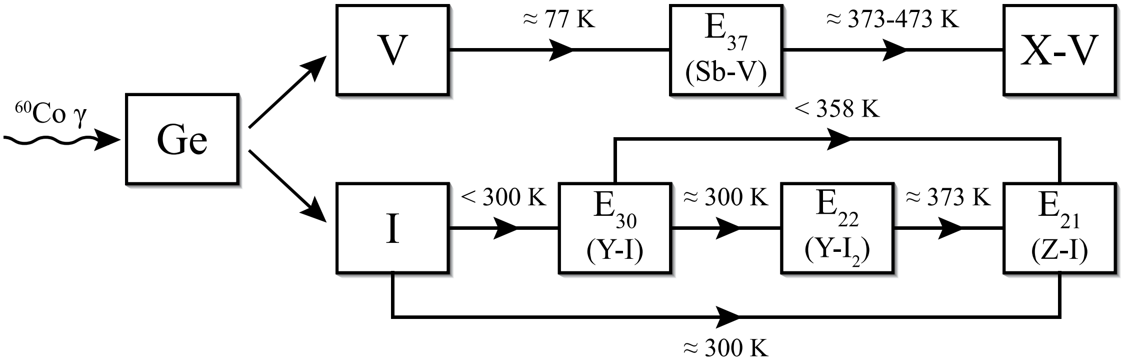

Figure 20. Schematic representation of defects in germanium generated by ^{60}Co irradiation and their reactions at various temperatures. X, Y, and Z stand for unknown sinks with which mono-vacancies, V, and self-interstitials, I, react.

Chapter 4. Point defects induced by a neutron and an alpha irradiation of n-type Czochralski-germanium

I. Introduction

To create more complex damage than simple mono-vacancies, self-interstitials and their associates, it is necessary to generate multiple displacements during the collision process. This is accomplished by irradiating with particles having a mass, as opposed to massless gamma ray. Due to the conservation of momentum, the heavier the particle, the easier it can transmit its energy to the nuclei during the irradiation and therefore the larger the collision cascade. For this work, we have used neutrons and alpha particles to generate complex point defects. In addition to their importance for the fundamental study of point defects in semiconductors, neutron and alpha particles (with electrons and protons) constitute most of the radiations in space and nuclear reactors. Therefore, it is also a crucial technological issue to understand how these particles can damage a material and how they can affect the properties of devices on-board instruments working in these extreme environments.

Neutrons have a mass of $1.7x10^{-27}$ kg and they can create much longer collision cascades than the Compton electrons generated by gamma irradiation. Because they don't have a charge, they don't undergo any coulombic interaction with the electronic cloud or the nuclei. They create damage by directly hitting the nuclei, which only occupy roughly 10^{-15} of the volume of the material. Therefore, collisions are scarce and the interaction length of neutrons with germanium is more than a centimeter, and the damage thus generated is homogeneously distributed in the 0.5 mm thick wafer samples used in this study.

The neutron source used in this work is the MIT nuclear fusion reactor. This facility produces two kinds of neutrons: slow ($E_K \approx 5$ eV, also called thermal neutrons) and fast neutrons ($E_K \approx 1$ MeV, also called kinetic neutrons), but can only filter out the fast one. When a slow neutron collides with a germanium atom, it does not have enough energy to generate a Frenkel pair. Instead, it is absorbed by the germanium atom to form non-stable isotopes by transmutation. After absorption of a neutron, multiple transmutations can occur, generating non stable isotopes that decay radioactively into stable atoms. Note that multiple isotopes of germanium exist in a stable form and we did not use wafers that were isotopically pure. For such "normal" germanium samples irradiated by thermal neutrons, around 30% of the neutrons are captured by ^{70}Ge, forming the radioactive ^{71}Ge, which decays into ^{71}Ga by emitting gamma rays, with a half-life of 12 days[35]. Other radioactive transmutations have much shorter lifetimes. This has two consequences: 1) changing of the doping level of the sample and 2) defect profiles similar to a ^{60}Co gamma ray irradiation. Fast neutrons on the other hand create large collision cascades until they have lost enough kinetic energy and have become thermal neutrons. For the study of defects more complex than those generated by ^{60}Co gamma rays, only fast neutrons are of interest and the influence of slow neutrons needs to be taken into account to analyse samples irradiated at the MIT nuclear fusion reactor.

Alpha particles are helium nuclei. They have a mass four times higher than the neutron and twice the charge of an electron (with the opposite sign). Contrary to neutrons, they lose their energy in a two-step process. When they have a lot of kinetic energy, they are slowed down by coulombic interaction with the electronic cloud of the material. It is the electronic stopping regime, in which the alpha particle loses a certain amount of energy per distance travelled but creates little displacement damage. Because collision events are rare in this regime, the defects generated are uniformly distributed. As the ions slow down, their collision cross-section increases up to the point when collisions become likely. When it happen, the ions lose their remaining energy very quickly through a collision cascade: this is the nuclear stopping. Nuclear stopping is triggered once the energy of the alpha particle passes below a certain threshold, which means that, for an energetically mono-dispersed beam of particles, all of them will experience it at roughly the same depth. Hence, when a charged particle is irradiated into a material, three zones appear: a zone close to the surface with some damage uniformity where electronic stopping dominates, a highly defective zone with large fluctuation of defect densities where nuclear stopping dominates and around which the irradiated ions are located, and finally a defect free zone past the implantation peak. These three areas are highlighted in Figure 21, which is a Monte-Carlo simulation of an implantation of alpha particles in germanium, generated by the software *Stopping and Range of Ions in Matter* (SRIM [36]). SRIM is a powerful tool to predict the position of the implantation peak. The implanted ion profiles during an irradiation are complex and do not have an analytical expression, so SRIM also provides the four first statistical moments of the distribution: average position (range), straggle (standard deviation), skewness and kurtosis. The distribution of the irradiation damage is more approximate than the ion profiles because SRIM does not take into account defect build-up nor the diffusion and transformation of defects. Finally, note that there is some nuclear stopping (and damage generated) even in the zone where electronic stopping is dominant because the collision cross-section is small but not zero. The irradiation performed for this doctoral work was performed at Pacific Northwest National Laboratory (PNNL) in a Van der Graaf accelerator, which allowed a tight control of the dose and energy (and thus range) of the irradiating alpha particles. In this work, we have used 6 MeV alpha particles, with a range of 30 µm. At the doping level of our material, the depletion region only extends a few nanometers deep, ensuring that only the electronic stopping region and its homogeneous defect profile is probed by DLTS using our Schottky diode structure.

Both alpha particles and neutrons create damage in the irradiated germanium by moving the lattice atoms in the nuclear stopping regime. A simple binary collision model predicts that more energy can be transmitted during a collision with a heavier particle than, which is why alpha particles could be expected to create more damage than neutrons. However, it is not the case in practice because the collision mechanisms of an alpha particle and of a neutron with a germanium atom are different. A neutron has no charge. It therefore only interacts with the germanium atoms by directly colliding with the nucleus, which results in rarer collision events, but larger collision cascades. Alpha particles on the other hand have a charge and interact with the germanium nuclei by a longer distance coulombic repulsion before an eventual direct collision. As a result, an alpha particle/germanium collisions results in more low angle scatterings, smaller momentum and energy transfer, and smaller collision cascades than a neutron collision. This longer range coulombic interaction is also the reason why the cross-section of alpha particles is higher than a neutron cross-section (the cross-section of a 1 MeV neutron is $\sigma=4\text{x}10^{-28}$ cm^2 [37]. An alpha particle of the same energy in the nuclear stopping regime (attenuation coefficient is 10 $\text{MeV.cm}^2.\text{g}^{-1}$[38]) has a cross-section of $\sigma=1\text{x}10^{-22}$ cm^2).

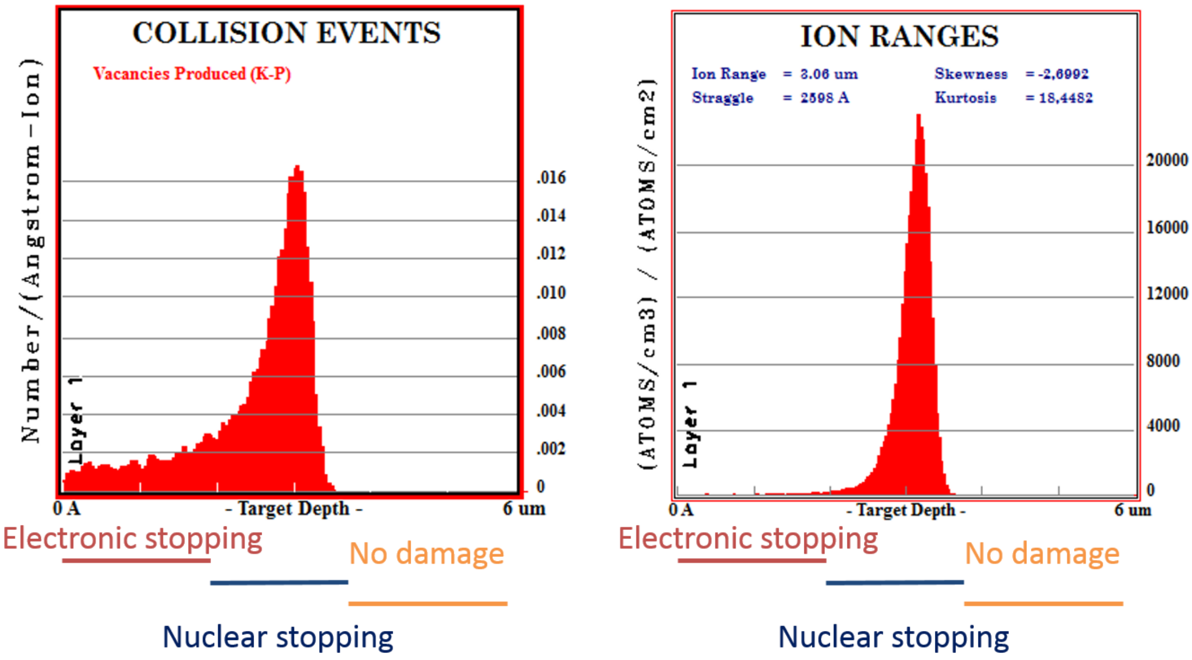

Figure 21: Vacancies produced and ion distribution after the irradiation of germanium by 1 MeV alpha particles, as a function of depth from the implanted surface, calculated by SRIM[36]. Three zones are apparent where electronic or nuclear stopping dominate and where there is no damage.

II. Electronic characterization

The DLTS spectra resulting from neutron and alpha irradiations (Figure 22) include the peaks observed after a ^{60}Co gamma irradiation. In addition, multiple other peaks have been introduced and are too close to one another to differentiate them with conventional DLTS. There are two methods two separate the different peaks from one another. Either, changing the pulse width used for the scan, in order to isolate the peaks with the smaller capture cross-section (Figure 23), or using a deconvolution algorithm to sort out the different exponential component of a capacitance transient measured at a fixed temperature (Laplace DLTS). Combining these approaches, we were able to identify the various peaks present after the particle irradiations and this is how we could precisely show the position of the peaks in Figure 22. Their Arrhenius behavior is shown on Figure 24, with the same naming convention as for the gamma induced points (E_{XX} has an apparent activation energy 0.XX eV below the conduction band). An apostrophe sign means that the peak is not observed in the gamma irradiated sample. The asterisk on the gamma defect E^*_{30} is to underline the specificity of this peak: it is not stable at room temperature and will anneal out within a month by transforming into E_{22}, as was shown in the previous chapter. Because of the delay between the irradiation (alpha, neutron) and characterization of the samples, no E^*_{30} was observed in the alpha and neutron samples. However, it was most likely introduced by the irradiation and decayed below the sensitivity level by the time of the measurement. Note that in the following paragraphs, we will not discuss the properties of one of the defect E'_{12}, because its introduction rate is small and we only detected it above the sensitivity level of our apparatus for the highest doses of particles.

There is no consensus on the physical nature of these different defects in the literature, and, similar to the case of gamma irradiated germanium, each group that studied germanium irradiated by neutron and alpha particle reports slightly different peaks, except for two defects corresponding to E'_{29} and E'_{11} which are always observed. They are detected in neutron irradiated samples by Nagesh et al.[39] and Capan et al.[40], after electron irradiation by Markevich et al. [41] and Poulin et al.[42], after proton irradiation by Fage Pedersen et al. [43] and after alpha particle irradiation by Kolkovski et al. [44] Markevich et al. [41] and Roro et al. [45]. Because E'_{29} is absent after a gamma irradiation (that only creates single displacements), it has been claimed that E'_{29} might be the divacancy. However, this identification seems premature as the argument that it does not appear after a gamma irradiation only suggests that is contains multiple interstitials and vacancies, but does not indicate which or how many. In addition, Density Functional Theory (DFT) studies of the divacancy level predicts that there should be none in the higher part of the germanium bandgap [46] and some other studies on both sides of the gap even affirmed that there is no state corresponding to the divacancy at all at room temperature [47]. For high doses of alpha particles, Kolkovski et al. [44] have identified a defect whose concentration scales strongly with dose similarly to E'_{24}. The other defects that we have detected (E'_{27}, E'_{19} and E'_{23}) have not been consistently reported. This might be due to their proximity with two large peaks (respectively E_{37} and E_{22}) which hide their presence in a conventional DLTS scan and make their detection difficult even when using Laplace DLTS.

Using pulse width variation methods, we were able to measure the real capture cross-section of the different peaks. The capture rate of carriers by a defect is related to its capture cross-section by Equation 14, which translates into an exponential filling of the defect (Equation 15). However, this last equation only holds if the capture cross-section is time independent. This is not always true: for instance if the filling of a trap slows done the capture rate of other traps. This can happen when defects are in close proximity: either in clusters [48] or in dislocations [48], [49], because when one defect captures a carrier, it changes its charge state, therefore creating an electrostatic field that can affect the neighboring traps. In this case, the capture of electron is logarithmic. Some of the defects that we are considering in this study are created within a collision cascade and one of them exhibits this behavior. Figure 25 shows the filling of a trap whose capture process follows Equation 15. If we apply the same equation for a time dependent capture cross-section trap, we obtain Figure 26: the constant capture cross-section hypothesis breaks down. In this case, a logarithmic capture happens (Figure 27), as expected. E'_{11}, E'_{15} and E'_{24} presents this logarithmic capture process. Moreover, they have a low capture cross-section compared to the other defects with a similar position in the bandgap (especially E'_{27}, E'_{29} and E'_{23}): their capture cross-section decreasing over time is also due to the influence of the other defects. Table 4 synthetizes the information provided by the measurement of real capture cross-section (cf. Methodology): capture cross-section prefactor and energy dependence, real enthalpy and entropy of ionization. In the case of a logarithmic capture process, we are reporting the capture cross-section as measured for smaller pulse widths. For such pulses, most defects are not filled and the coulombic interaction between filled and empty trap is smaller. However, the precision of the measurement suffers from the small intensity of the signal.

Of the defects observed after neutron and alpha irradiation, only E'_{29} has a temperature independent capture cross section. All the other defects have an activation energy barrier toward capture/emission. This barrier is especially high for E'_{27} and is larger than the enthalpy of ionization itself. Another peculiarity of E'_{27} is its huge negative entropy of ionization: the entropy of the trap is higher when it is filled. Therefore, the trap most likely undergoes a massive bonding re-arrangement upon ionization. In addition, because of this negative entropy of ionization, a peculiarity of E'$_{27}$ is that its free energy of ionization overlaps with E'$_{29}$ at 175 K: at this temperature, the emission rates of the two defects are the same.

$$c_n = \sigma v n \qquad \text{(Equation 14)}$$

$$n_{filled} = N_T\left(1 - \exp\left(-c_n t_p\right)\right) \qquad \text{(Equation 15)}$$

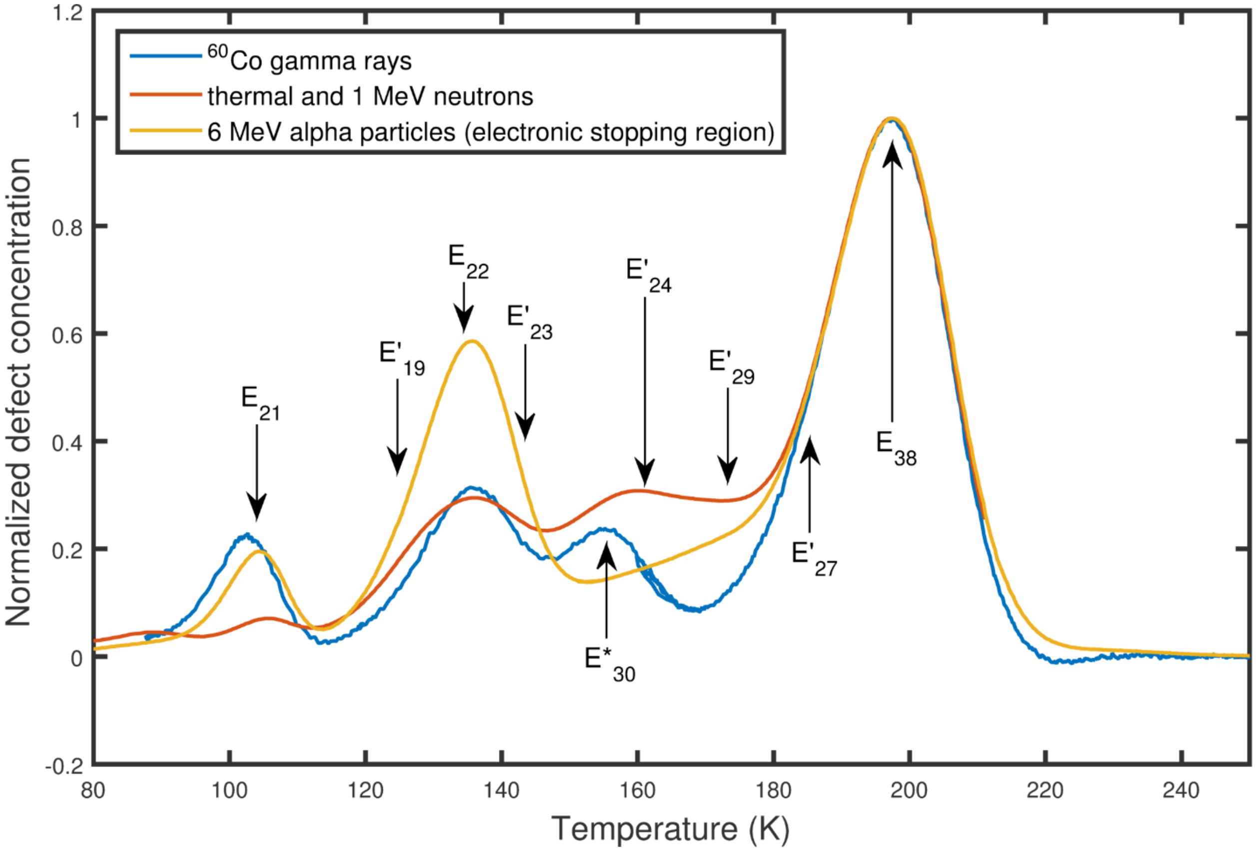

Figure 22: DLTS scan of ^{60}Co, neutron and alpha irradiated CZ germanium, with indication of the location of the different peaks identified, normalized by the concentration of E_{37}. E_{30}, highlighted with an asterisk, is unstable at room temperature and was absent at the time of the measurement due to the delay between the irradiation and testing. The reverse bias, pulse bias, pulse duration and rate window are respectively -5 V, 0V, 5 ms and 200 s^{-1}. The dose of alpha particles is 5x10^{8} cm^{-2} at an energy of 6 MeV. The dose of 1.1 MeV neutrons is 10^{13} cm^{-2}.

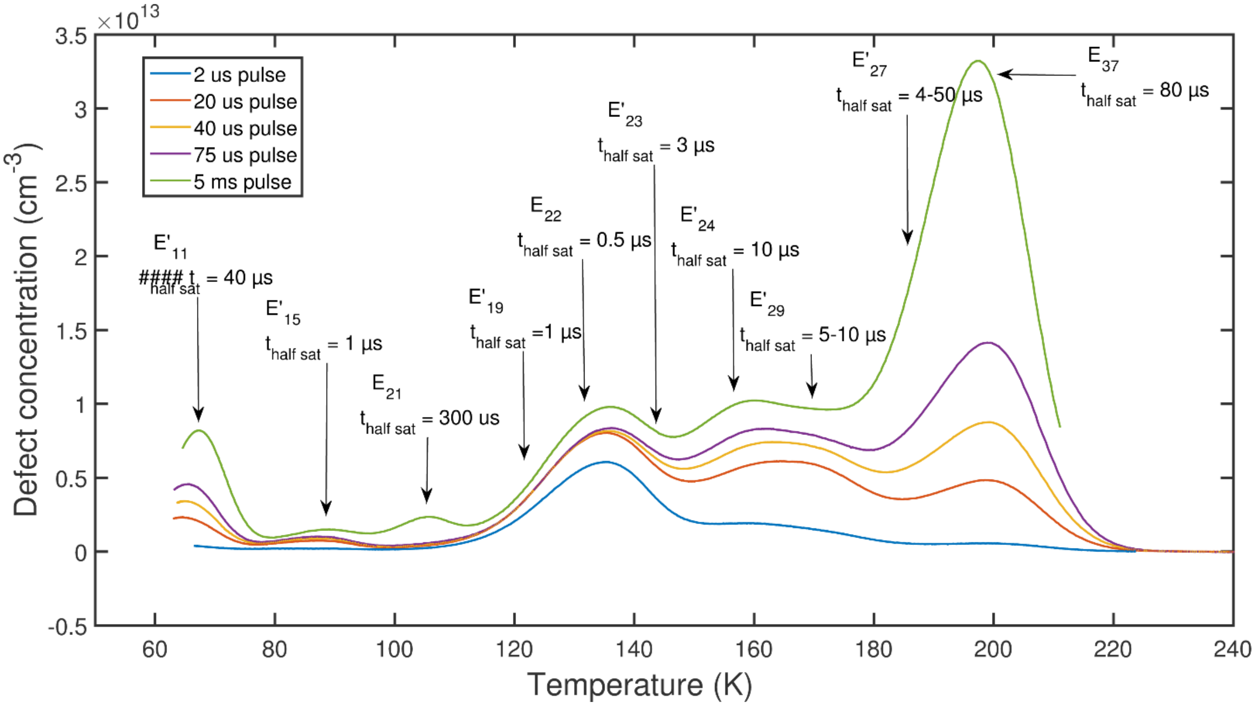

Figure 23: DLTS spectra of a 10^{-13} cm^{-2} thermal and 1.1 MeV irradiated germanium sample, for different pulse lengths

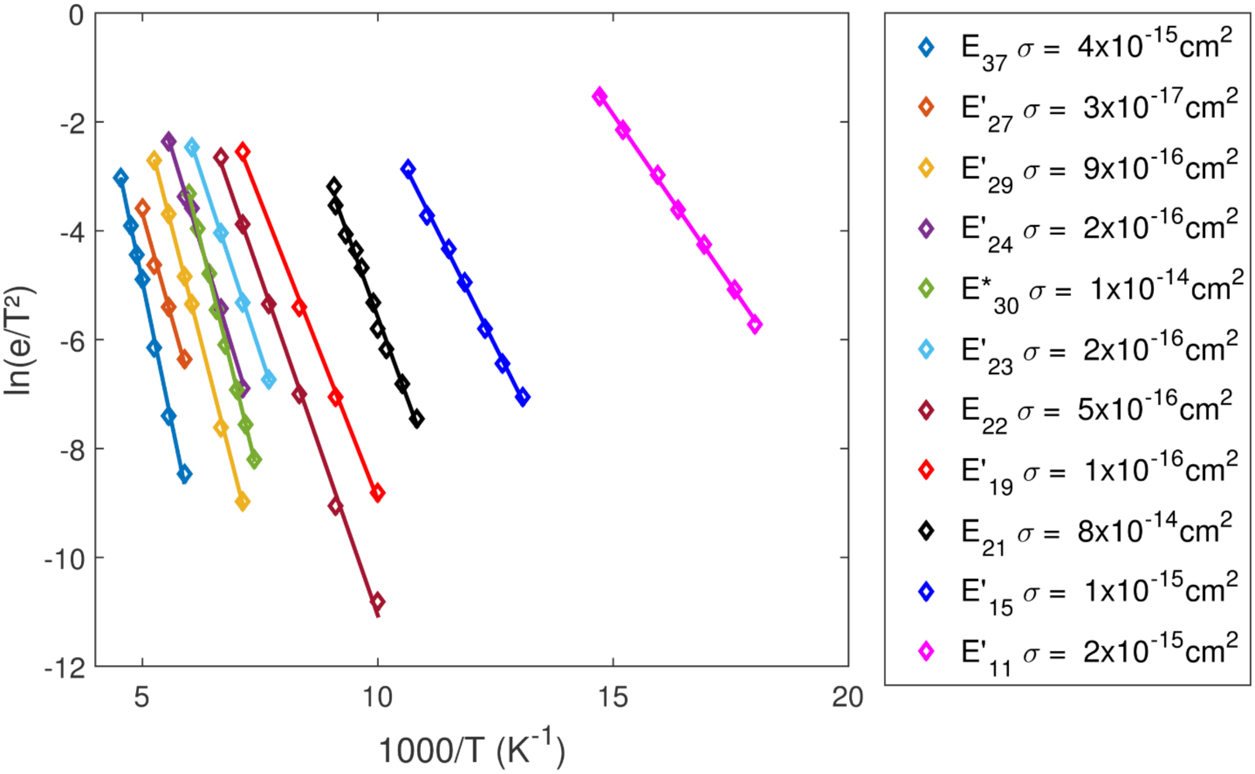

Figure 24: Arrhenius behavior of the different defects observed in the neutron and alpha irradiated samples.

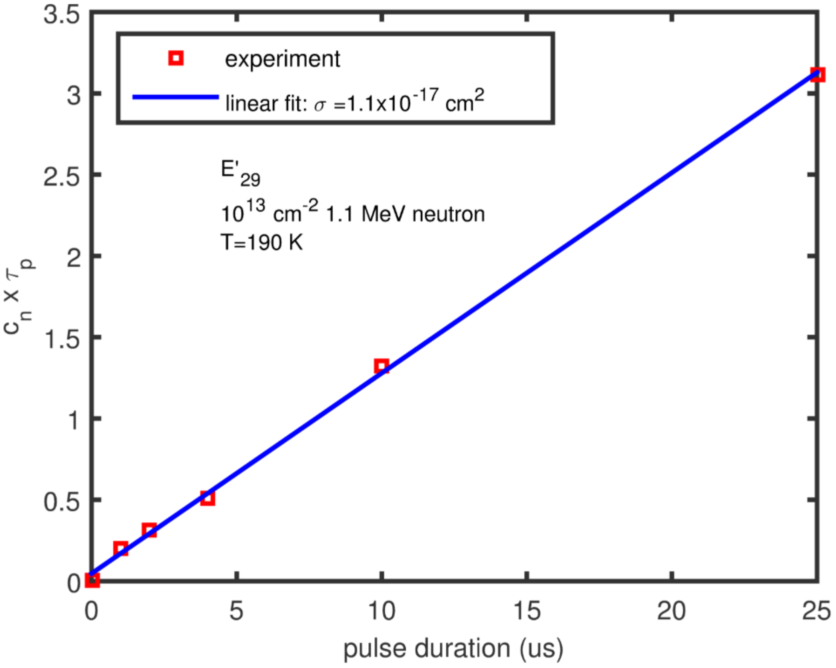

Figure 25: Calculation rate time pulse duration for E'$_{29}$. This defect has an ideal behavior, with a time-independent capture cross-section

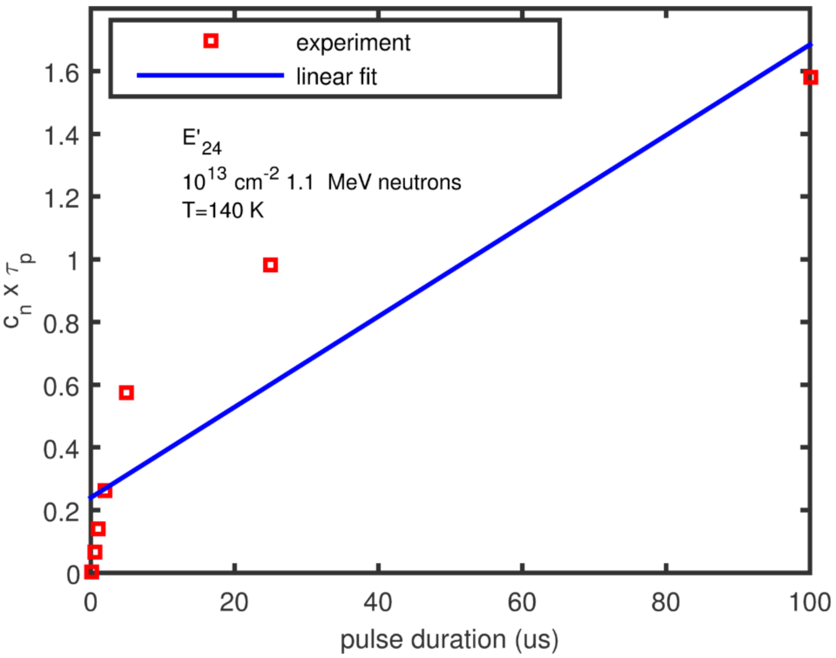

Figure 26: Calculation rate time pulse duration for E'$_{24}$. The capture cross-section of this defect is time-dependent and the fit to Equation 13 and to Equation 15 is poor.

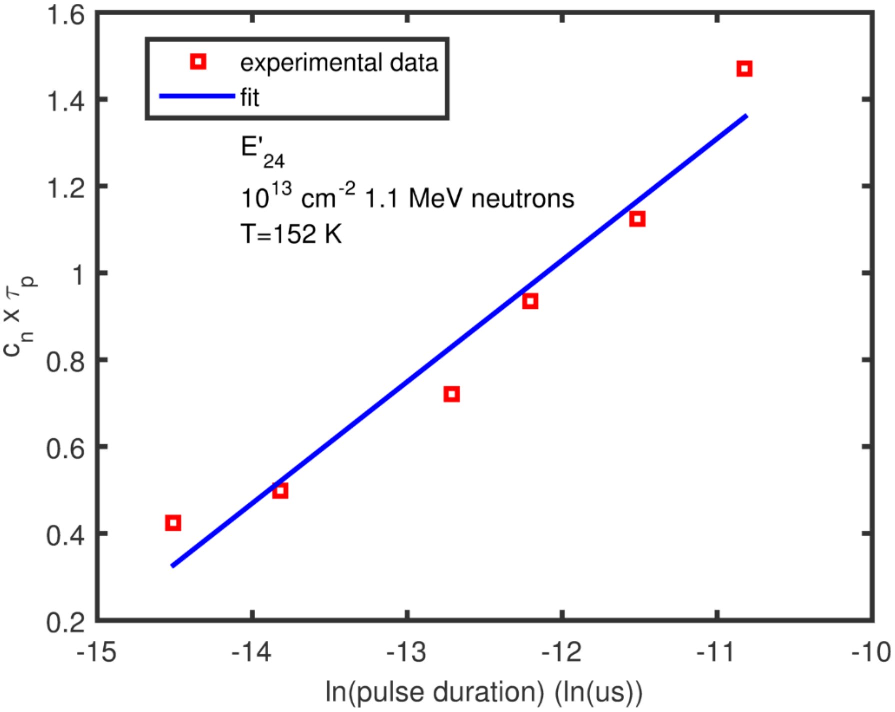

Figure 27: Calculation rate time pulse duration as a function of the logarithm of the pulse duration. A logarithmic capture cross-section is the signature of a defect in a cluster or in a dislocation.

defect name	**apparent activation energy (eV)**	**apparent cross-section (cm^2)**	**Logarithmic Capture cross-section**	**Real cross-section at e_m=200s^{-1} (cm^2)**	**real cross-section prefactor (cm^2)**	**cross-section activation energy (meV)**	**real free energy (eV)**
E_{37}	0.37	3.90E-15	✗	6.40E-19	7.60E-17	85	0.29-3.94 kT
E_{30}	0.3	1.20E-14	✗	>1e-15	>1e-15	NA	NA
E_{22}	0.22	4.60E-16	✗	1.10E-16	1.10E-16	0	0.22-1.53 kT
E_{21}	0.21	8.00E-14	✗	3.60E-20	2.00E-17	54	0.16-8.29 kT
E'_{27}	0.27	3.00E-17	✗	2.40E-18	1.50E-14	142	0.13+6.22 kT
E'_{29}	0.29	9.00E-16	✗	1.10E-17	1.10E-17	0	0.29-4.4 kT
E'_{24}	0.24	2.00E-16	✓	1.50E-18	5.50E-17	16	0.22-1.29 kT
E'_{23}	0.23	2.00E-16	✗	1.70E-17	1.30E-16	24	0.2-0.43 kT
E'_{19}	0.19	1.00E-16	✗	7.70E-17	4.20E-16	17	0.17+1.44 kT
E'_{15}	0.15	1.00E-15	✓	2.2E-18	2.2E-18	0	0.15-6.1 kT
E'_{11}	0.11	2.00E-15	✓	2.5E-18	2.5E-18	0	0.11-6.7 kT

Table 4: Electronic properties of the alpha and neutron induced defects.

III. Introduction rate of the defects

a) Dose effect in alpha particle irradiated germanium

In addition to the electronic signature of the point defects, we can gain an insight into their nature by investigating their introduction rate: how the choice and the dose of irradiating particles affect the defect profiles. In this section, we will investigate how the defect concentration scales with the dose of 6 MeV alpha particles. We have tested doses up to 5x10^9 cm^{-2} of 6 MeV alpha particles. For doses above 10^9 cm^{-2}, the number of defects generated is on the order of 10% of the doping level. When this happens, the filling and emptying of traps during a DLTS measurement induce large changes of the width of the depletion region. It follows that the system is not in a "small signal" regime, and the formula used for the determination of defect concentration from the amplitude of the capacitance transient breaks down. Therefore, the defect concentrations measured for the 5x10^9 cm^{-2} dose have a larger uncertainty.

Figure 29 shows DLTS profiles of germanium samples irradiated by 6 MeV alpha particles in doses ranging from 1x10^8 cm^{-2} to 5x10^9 cm^{-2}. The profiles have been normalized to the concentration of E_{37}, in order to allow the comparison of profile shapes despite the large difference in absolute defect concentration. The profiles of the samples that received 1x10^8 cm^{-2} and 5x10^8 cm^{-2} are similar, but they both differ strongly from the 5x10^9 cm^{-2}. E_{37} is not the dominant defect in the highest dose alpha-irradiated sample, with E'_{23} having a higher concentration. Such shift of major defect has been observed by others [44] and is characteristic of the defect profile after a high dose alpha particle implantation. This is because this defect is a secondary defect, forming by association of two other defects, and its introduction rate scales supra-linearly with dose, as will be shown in the following paragraph.

Using Laplace DLTS, we are able to estimate the concentration of the different defects present more precisely than using a conventional DLTS scan, which allows us to evaluate introduction rates. As can be seen in Figure 30, for low doses**,** the introduction rate of E_{37} is linear, similar to what was observed after a gamma irradiation. Neither E_{22} nor E_{21} have a linear introduction rate, consistent with their formation process**.** The non-linearity of E_{22} in particular is due to the complex mechanism (association of two E*30) that we identified after the study of cryogenic gamma irradiation of germanium. Of the defects observed following only an alpha or neutron irradiation, E'_{29}, E'_{24}, E'_{19} E'_{11} also have a linear introduction rate, as shown in Figure 31. They are therefore primary defects created either during a collision event, or after a short diffusion to a high concentration sink. Because they don't appear in the gamma irradiated samples, we can infer that they are created when multiple displacements happen simultaneously during the collision cascade, and hence contain multiple vacancies and/or interstitials. E'_{27} and E'_{23} are different (Figure 32: their introduction rates do not follow a simple fit. A polynomial fit results $[E'_{27}]$~$Dose^{1.7}$ and $[E'_{23}]$~$Dose^3$. From these higher order dose dependencies we infer that a defect forms by the association of multiple primary defects. However, these exponents have a large uncertainty because they rely heavily on the trap concentration measured after an alpha irradiation with dose 5x10^9 cm^{-2}, which is imprecise due to the deviation from the small signal regime. The higher order introduction rates hint that E'_{27} and E'_{23} form by the association of other less stable primary defects. In addition, the scaling laws suggest that E'_{27} contains two primary defects and E'_{23} contains three, but this is highly speculative given the uncertainty pertaining to the determination of the exponents.

b) Difference between the alpha, gamma and neutron induced defect profiles

The profiles obtained after gamma, alpha or neutron irradiations are qualitatively different (Figure 22). Even if they are all dominated by the vacancy donor complex E_{37} (with the exception of the samples irradiated by the highest dose of alpha particles, which will be described in detail in a different section), the relative intensity of each peak is affected by the nature of the irradiation. For instance, E_{21}'s relative introduction rate is smaller in the neutron irradiated sample, while E_{22}'s is higher in the alpha irradiated sample. The peaks in the 140 K region of the spectra are more developed in the neutron irradiated sample than in the alpha (and are absent in the gamma irradiated sample). These variations are due to the difference of interaction between the incoming particle and the atoms of the lattice, which impacts the extent of the collision cascade.

When comparing profiles due to gamma, alpha and neutron irradiated germanium, a subtlety regarding the neutron sample needs to be taken into account. Their spectra are the result of the irradiation by both thermal and 1.1 MeV neutrons, because the nuclear reactor at MIT does not allow for the irradiation of only high energy neutrons. However, thermal-neutron-only irradiations are possible, allowing us to estimate what defect is due to what kind of neutron. DLTS spectra of thermal-only, thermal and fast, as well as "fast only" (obtained by subtraction of the two others) neutron irradiated sample are presented in Figure 28. A striking feature of this graph is that most of E_{22} and E_{21}, two of the peaks observed in gamma irradiated germanium, are mostly introduced by the thermal neutrons (more precisely by the gamma rays emitted after the transmutation of the unstable isotopes of germanium. This is the reason why the thermal neutron DLTS profile looks similar to a ^{60}Co gamma ray profile, even if the gamma rays involved do not have exactly the same energy). From the gamma irradiation study, we have determined that E_{22} is a di-interstitial defect and E_{21} is a single interstitial defect, and that they account for all the interstitials introduced by the irradiation, while E_{37} accounts for the vacancies. During a displacement event, interstitials and vacancies are generated in equal proportions: the lack of E_{22} and E_{21} in a fast neutron irradiated sample requires that other interstitial defects have a large concentration to preserve the balance between interstitial and vacancy defects. This suggests that both E'_{11} and E'_{27} are interstitial defects.

Despite this difference regarding the introduction of E_{22} and E_{21}, the (low dose) alpha and neutron irradiated samples share a property: E_{37} has an introduction rate higher than the other defects, by an order of magnitude. Consequently, its concentration is a good way to assess the number of displacements occurring during the irradiation, and by extension to have an idea of the damage generated, independent of the extent of the collision cascade. This approach allows a more quantitative comparison of the alpha and neutron generated defects. Table 5 presents the defect concentrations measured using Laplace DLTS, for different doses of 6 MeV alpha and for a dose of 10^{13} cm^{-2} 1.1 MeV neutrons (the defect introduced by the thermal neutrons have been subtracted). Coincidentally, the concentration of E_{37} in the 5x10^{8} cm^{-2} alpha-irradiated and "fast only" neutron-irradiated samples are the same: both irradiations generate the same number of displacements. We can define the "neutron-to-alpha ratio" as the ratio of the concentration of a defect in the neutron irradiated sample divided by its concentration in the 5x10^{8} cm^{-2} alpha irradiated sample. It is a good measure of how much the neutron irradiation (and by extension the size of a collision cascade) favors the formation of some defects. By definition, it is 1 for E_{37}. For the primary defects, it is: 3.2 for E'_{29}, 4.7 for E'_{24}, 3.8 for E'_{19} and 10 for E'_{11}. A ratio higher than one indicates that the formation of such defects is favored by the neutron irradiation, which, as expected, creates more multiple displacement damage. With the exception of E'_{11}, the three defects have a similar ratio of roughly 4. This hints that the events that lead to their creation are equally probable and that the same number of displacements is involved in their generation. E'$_{11}$ has a higher ratio of 10. It benefits even more than the other defects from the larger collision cascade, which suggests that this defect contains more interstitials or vacancies than the three others. Using Occam's razor, we propose that E'$_{29}$, E'$_{24}$ and E'$_{19}$ each contain either two interstitials or two vacancies, and that E'$_{11}$ contains 3. From the balance between interstitial and vacancy defects, we have inferred in the previous paragraph that E'$_{11}$ is an interstitial defects, which thus makes it a triple interstitial. This assignment is consistent with the balance between interstitials and vacancies and both neutron and alpha particle irradiated samples, as long as out of E'$_{29}$, E'$_{24}$ and E'$_{19}$, two defects contain two vacancies, and one contain two interstitials

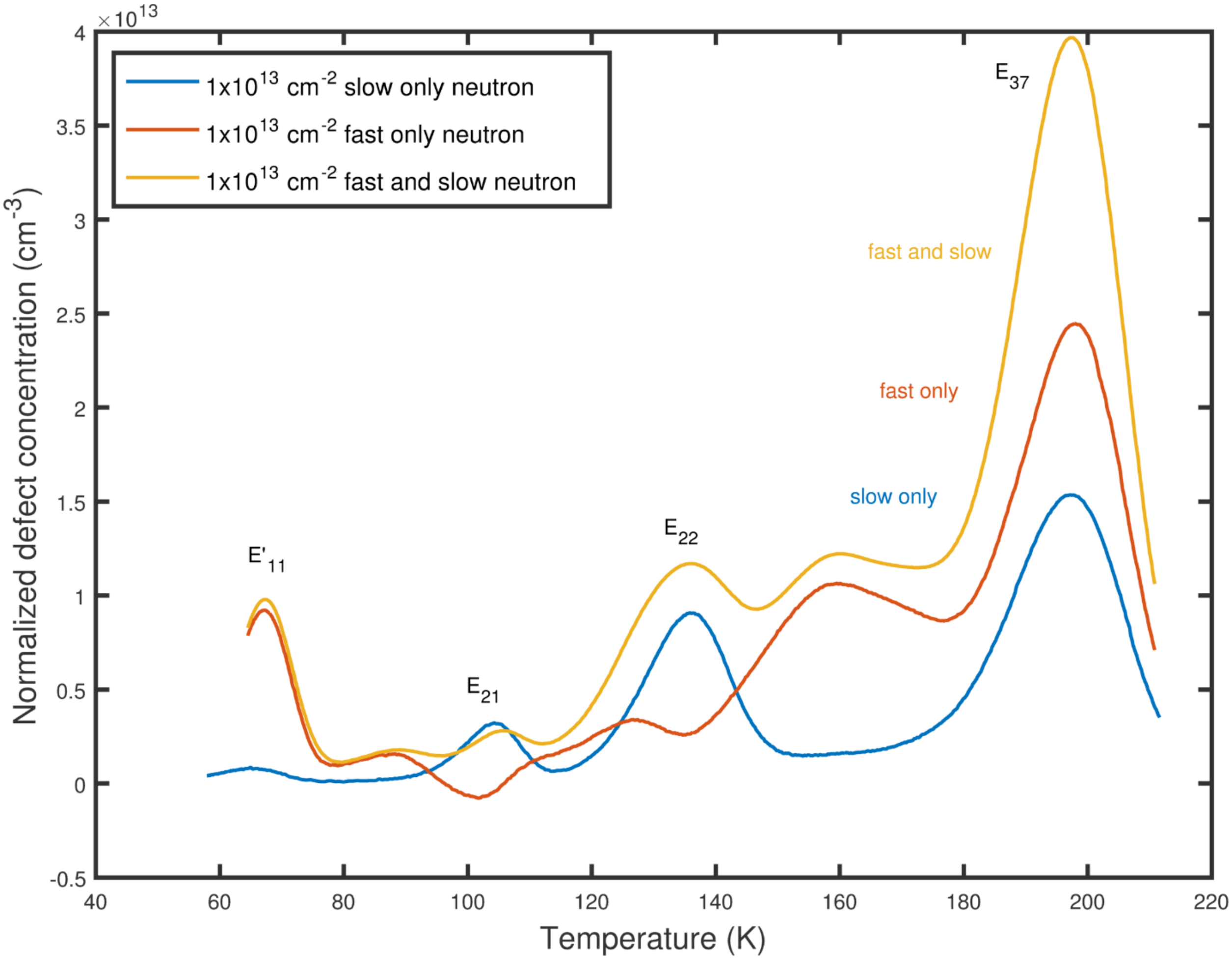

Figure 28: DLTS spectra after a slow neutron only irradiation and after a slow and fast neutron irradiation. The fast only profile is obtained by subtracting the former from the latter. The fast neutron irradiated samples lacks the peaks at 100K (E_{21}) and 135 K (E_{22}), which account for most of the interstitials in gamma and alpha irradiated material. Instead, there is a large concentration of E'$_{11}$. This scan was done at V_R=-5 V, V_P=0 V, t_p=5 ms and a rate window of 200 s^{-1}.

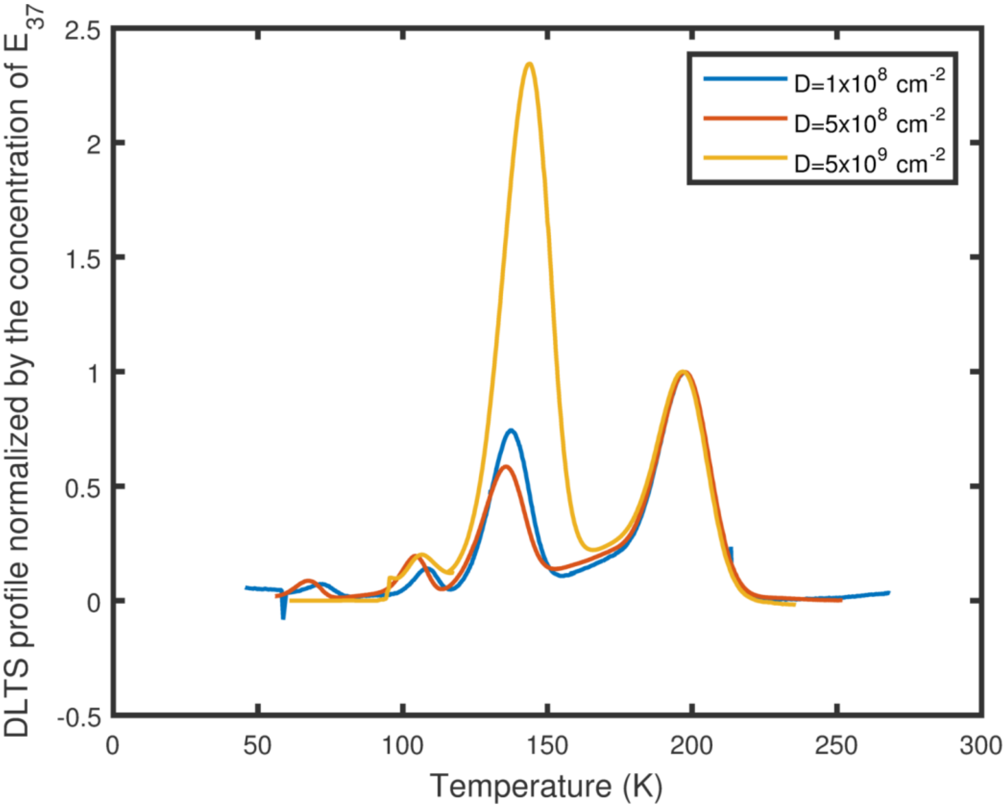

Figure 29: DLTS profiles after an irradiation by different doses of 6 MeV alpha particles, normailzed by the concentration of E_{37}. The defect population of the sample that received the highest dose of alpha particle is radically different from the others.

Table 5: Defect concentration (cm^{-3}) after irradiation of different doses of 6 MeV alpha particle and for a fast neutron irradiation (slow neutron defect concentration subtracted). A concentration of 0 cm^{-3} means that the concentration of the defect is below the DLTS sensitivity level.

peak name	$1x10^8$ cm^{-2} 6 MeV alpha	5 $x10^8$ cm^{-2} 6 MeV alpha	1 $x10^{13}$ cm^{-2} 1.1 MeV neutron	5 $x10^9$ cm^{-2} 6 MeV alpha (rough estimates)
E_{37}	4.24E+12	1.70E+13	1.70E+13	3.50E+14
E_{22}	3.50E+12	1.10E+13	0	2.50E+14
E_{21}	2.04E+12	2.50E+12	7.0E+11	7.30E+13
E'_{27}	0	4.10E+11	8.90E+12	2.00E+13
E'_{29}	5.00E+11	2.50E+12	8.00E+12	4.00E+13
E'_{24}	3.00E+11	1.50E+12	7.00E+12	3.30E+13
E'_{19}	1.00E+11	8.00E+11	3.00E+12	2.00E+13
E'_{23}	0	4.40E+11	2.00E+12	6.00E+14
E'_{15}	0	0	5.00E+11	0
E'_{11}	0	1.00E+12	1.00E+13	2.30E+13

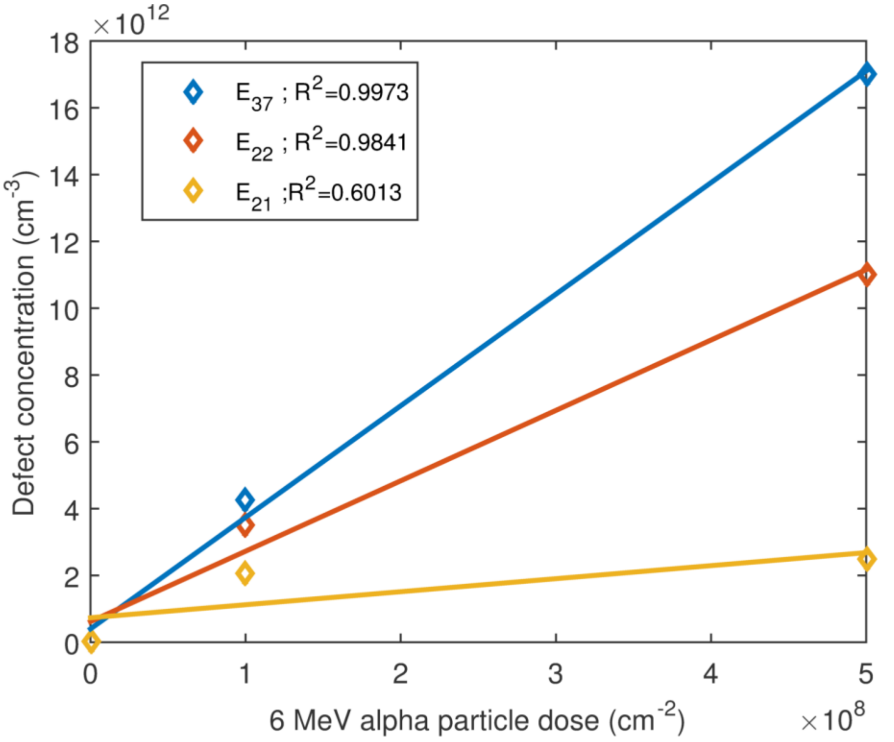

Figure 30: Concentration of E_{37}, E_{22} and E_{21} as a function of the dose of 6 MeV alpha particles. Only E_{37} has a linear introduction rate.

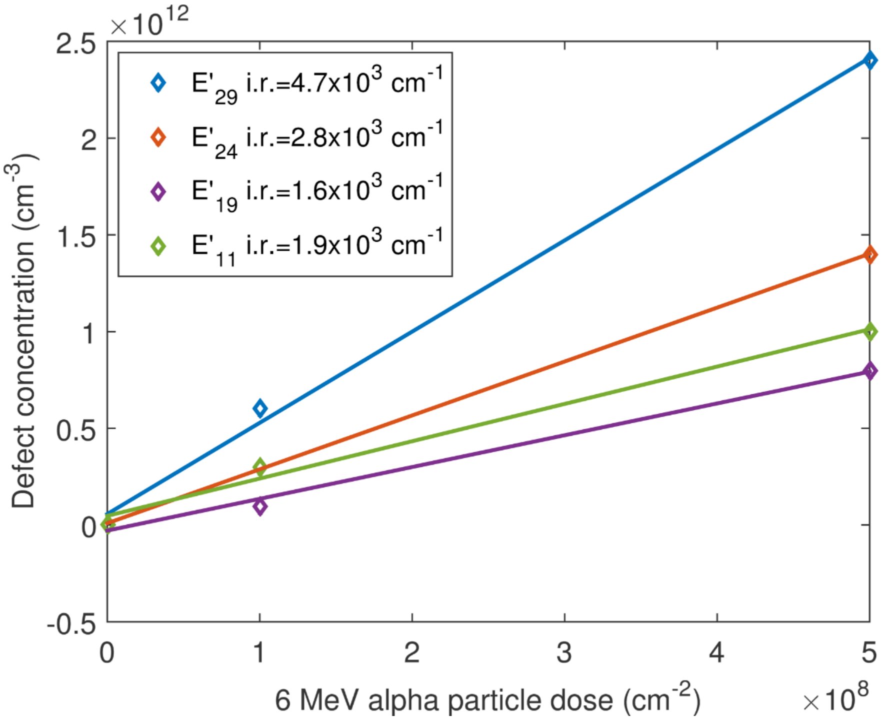

Figure 31: Concentration of E'_{29}, E'_{24}, E'_{19} and E'_{11} as a function of the dose of 6 MeV alpha particles. These defects have a linear introduction rate ("i.r." in the legend)

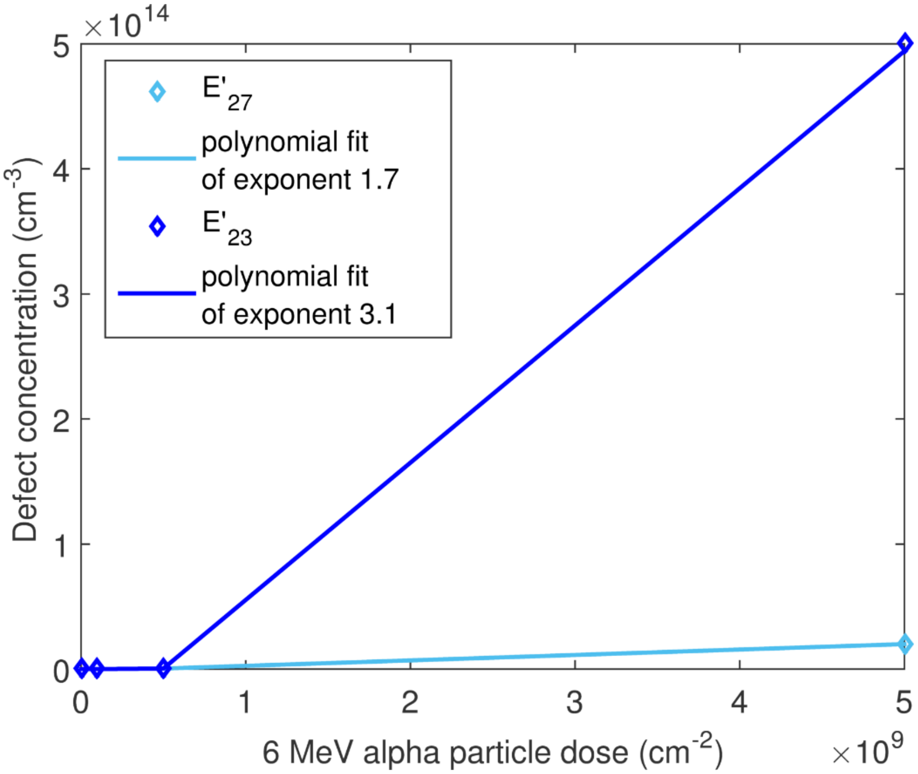

Figure 32: Concentration of E'$_{27}$ *and E'*$_{23}$ *as a function of the dose of 6 MeV alpha particles. The concentrations for 1x10*^{8} *cm*$^{-2}$ *are below the sensitivity level, and their concentrations are respectively 4.1x10*^{11} *cm*$^{-3}$ *and 4.4x10*^{11} *cm*$^{-3}$ *for a dose of 5x10*^{8} *cm*$^{-2}$*. These traps have a super-linear introduction rate, signature of secondary defects.*

c) Annealing study

In addition to their electronic properties and their introduction rates, an important attribute of point defects is their annealing behavior. After annealing of the alpha and neutron irradiated samples, no new defects appeared,some defects annealed out, or converted into one another. Figure 33 shows DLTS profiles after the 1 minute isochronal annealing of 5x10^{8} cm^{-2} 6 MeV alpha particle irradiated germanium. After these anneals, the concentration of all the defects decrease, except for E_{21} which increases. Similar to what we observed after the annealing of gamma irradiated material, the growth of E_{21} is concomitant with the disappearance of E_{22}. However, the defect transformation in the alpha irradiated material is not the straightforward one-to-two conversion of E_{22} to E_{21} characteristic of gamma irradiated germanium. Instead, the annealing of E_{22} and growth of E_{21} is also accompanied by the decrease of E_{37}. This behavior is clearer in the 113°C and 137°C isothermal DLTS profiles shown in Figure 34and Figure 35. Only the concentration of E_{21}, E_{22} and E_{37} have significantly changed after thermal treatment. The decrease of E_{37} is not driven by its intrinsic thermodynamic stability. If it were the case, a similar decay in this temperature range would have been observed in the gamma irradiated samples. Moreover, the decrease of E_{37} concentration stops once most of E_{22} has out-annealed, as is shown by the minimal change of concentration between the 5 and the ten minutes annealing, compared to the evolution observed between 1 and 5 minutes (Figure 34and Figure 35). It is not clear why the annealing relation between E_{21}, E_{22} and E_{37} is different in the case of the alpha and gamma irradiated samples. This might be due to the "cluster" nature of the defects formed after a neutron or an alpha particle irradiation. Contrary to a gamma irradiation which only generates single displacements far from one another, an alpha or neutron irradiation creates a collision cascades, a set of single and multiple displacements in close proximity. As a result, contrary to a gamma irradiation, after which the E_{22} formed by association of two single interstitial defects E^*_{30} can be situated far from the initial position of the Frenkel pair and of the E_{37}, after a neutron or alpha irradiation, multiple E^*_{30} are created in close proximity and there is no long range diffusion required for the formation of E_{22}. As a result, the average distance between E_{22} and E_{37} is much smaller and the interstitials released by the annealing of E_{22} might find and react with the vacancy of an E_{37} more easily.

Due to the convolution of the peaks, even the Laplace DLTS software has trouble determining the defect concentrations accurately enough to provide quantitative annealing kinetics. Qualitatively, all the defects introduced by alpha and neutron irradiations are stable up to at least 20 minutes at 137°C. After 1 minute at 202°C, the concentration of E'_{29}, E'_{24} and E'_{19} is roughly halved, while E'_{27} and E'_{23} does not change significantly.

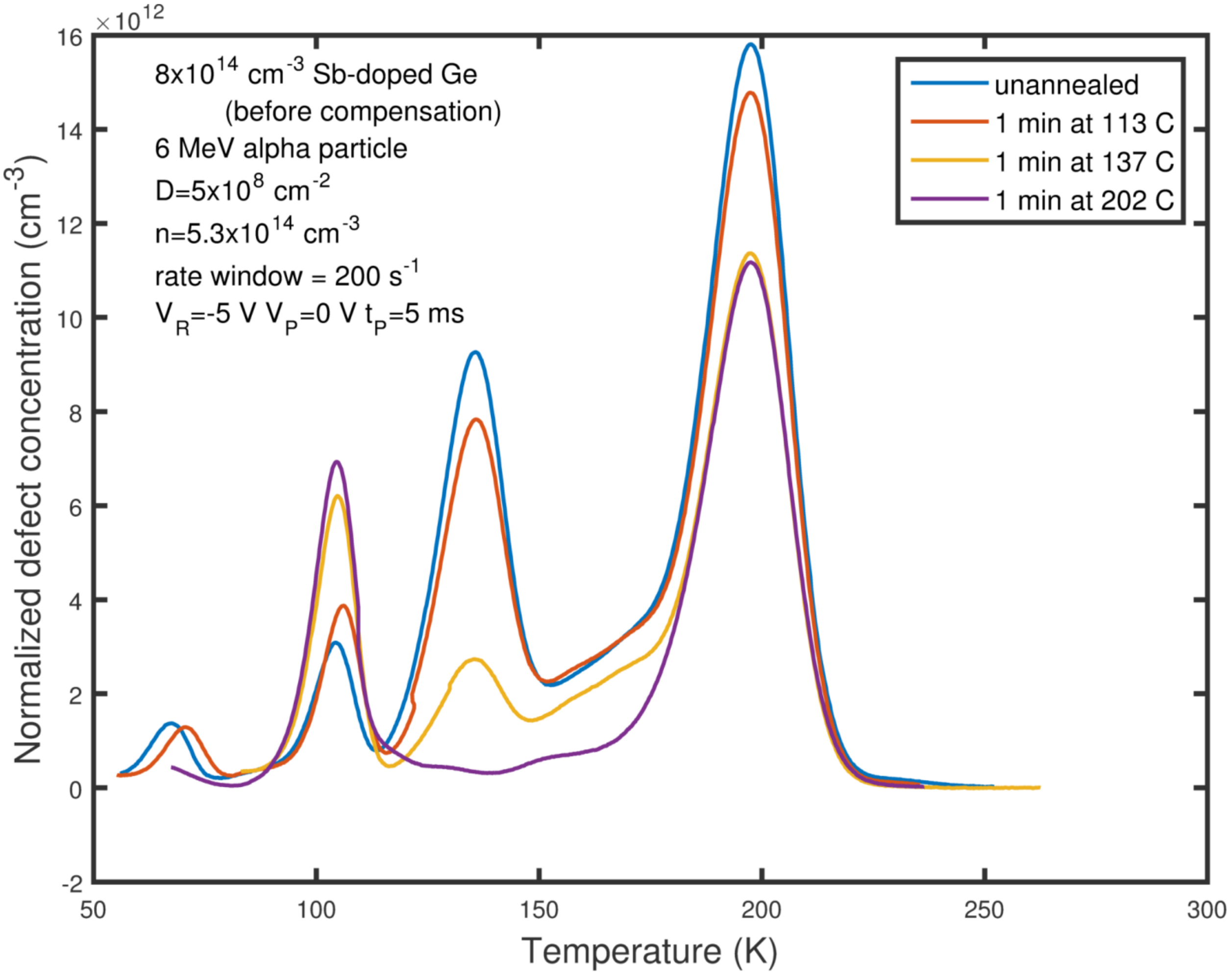

Figure 33: 1 minute isochronal annealing of germanium irradiated by $5x10^8$ cm^{-2} 6 MeV alpha particles. The annealing of E_{22} drives the growth of E_{21} and the decay of E_{37}. The other defects are stable up to 202°C.

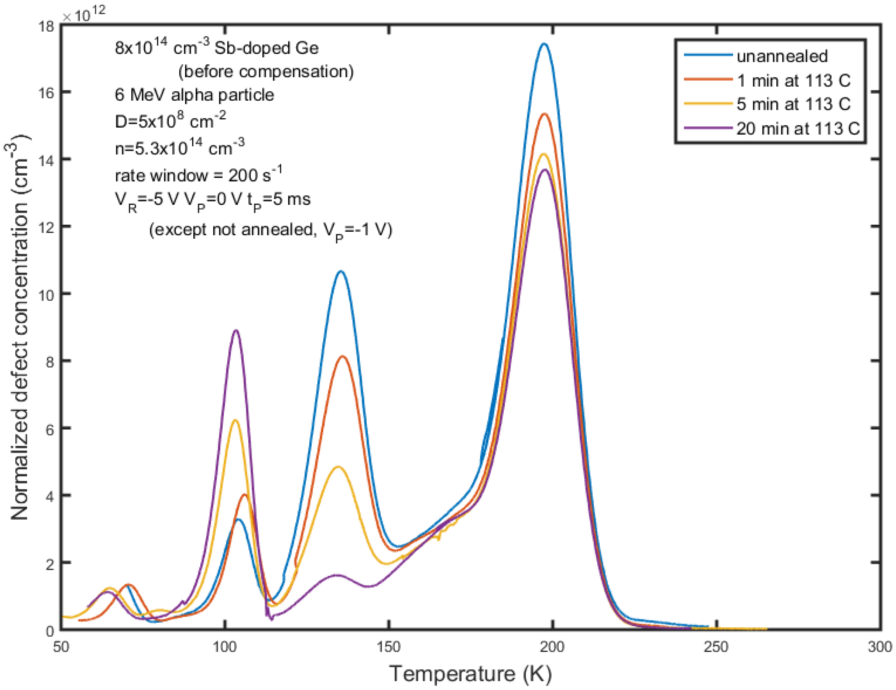

Figure 34: Isothermal annealing profiles at 113°C of $5\text{x}10^{8}$ cm^{-2} 6 MeV alpha particles irradiated germanium. The annealing of E_{22} drives the growth of E_{21} and the decay of E_{37}. The other defects are stable.

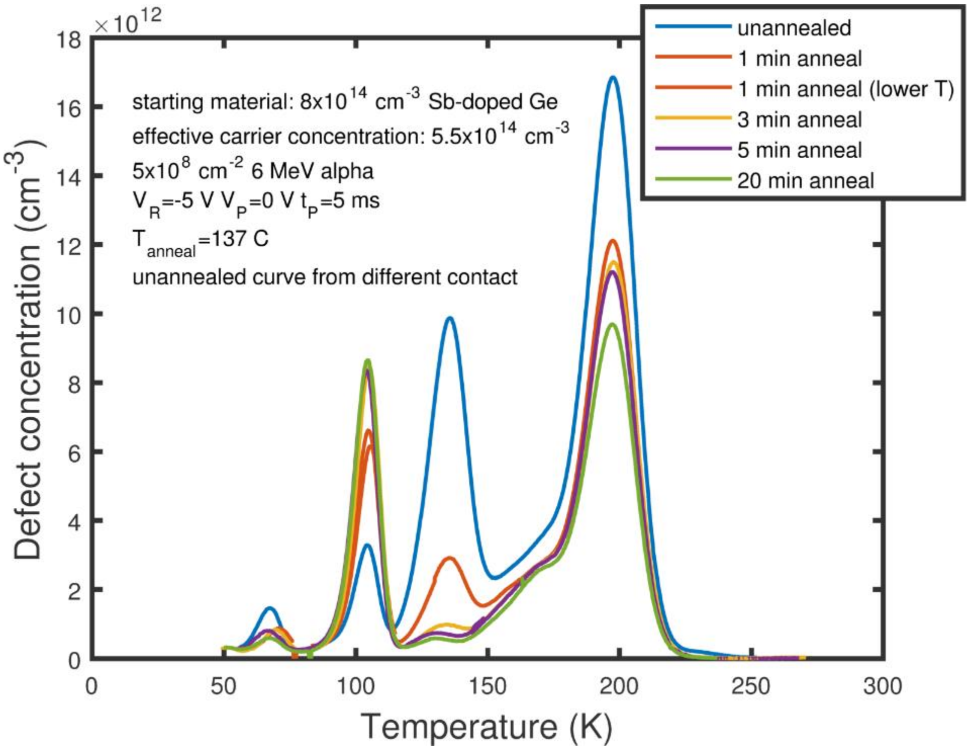

Figure 35: Isothermal annealing profiles at 137°C of $5\text{x}10^{8}$ cm^{-2} 6 MeV alpha particles irradiated germanium. The annealing of E_{22} drives the growth of E_{21} and the decay of E_{37}. The other defects are stable.

IV. Summary

We have investigated the properties of the defects introduced in n-type CZ-germanium after a 6 MeV alpha particle and a 1.1 MeV neutron irradiation. 7 defects have been identified that were not present after a gamma ray irradiation, their electronic signatures (capture cross-section and activation energy) have been measured, the dependence of their introduction rate on the dose and the nature of the irradiating particle have been described, as well as their annealing behavior. From this information, we have sorted primary defects (E'_{29}, E'_{24}, E'_{19} and E'_{11}) and secondary defects (E'_{27} and E'_{23}, which dominates defect profiles obtained after high dose alpha irradiation), while the nature of E'_{15} remains unknown, due to its smaller introduction rate.Of the primary defects, E'_{24} and E'_{11} have a logarithmic capture cross-section, a signature of the cluster nature of the defects generated by the light particle irradiation: the defects are not spread uniformly in the sample, but located within the collision cascades resulting from the nuclear collisions of the neutrons and alpha particles. E'_{11} is favored by neutron irradiation compared to the other defects, and we assign it to a triple interstitial complex. E'_{23} is the defect with the highest introduction rate after a high dose of alpha particles. Ultimately, in addition to the generation of more complex defects, the biggest difference between a gamma and a light particle irradiation is the spatial distribution of the defects: a gamma irradiation creates defects homogeneously, whereas a neutron/alpha irradiation creates cluster of point defects in the region where a collision cascade happens. This proximity of the point defects inside a cluster has consequences: the defect can co-anneal and the electric field induced by the capture of a charge by one trap changes the capture cross-section of neighboring defects.

Chapter 5. Point defects in germanium photodetector

I. Introduction

In a real-life device, the active area is not made out of Czochralski (CZ) bulk germanium. For cost reasons, in most cases, the germanium will be grown by epitaxy on a silicon wafer. It will then be heavily processed: coated by photoresists, metals and other semiconductors, etched, implanted by ions, annealed, etc. As a result of this complex processing history, the germanium of a device is never as pristine as CZ germanium. It contains chemical impurities that can in-diffuse during any step. The processing itself can introduce defects: oxidation generates interstitials, nitridation increases the vacancy content, a high temperature treatment can induce inter-diffusion at the germanium interface, implantation creates interstitial loops and other point defects at the end of range, etc. In addition to the point defects, the growth of germanium on silicon requires the creation of high densities of misfit dislocations, which interact with the point defect. As a result, the point defects present in a thin film are different than that of bulk material. In this section, we will study the native, processing and irradiation point defects present in a commercial photodetector made of germanium on silicon. We will especially investigate how the population of point defects evolves upon irradiation by ^{60}Co gamma rays and to what extent the performance of the devices are affected by increasing doses of radiation.

II. Description of the germanium photodetector

Processing injects impurities, vacancies and interstitials in a material. However, the difference between bulk germanium and a thin film of epitaxial germanium grown on a silicon wafer (Ge-on-Si) is not only a higher native point defect concentration. Because of the lattice mismatch of 4% between silicon and germanium, dislocations nucleate to release the elastic strain that would result from a pseudomorphic growth. The dislocations in a Ge-on-Si layer are of two kinds: misfit dislocations and threading dislocations. The former are located at and run parallel to the interface between the two mismatched materials. They are responsible for the strain release in the germanium layer. These misfit dislocations are not infinitely long. They need to either terminate on a free surface or loop on themselves. In a thin film geometry, the only free surface available is the surface of the film itself. This is why the misfit dislocation eventually branch off the silicon/germanium interface and become threading dislocations, connecting a misfit dislocation to the surface, by crossing the germanium layer, as shown in Figure 36. Consequently, a large number of threading dislocations are crossing the germanium layer in Ge-on-Si devices. This number can be reduced down to 10^7 cm^{-2} by cyclic annealing, in combination with the use of mesa structures.

The photodetectors that we have studied in this doctoral work are 0.95 mm diameter high speed Ge-on-Si pin diodes that *Analog Device Incorporated* has provided us, and whose structure is sketched in Figure 37. A cross-section TEM micrograph of the device is presented in Figure 38**.** The substrate is a highly p-doped SOI wafer, on which is grown 1.5 µm of undoped germanium, itself capped by highly doped n-type poly-silicon. The germanium is grown by the two-step method[50]: first a low temperature deposition, a few tens of nanometers thick, second a high temperature growth for the rest of the layer. The goal of the low temperature step is to prevent a Stransky-Krastanov growth: at a high temperature in which the germanium adatoms can diffuse on the silicon surface, germanium forms islands, instead of a uniform pseudomorphic layer. The misfit dislocations are all situated in this layer grown at low temperature. The objective of the high temperature growth, besides obtaining a higher deposition rate, is to get a better quality of material: because of the higher mobility of the adatoms, such material contains less point defects. In addition, because it is further away from the silicon interface, it is only crossed by threading dislocations, not misfit dislocations.

The threading dislocations present in the germanium are electrically active and result in a p-type material, even if the germanium layer itself is undoped. However, the free hole concentration within the material is not uniform through the sample. From the poly-silicon/germanium interface, the first 0.5 µm have a constant hole concentration of 10^{15} cm^{-3}. This number raises up to 10^{17} cm^{-3} at a depth of 1 µm, where it plateaus until the germanium/silicon interface. The 0 V and -10 V depletion widths at room temperature are respectively 0.55 µm and 1 µm. Using a CV measurement, we were able to precisely measure the free hole concentration as a function of the depth in the region where it is not constant, as shown in Figure 39. The cause of this non uniform concentration is unclear, but most likely due to the in-diffusion of dopants from either silicon layer during a high temperature processing step.

Another important experimental consideration when working with these germanium photodetector: the packaging is a source of noise and even failure. Figure 40 shows the mounted samples before and after irradiation: the ozone generated inside the gamma irradiator has oxidized the pins, making the devices untestable for doses above 150 Mrad. Moreover, in order to control for the diodes to diodes variability, we have done measurements on the same diodes multiple times for different doses of a gamma. The recurrent mounting/unmounting of the samples in the DLTS chamber is a source of scratches of the metallic parts of the packaging, which increases the noise on the capacitance transient measured by DLTS and hence decreases the sensitivity of the measurements.

The IV of the photodetector is unconventional, as shown in Figure 41**.** Even if the device characteristic is asymmetric, it is only correctly rectifying at low voltages. Past -4 V, the leakage current does increase drastically, instead of capping at a maximum value. In this high leakage regime, the reverse current is so high that it is not affected by the dose of ^{60}Co gamma rays that it has received and the point defects that the radiation has induced: the dislocations dominate the properties of the device. A change of leakage current due to irradiation damage is only detected for lower reverse bias voltages (Figure 42), in a regime where the junction rectifies exponentially and the leakage current is small. This is because the point defects introduced by the irradiation are generation-recombination centers, consistently with the Shockley-Read-Hall model.

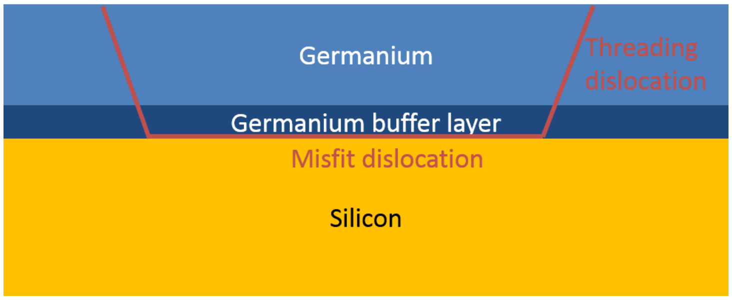

Figure 36: Schematic of the structure of a Ge-on-Si layer, with the position and type of dislocations.

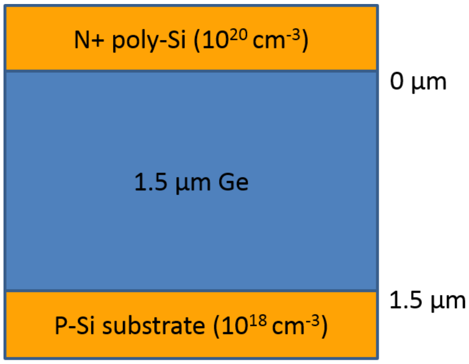

Figure 37: structure of the germanium photodetectors. The junction whose capacitance we will measure by DLTS is at the poly-SI and germanium interface.

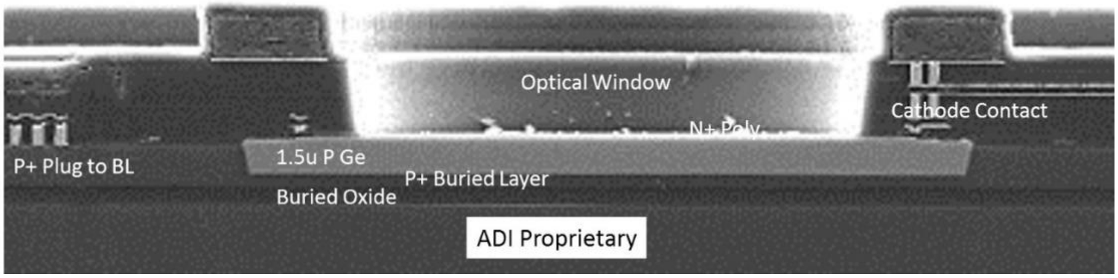

Figure 38: cross-sectional TEM micrograph of one of the photodetectors.

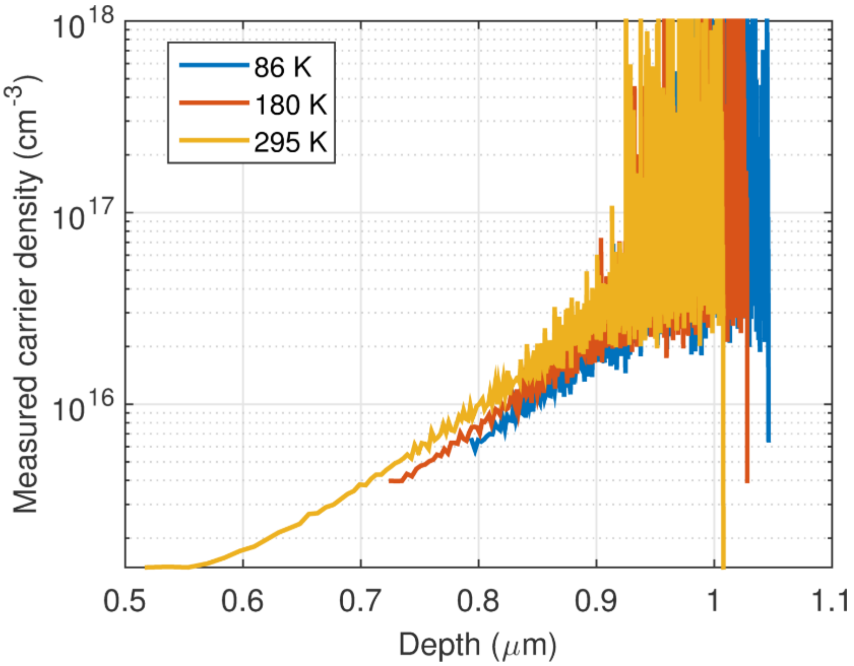

Figure 39: free hole concentration profile in the germanium layer, measured by CV at different temperatures. The doping of the sample is not uniform.

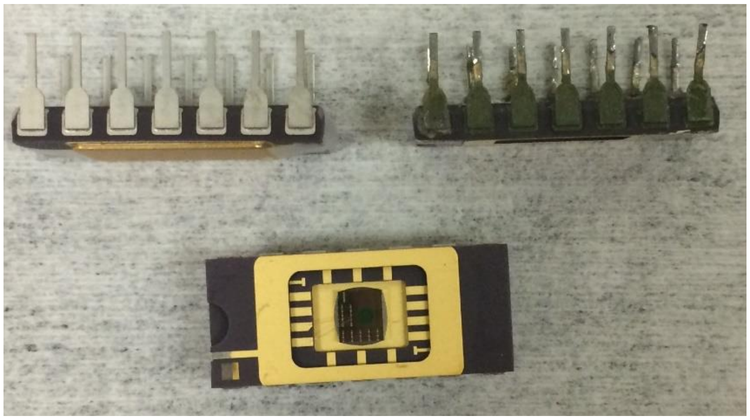

Figure 40: Pictures of the side of an unirradiated photodetector (top-left), of a 150 Mrad ^{60}Co gamma irradiated detector (top right) and top view of the packaging of an unirradiated photodetector (bottom). The oxidation of the pins due to the ozone in the irradiator is responsible for an decrease of the signal to noise in the DLTS measurements and ultimately the failure of the device.

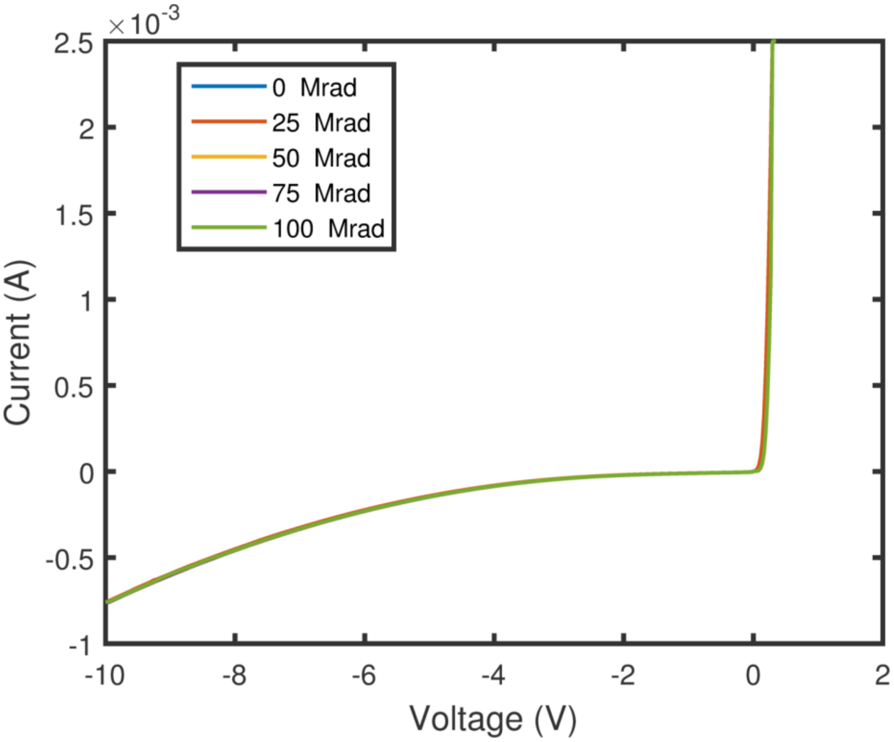

Figure 41: IV of one photodetector after receiving different doses of ^{60}Co gamma rays. The diode stops rectifying past a certain voltage and the leakage current increases drastically.

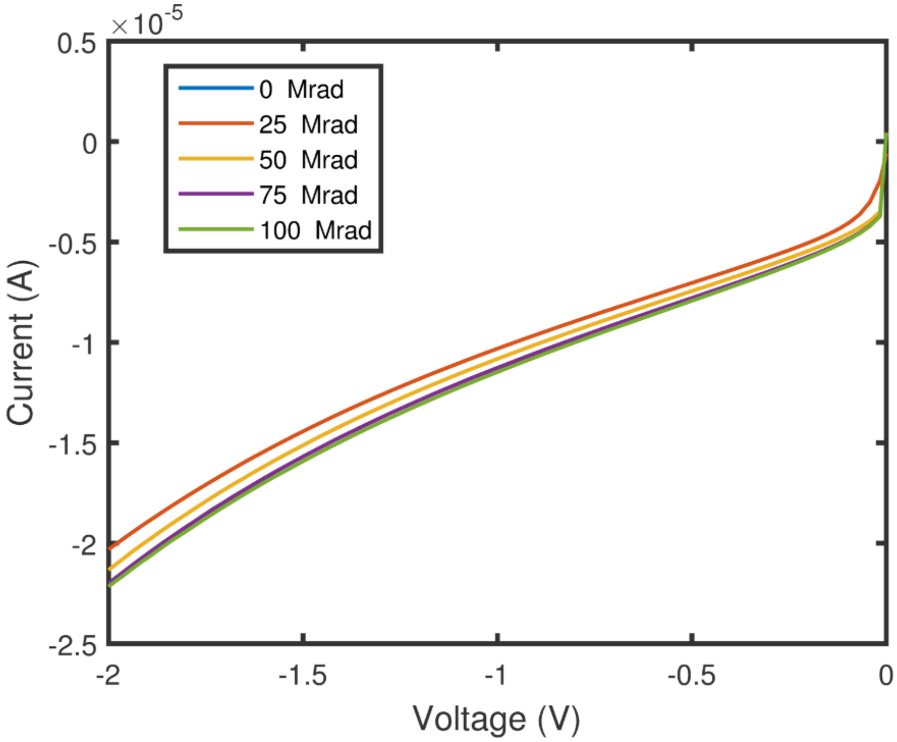

Figure 42: IV of one photodetector after receiving different doses of ^{60}Co gamma rays, centered in the low leakage current region where the diodes rectify exponentially. Radiation marginally increases the leakage current.

III. DLTS study

a) Point defect population

We have performed DLTS on photodetectors before and after irradiation by ^{60}Co gamma rays. In order to both stay in the regime where the leakage current is low and probe an area in which the free hole concentration is not too high, these measurements have been made at a small reverse voltage of -1 V. Another concern justifies this low voltage. Due to the non-uniform free hole profile, using a low reverse voltage means that the probed region is less deep and undergoes smaller variations of doping, which has two beneficial consequences: 1) the sensitivity of a DLTS measurement is a fraction of the free carrier concentration at the edge of the depletion region at bias and is thus increased; 2) by using a low voltage, there is no large variation of the doping level and less intense electric fields in the region which is examined. To avoid minority carrier injection, we have used a voltage pulse of -0.1 V. Because the germanium of the photodetectors is p-type, we have adapted the naming convention used so far in this doctoral dissertation to H_{XX}, to emphasize that the defects we are describing are hole traps. In this case, “XX” means that the level of the defect is 0.XX eV above the valence band.

We have studied multiple different photodetectors. There is some variability between the defect profiles that we measured, even in unirradiated samples, as shown in Figure 43. Some diodes do not contain defects whose concentration is above the sensitivity of our measurement, whereas other have background defects. We could not detect directly a state signature of a dislocation. There is only one native defects, H_{39a}. Echoing the variability of the initial defect population, the DLTS profiles after irradiation are also diverse, as shown in Figure 44. Different diodes irradiated by the same diode of 100 Mrad of ^{60}Co gamma rays, can have different profiles: the 150 K peak has different intensities, and the shape of the DLTS shape can change drastically in the 180 K to 210 K region. Furthermore, the defects are not all stable at room temperature. Figure 45 for instance presents the DLTS profile of the same diode after an irradiation and a month after the irradiation. This instability makes the study all the more difficult that the irradiation itself is slow: it takes over a day to irradiate a sample with 10 Mrad. The irradiation of high dose samples has a duration on the order of the decay constant of some defects.

Figure 46 presents the Arrhenius behavior of all the detected defects. The imprecision in the measurement of the emission rate for some of the defect (H_{41},H_{39a} and H_{39b} in particular) is unusually high. Multiple parameters can explain this problem: convolution of the different defects, high noise of the capacitance transient measurements and non-exponential emission rate[51], which can happen in defects associated with dislocations[52]. Such non-exponential rates can make the Laplace analysis difficult and noisier, because it is based on an algorithm designed to deconvolve perfectly exponential transients.

Despite the differences between individual photodetectors, the profiles have similarities: after irradiation, all the samples contain H_{17} (peaks at 100 K), H_{13}, H_{26} (highest introduction rate defect, peaks at 150 K) and H_{39b}. The bump at 190 K observed in diode 2 (Figure 44 and Figure 45) is due to the defect H_{40}, which anneals out at room temperature.

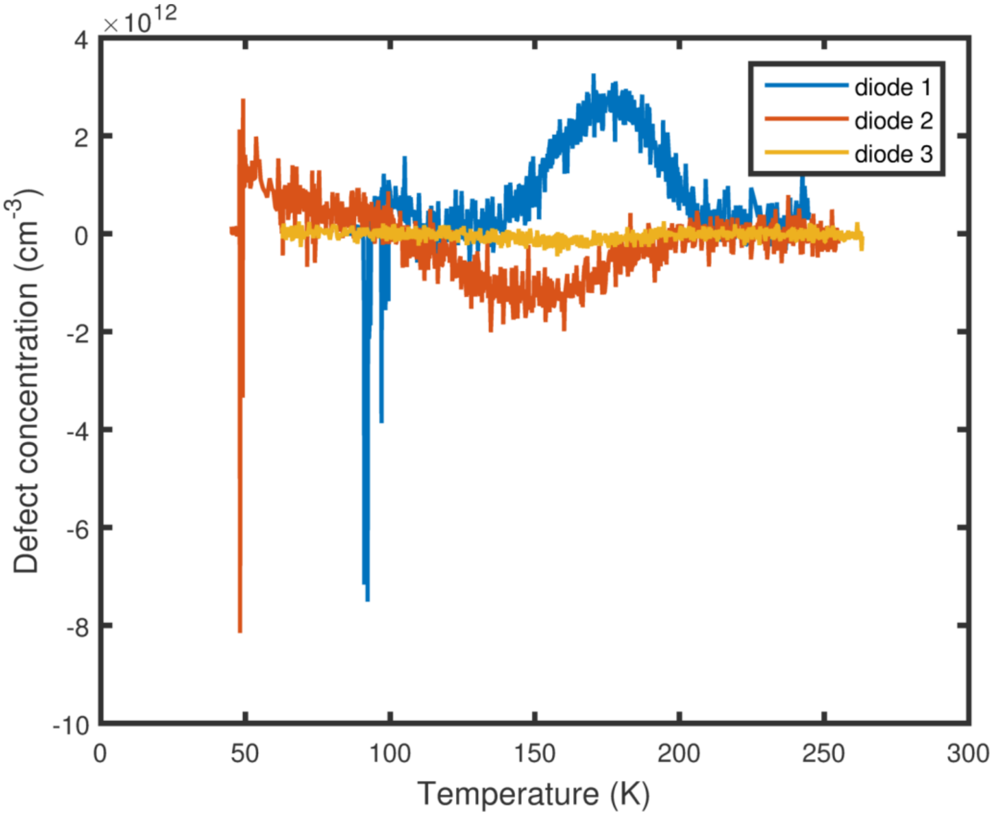

Figure 43: DLTS profile of unirradiated photodetectors. There is some variability between the diodes, and some contain point defects.

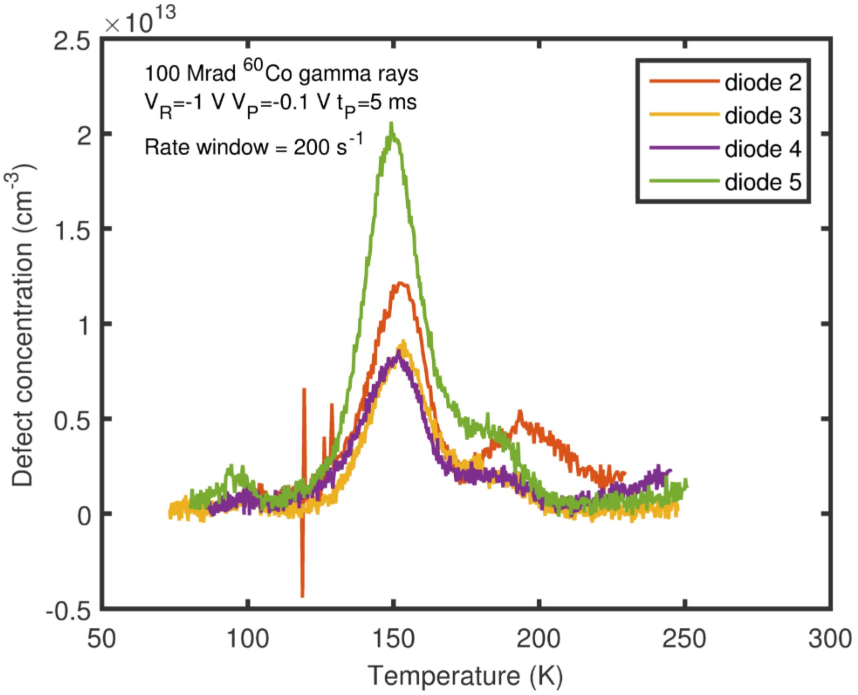

Figure 44: DLTS scans of diodes irradiated by 100 Mrad of ^{60}Co gamma rays, displaying the variation of defect profiles from device to device.

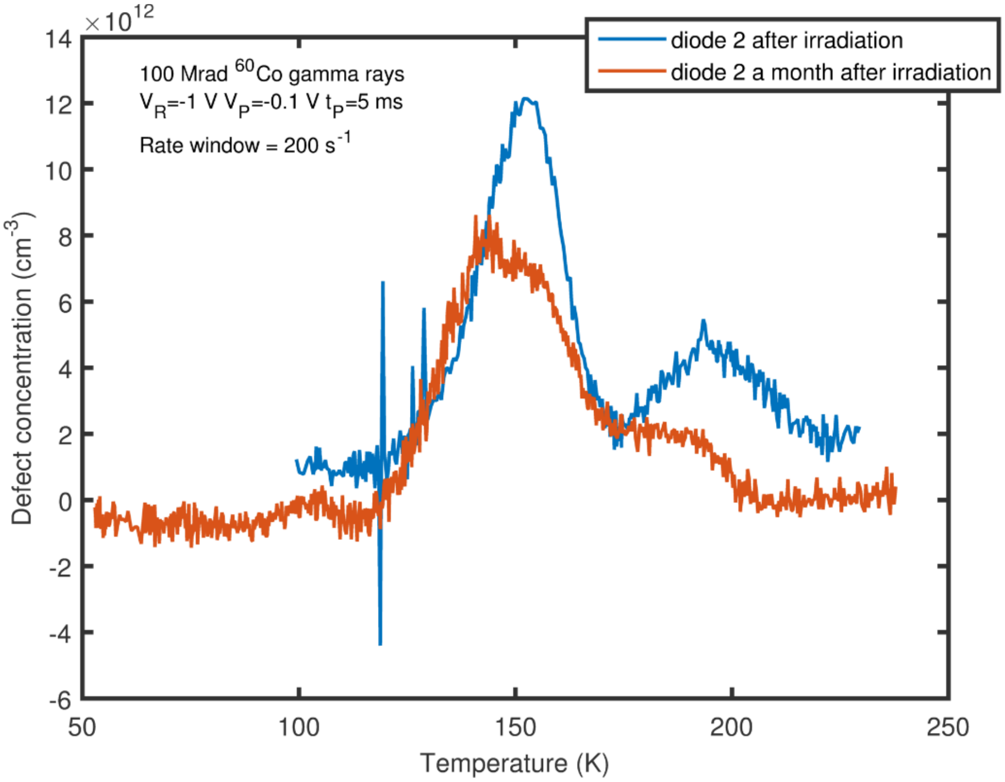

Figure 45: DLTS profile of the same photodetector after irradiation and after a month of aging at room temperature. Not all the defects are stable.

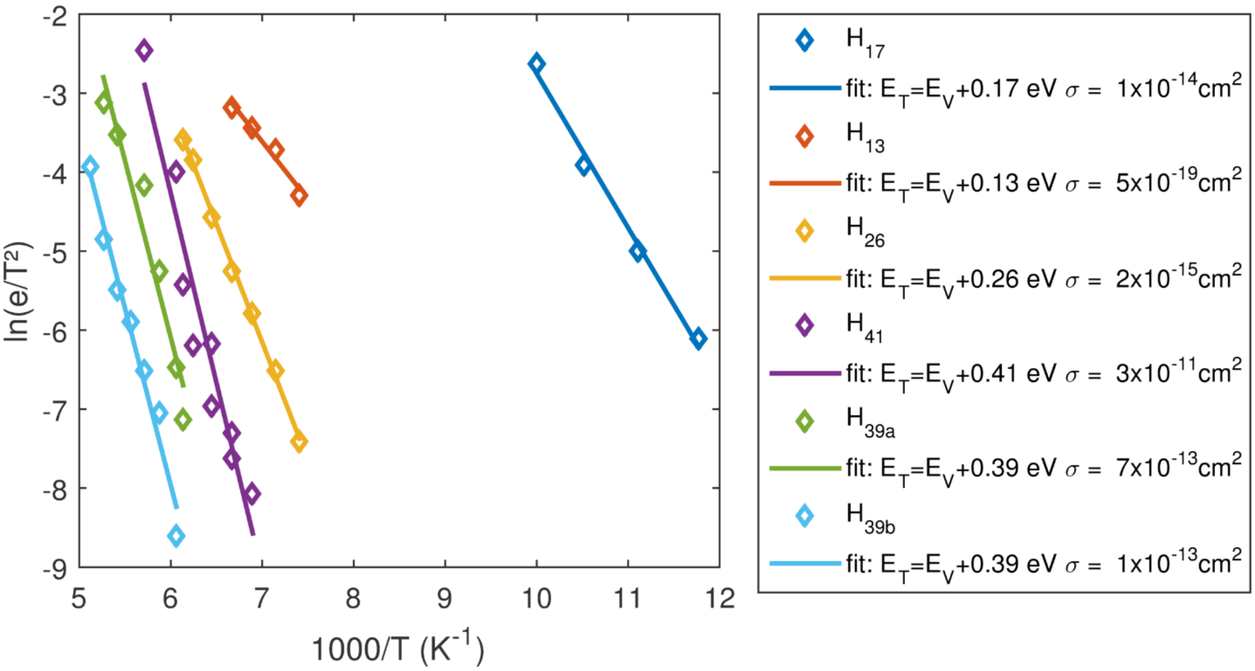

Figure 46: Arrhenius behavior of the different defects that we identified in the irradiated photodetectors.

b) Dose study in a background-less sample

In order to control for the variability between samples, we have performed a dose study of a photodetector that happened to not contain native defects prior to irradiation (diode 3 from Figure 43, which also had the smallest noise level before irradiation) and investigated the introduction rates of the different defects. The resulting DLTS profiles are presented in Figure 47. Only H_{26} has a linear introduction rate (Figure 48), of 1.1×10^{11} cm^{-3}.$Mrad^{-1}$. This introduction rate is of the same order of magnitude than that of the mono vacancy and self-interstitial in ^{60}Co gamma irradiated CZ germanium[16], rate that we calculated in a previous section of this doctoral work. This consistency of introduction rate between bulk CZ-germanium and epitaxially grown thin film germanium is expected, as the introduction rate is related to the irradiating particle, the atomic mass of germanium and the strength of the Ge-Ge bond, and is thus independent from the background impurity and dislocation profiles. The concentration of the other defects is barely above the sensitivity level even for the highest dose of radiation and the signal to noise ratio is too low for an accurate determination of their introduction rate. However, their concentration seems to saturate at a value around 2×10^{12} cm^{-3}. This suggests that these defects out diffuse of the probed zone, maybe because they form with a sink of concentration in the 10^{12} cm^{-3}.

Due to its higher introduction rate, H_{26} is the only defect that we could study quantitatively. The noise was too high for the other defects to measure their concentration reliably. Beside its linear introduction rate, another property of H_{26} is its non-constant capture cross-section. Similarly to the defect E'_{24} in the neutron irradiated n-type CZ-germanium, H_{26} has a logarithmic capture cross-section (Figure 49 and Figure 50**).** In the absence of collision cascade, this logarithmic capture process is the signature of a dislocation defect[49]. In addition, H_{26} displays an electric field dependent emission rate and activation energy. Figure 51 plots its emission rate at different temperature and for different reverse biases and therefore demonstrate the field effect on the emission of carriers by the trap, because the higher the reverse voltage, the stronger the field inside the depletion region. The activation energy of H_{26} can be extracted from this measurement. It is 0.3 eV, 0.27 eV, 0.25 eV and 0.22 eV for reverse biases of respectively 0.5 V, 1 V, 2 V and 3 V. This electric field assisted emission can be due to a Poole-Frenkel effect (which suggests that H_{26} is charged neutrally when filled with a hole) or another field effect. H_{39b} also presents an electric field enhanced emission rate, but its smaller concentration prevented a precise measure of the variation of activation energy as a function of the voltage.

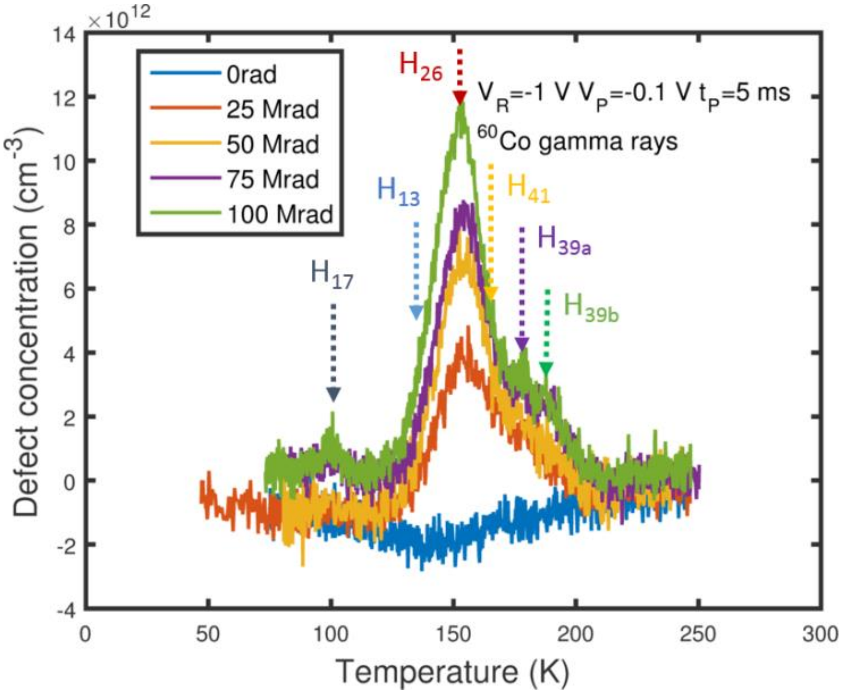

Figure 47: DLTS profiles as a function of increasing doses of ^{60} *Co gamma rays on the same diode. Multiple defects are convolved and the signal does not scale linearly with the dose, suggesting that most defects are not primarily generated.*

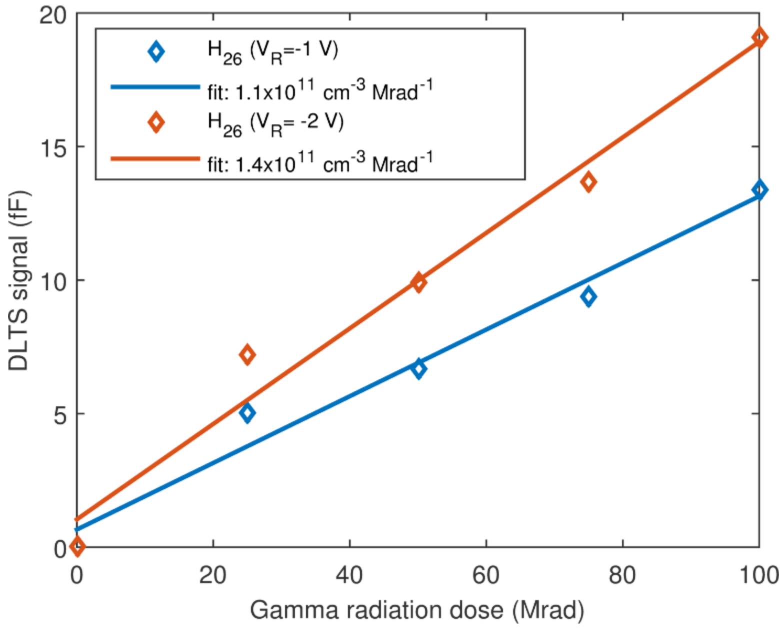

Figure 48: Introduction rate of H_{26}, as measured at two different reverse voltages (i.e. depth). The higher concentration measured at -2 V is due to the measurement imprecision induced by the non-uniform hole concentration inside the material.

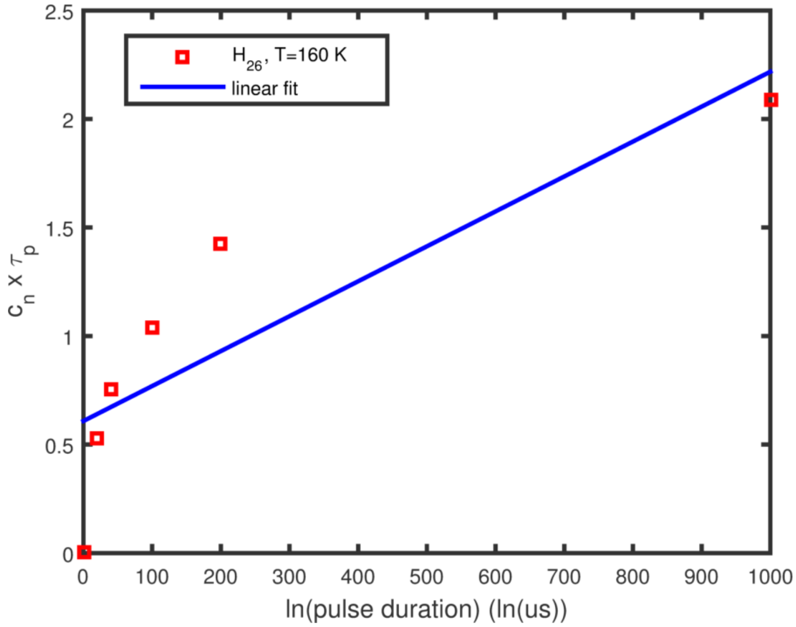

Figure 49: Application of a time-independent capture cross-section model to H_{26}. The non-linearity of the curve proves that this hypothesis does not apply.

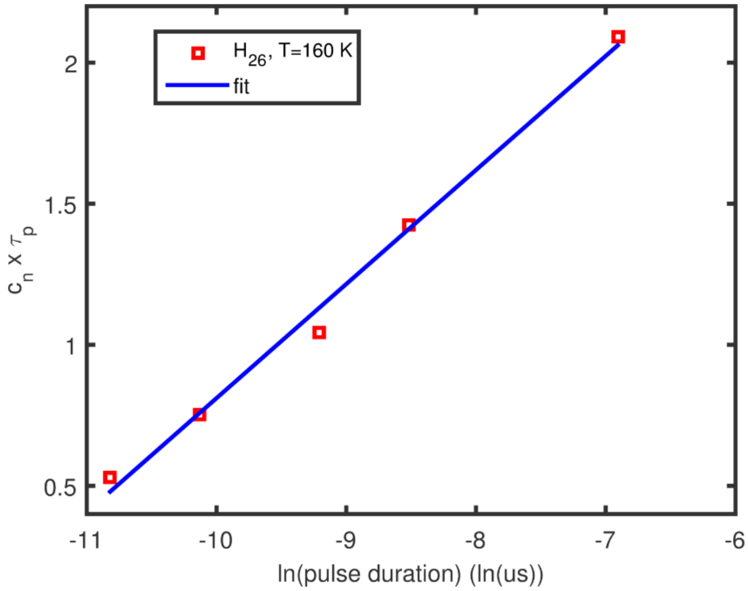

Figure 50: Demonstration that H_{26} has a logarithmic capture process.

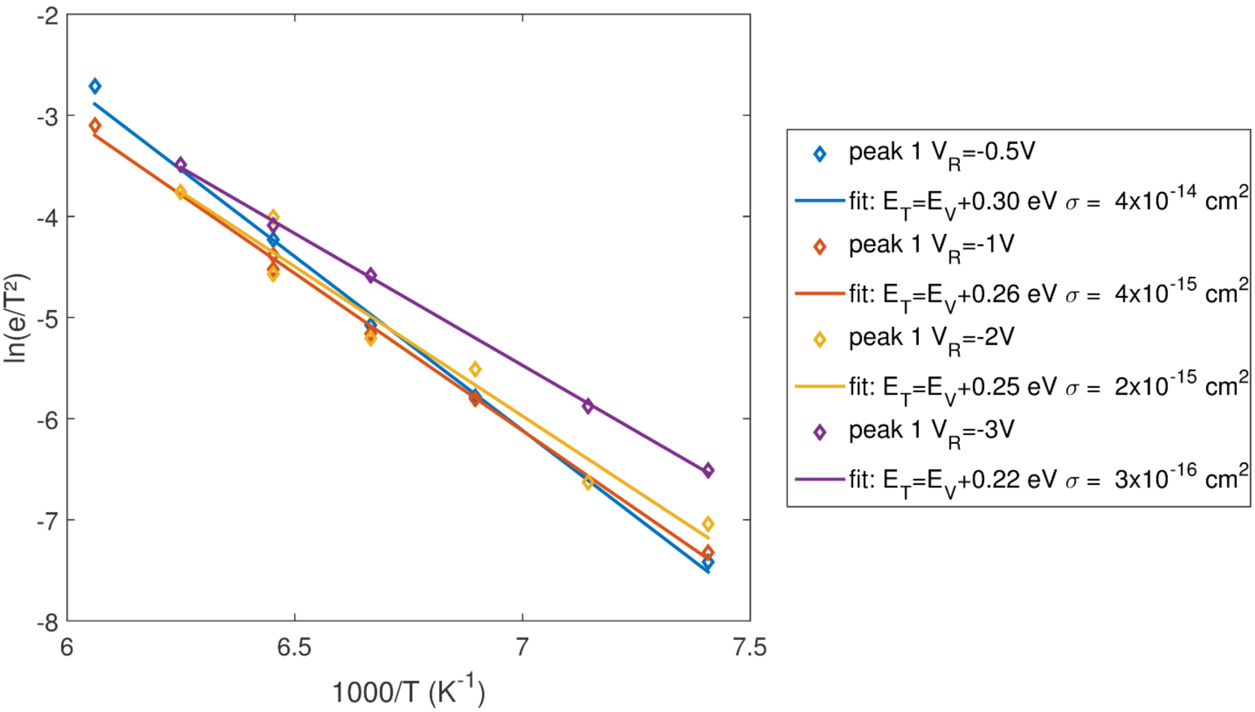

Figure 51: Arrhenius behavior of H_{26} at different reverse voltage, showing that the hole emission of this trap can be assisted by an electric field.

c) Forward pulsing

Contrary to the Schottky junctions that we studied in the previous chapters of this doctoral dissertation, these commercial photodetectors are pin-junctions. As a result, it is possible to inject minority carriers in the depletion region by forward pulsing the junction during a DLTS scan. This allows the characterization of the other side of the bandgap of our material. Experimentally, we kept the reverse voltage of -1 V, while using 5 µs pulses to 0.5 V. This yielded DLTS profiles such as Figure 52, which was obtained after a 100 Mrad irradiation of diode 5. Using Laplace DLTS, we were able to isolate 5 point defects. One of them is H_{26}, the four other are electron traps, whose Arrhenius behavior is shown in Figure 53. To reflect the fact that we measured them by pulse injection in a p-type sample, we have adapted the naming convention of these defects by adding an "i" in their name, but kept the fact that they are referenced by their activation energy. For instance $E_{i,23}$, has an apparent activation energy of ionization of E_C-0.23 eV.

The two main defects in term of concentration are $E_{i,23}$ and $E_{i,31}$, and are responsible for the general shape of the conventional DLTS scan shape (Figure 52). The concentration of the other defects is smaller and the measurement of their emission rate is therefore less precise. We have compared the Arrhenius behavior of these 4 electron peaks to those of the peaks resulting from the gamma irradiation of n-type CZ-germanium. Only $E_{i,34}$ and $E_{i,23}$ seemed to match defects that we previously observed, respectively E_{37} and E_{22} (Figure 54). The good match between $E_{i,34}$ and E_{37} suggests that the former could be a vacancy-donor complex. The Arrhenius graphs of $E_{i,23}$ and E_{22} are parallel and would overlap if the emission rates were shifted by 2 K. It is unclear whether this is a coincidence or a measurement error due to the thermal mass of the packaging of the photodetector.

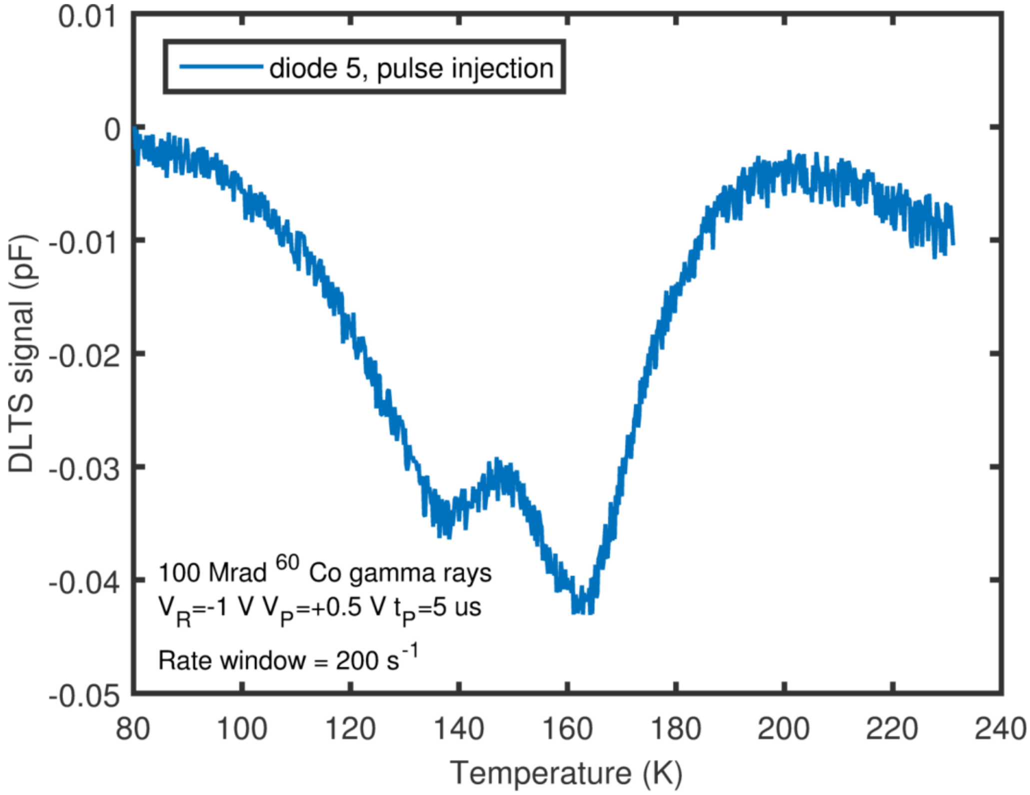

Figure 52: Forward bias pulse DLTS scan on a photodetector. The negative peaks correspond to minority carrier traps, electron in this case..

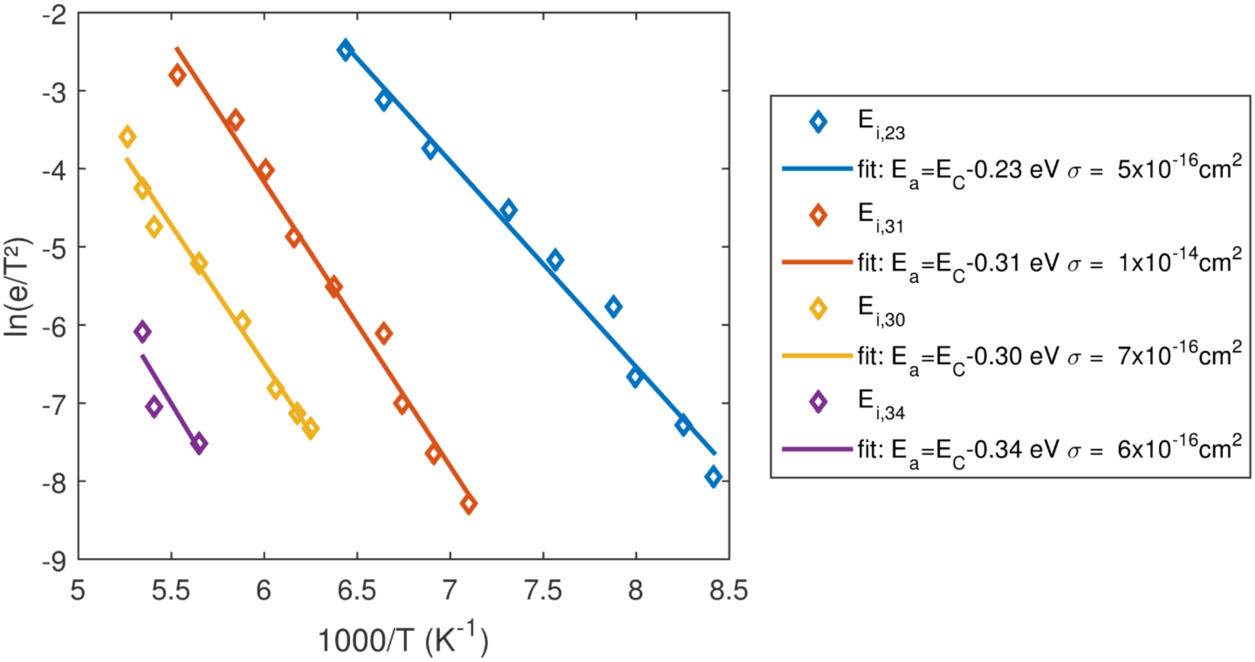

Figure 53: Arrhenius behavior of the traps observed after minority carrier injection DLTS.

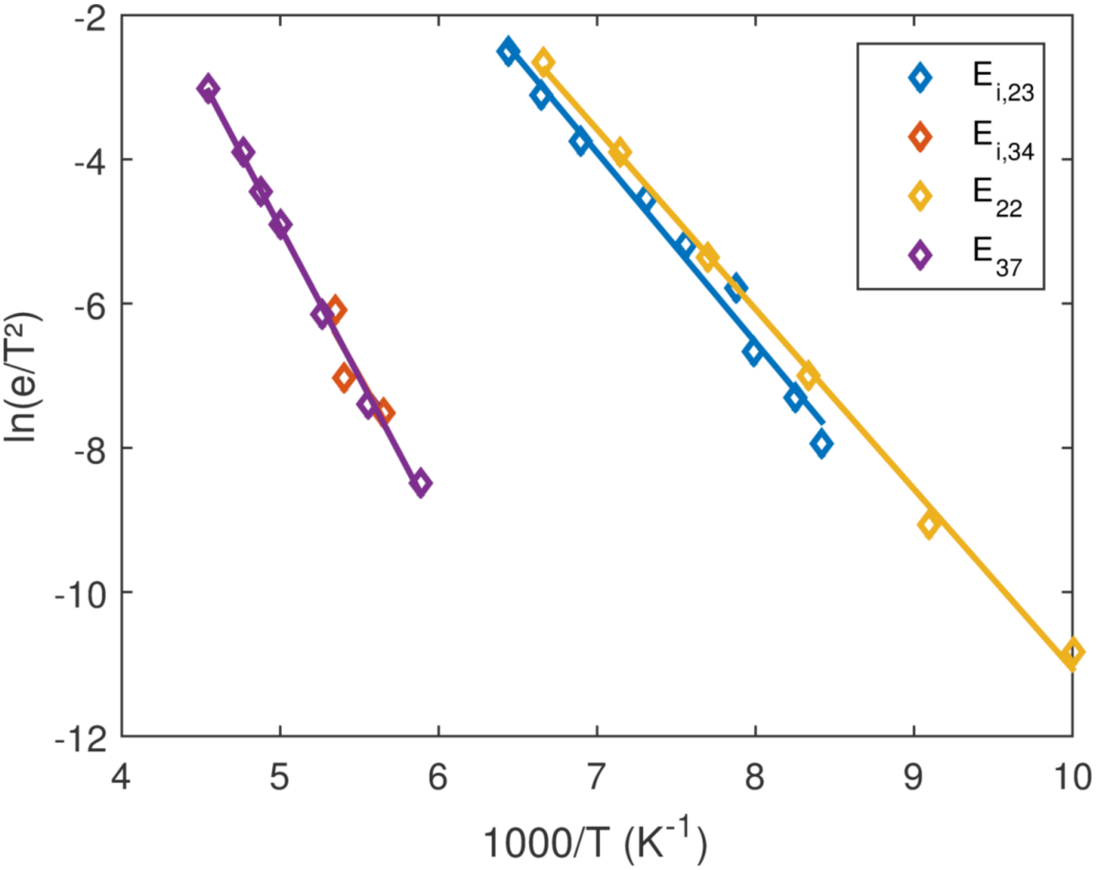

Figure 54: Comparison of the arrhenius behavior of $E_{i,23}$ and $E_{i,34}$ with these of E_{22} and E_{37}, two defects observed in ^{60}Co gamma irradiated Czochralski germanium. This similarity suggests that these defects are the same.

d) On H_{26}

Because of its higher introduction rate, H_{26} is the defect on which we have the most data, and whose measurement is the most precise. Its Arrhenius behavior and its electric field assisted emission makes H_{26} similar to the defect H_{30} observed by Fage-Pedersen et al. [43], Markevich et al.[53] and Lindberg et al.[54], as well as the E_V+0.24 observed by Fukuoka et al. [55]. Due to its concomitant annealing with the double acceptor state donor-vacancy complex (E_{37} in our previous experiments, also called the E-center) in n-type samples [53] and good agreement with DFT calculation[56], this level was attributed to the single acceptor state of the donor-vacancy complex. Furthermore, the presence in the sample of $E_{i,34}$, a defect whose electronic signature matches the double acceptor state of the E-center, adds up toward this identification. Even if the germanium was grown undoped and is p-type, it is not a major objection: it is possible that some donors of the capping 10^{20} cm^{-3} n-type poly-silicon layer have in-diffused. However, the logarithmic capture cross-section of H_{26} differs from has not been reported by other groups, and suggests a dislocation associated peak, not a pure point defect. Therefore, if H_{26} is the single acceptor state of the E-center, it would suggest that the donors diffuse from the poly-silicon to the germanium by following the dislocations.

IV. Summary

Thin film layers usually do not behave like their bulk counterparts. In this chapter, we have characterized the point defects in a p-type germanium photodetector and confirmed this empirical rule. The main difference in the case of a hetero-epitaxially grown germanium-on-silicon layer is the presence of threading dislocations, which are responsible for the high leakage current of the devices. The electronic properties of the photodetectors themselves are dominated by these dislocations, making the leakage current relatively insensitive to the irradiation defects, even for high dose of ^{60}Co gamma rays. Furthermore, the logarithmic capture cross-section and non-exponential emission rate of some traps is a sign that they are close to or inside a dislocation, which therefore directly affects the properties of the point defects. Another important feature of the photodetectors is the variability of their defect profiles. Contrary to bulk Czochralski germanium, the epitaxial germanium of the photodetectors contains some point defects prior to irradiation, either generated during the growth of the layer or during the processing steps, and there is some difference between samples in their defect background. Even if this variability persists to some extent after a ^{60}Co gamma ray irradiation, all the defect profiles are dominated by H_{26}. This defect has a logarithmic capture cross-section, an electric field assisted emission process and an introduction rate consistent with this of the Frenkel pair in bulk germanium. Its properties suggest it might correspond to the single acceptor level of a donor-vacancy complex in the vicinity of a dislocation.

Chapter 6. What happened to the *Chandra* telescope detectors?

I. Introduction

More than characterization, this doctoral work is about defect engineering. In this part, we will show how the knowledge of the point defect population in silicon can be leveraged to solve a real-life problem: the reverse annealing of the CCDs *Chandra* X-ray telescope. After its launch in July 1999, silicon CCDs of this spatial telescope were damaged by irradiation, causing an increase of leakage current and of charge transfer inefficiency (CTI). To remove this damage, the CCDs were annealed to +30 °C for a few hours (the operating temperature being -100 °C), which resulted in a further 35% increase of the CTI. This degradation of performance following an anneal was referred to as "reverse annealing" in previous articles[57], [58]. Now, more than 17 years later, another annealing of the device is required to remove residues on the telescope imaging array. Over the course of its lifetime the CCD has been exposed to even more radiation and hence has accumulated new defects which could result in another increase of the CTI if annealed inappropriately. The question we will be solving in the chapter is thus the following: what caused this phenomenon, and can we prevent it to happen again?

II. Review of the proposed mechanism

The X-ray spectrometer used in the Chandra telescope uses buried channel silicon CCDs of two kinds: front illuminated and back illuminated, of which only the former were significantly damaged by exposure to radiation. The different parameters of the CCDs are described in details elsewhere [59] and can be summarized as follows. The devices are fabricated on 100-mm p-type float zone silicon wafers of resistivity of 7000 Ω.cm. Therefore the background electrically active impurity concentration is deduced to be lower than $3x10^{12}$ cm^{-3}. This results in a depletion width of 50-70 µm. In addition to eventual electrically active impurities, high purity float-zone silicon contains carbon and oxygen at a 10^{15-16} cm^{-3} level. The buried channel is obtained by an implantation of phosphorus through an oxide layer with an energy of 200 keV. After the various other processing steps and related annealings are performed, the phosphorus profile is a few hundreds of nanometers deep. In addition, the pixels have a trough, a 2 µm wide past the buried channel potential well used to make the device more radiation hard [60]–[62]. The concentration of phosphorus in the buried channel and in the trough, where charges are collected and transfer after a light absorption event, is in the 10^{16} cm^{-3}. Therefore, in our analysis, we consider defects comprising vacancies, interstitials and their associates with carbon, oxygen and phosphorus.

Previous articles [57], [58], [63] have suggested that only low energy protons were involved in the degradation of CCD performance, based on the penetration depth of the radiation which scales with particle energy. SRIM[36] was used to determine the ion range, straggle and primary defects (vacancies and interstitials, for both ionic and nuclear stopping regimes) generated in silicon by irradiation of protons of different energies, as shown in Table 6. 100 keV protons have an implantation depth of 860 nm in silicon, which matches the position of the active area of the CCDs, while protons of energies higher than 1 MeV will create most of their damage farther inside the bulk of the wafer and should therefore not alter the device performance significantly. Protons of energies higher than 10 MeV can damage the front- and back-illuminated CCDs equally, but the latter were shown not to be affected by the reverse annealing. In addition, the frame store section, which is shielded by 2.54 mm of gold coated aluminum, was not damaged. This is consistent with low energy proton damage, which cannot penetrate the thick metal shielding. All these considerations confirm that low energy protons are the most likely to have introduced defects that were involved in reverse annealing. This was confirmed by 100 keV proton irradiation experiments performed on the ground with similar CCD devices [58] which yielded dark current and CTI changes similar to observations on the annealed Chandra CCDs.

Table 6: Ion range, straggle and primary defects (vacancies and interstitials, for both ionic and nuclear stopping regimes) generated in silicon by irradiation of protons of different energies (calculated by SRIM).

Proton energy	Ion range (um)	Straggle (nm)	Number of primary defects generated in ionic stopping regime (cm^{-3}/(ion.cm^{-2}))	Number of primary defects generated in nuclear stopping regime (cm^{-3}/(ion.cm^{-2}))
100 keV	0.86	82	$4x10^4$	$1.5x10^5$
1 MeV	16.6	514	$4x10^3$	$5x10^4$
10 MeV	714	$14x10^3$	$3x10^2$	$5x10^3$

Irradiation damage creates Frenkel pairs, each pair consisting of one interstitial and one vacancy. The pair can split, leaving behind mono-vacancies and self-interstitials. Figure 55 is a schematic of the transformation as a function of the temperature, of the various defects observed in float-zone phosphorus-implanted silicon.

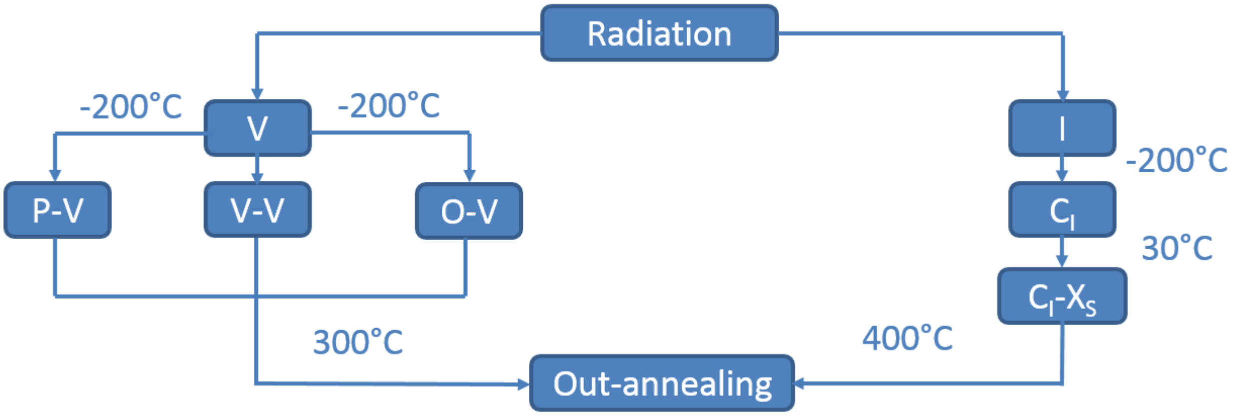

Figure 55: Schematic of the point defect changes in n-type float zone silicon as a function of the temperature. The mono-vacancies and the self-interstitials form complexes with impurities at -200°C. Then the vacancy associates are stable up to 300°C, while the carbon interstitials will pair with a substitutional impurity at 30°C until it out-anneals at 400°C[15].

The mobility of defects at temperatures of interest can explain annealing-induced increase in CTI. At -100 °C, the operational temperature of the Chandra telescope, the mono-vacancies and self-interstitials created are mobile and will diffuse in the material until they form more energetically favorable complexes with impurities, such as oxygen, phosphorus and carbon. The resulting vacancy complexes (O-V, P-V and V-V) are present at -100°C and stable up to 300°C, therefore not affected by the annealing at +30°C. The concentration of vacancy defects should therefore remain unaffected by the annealing. They contribute equally to the CTI before and after annealing and are not responsible for the performance degradation, as explained later in this article and shown in Figure 56. In contrast, the carbon interstitial (C_I, the defect that forms from the association of the self-interstitial and a carbon atom) has a high mobility at the anneal temperature of +30°C. For comparison, the ratio of diffusivity of the donor-vacancy pair and the carbon interstitial at +30°C is $\frac{D_{P-V}}{D_{C_I}} = \frac{9.7x10^{-4}\exp(-\frac{0.93}{kT})}{0.44\exp(-\frac{0.87}{kT})} = 2x10^{-4}$ [64], [65]. In addition, vacancy complexes do not react with other impurities as much as the carbon interstitial, which, once mobile, will diffuse until it forms the more stable C_I-X_S complexes (with X_S a substitutional impurity, which in the case of the Chandra CCDs, is either phosphorus, oxygen or carbon) [66], [67]. When the carbon interstitial diffuses, the probability that it forms a complex with an impurity X_S is proportional to the product of the X_S concentration and the reaction capture cross-section. In the buried layer, the active area, the highest concentration impurity is phosphorus (peak concentration of 3x10^{16} cm^{-3} whereas an upper bound for carbon and oxygen is 5x10^{15} cm^{-3}). Moreover, the capture cross-section of the formation of a phosphorus complex is two to twelve times higher than for an oxygen or carbon complex [67]. Therefore, the carbon interstitial will most likely form complexes with phosphorus.

We can conclude that the carbon interstitial (C_I) travels relatively rapidly at the annealing temperature to associate with a substitutional atom (X_S), forming a (C_I-X_S) complex. These C_I-X_S complexes introduce states in the bandgap which are closer to midgap than the C_I (Figure 56, to be discussed), which implies (i) a higher capture-cross section of majority carriers (it is more likely that the charges are captured during one clock cycle) (ii) a smaller emission rate (it is less likely that an absorbed charge is re-emitted during a clock cycle) and (iii) a higher cross-section of minority carriers (the traps are more efficient recombination centers). In the case of the Chandra CCDs, the increase in CTI can be explained by the relative position of the defect states in the bandgap with respect to the Fermi energy, as is summarized in Figure 56. We can calculate the quasi-Fermi level in the detector by approximating the number of injected carriers due to X-ray excitation. A typical charge packet in the on-board CCD contains 100 to 2500 electrons. In the following calculation, we will use the number of electrons in a packet generated by the X-ray calibration source of the telescope at -100°C: 1600 electrons. This will determine the carrier concentration inside the device and hence the Fermi level position and the behavior of the different traps present in the device. To estimate the charge profile distribution, we have used profiles simulated in CCDs with a similar architecture[68]. The devices in the said simulation do not have a trough, but this is the only main difference with the *Chandra* CCDs. The presence of a trough is equivalent to having the width of a pixel shrunk to the size of the trough. The simulated profiles are done in a 27 µm x 27 µm pixel, and the Chandra trough are 2 µm. This means that a shrinking ratio of 13.5 is a good approximation: a 1600 electrons charge packet is equivalent to a 22 000 electrons packet in the simulated CCDs, which corresponds to a carrier concentration of 3x10^{15} cm^{-3} and a quasi-Fermi level 0.13 eV below the conduction band at -100°C. Therefore, the defect state of the carbon interstitial (E_C-0.1 eV) is above the quasi-Fermi level and its occupation (Fermi factor) is f=8%. It follows that its emission rate is much higher than its capture rate (Equation 16, in which n, v, σ, N_C, E_F, E_T, E_C respectively denote the free carrier concentration, the thermal speed of the carrier, the capture cross-section of the defect, density of states of the conduction band, the (quasi)-Fermi energy, the deep-state level and the level of the conduction band) which means that most of the traps are empty and do not contribute to any loss of charges during the column to column transfer. This is the opposite of the C_I-X_S, which have deeper states than the quasi-Fermi level (for instance C_I-P_S has multiple metastable states, respectively 0.23, 0.26, 0.32 and 0.38 eV below the conduction band [69]). Even for the shallowest of the C_i-P_S for instance, the Fermi factor at -100°C for a 1620 electron pulse is 0.998, an order of magnitude higher than for the donor level of the carbon interstitial. Consequently, even if the number of traps is the same before and after the reverse annealing, the effective number of traps contributing to the capture of electrons is much higher after the reverse annealing.

$$\frac{c_n}{e_n} = \frac{n v \sigma}{N_C v \sigma \exp\left(-\frac{E_C - E_T}{kT}\right)} = \exp\left(\frac{E_F - E_T}{kT}\right) \qquad \text{(Equation 16)}$$

The vacancy-defects (P-V, O-V and V-V, which were detected in the *Chandra* CCDs using a variation of DLTS[63]) do affect the CTI and the leakage current of the device which is why the performance of the CCDs degraded after launch even before the annealing. However, they do not impact it in the same proportion despite being introduced in the same concentrations as interstitial defects (each radiation event creates one interstitial and one vacancy). This is due to their position in the bandgap and their formation process. The dominant defect peak in n-type phosphorus-doped float zone silicon, which constitutes the buried layer, is the phosphorus-vacancy pair [70], which is deep in the bandgap (E_C-0.44 eV). Consequently, its emission rate is small: its characteristic time for emission is more than a second. As a result, during radiation exposure, the P-V states are quickly filled with electrons, do not re-emit charges and thus do not capture new charges during their transfer from one column to the other. On the other hand, the oxygen-vacancy (O-V) has a defect state of 0.18 eV below the conduction band and contributes to some charge transfer inefficiency. But in float zone n-type silicon, the formation of the oxygen-vacancy (O-V) defect is less likely than the phosphorus-vacancy (P-V) defect [70]. The case of the di-vacancy is similar to the O-V. It does not affect the CTI is because its concentration is too small (even if its position below the Fermi energy yields a high occupation). Indeed di-vacancies in silicon form as primary defects, when a collision event transmits enough energy to form two Frenkel pairs at the same location, the likelihood of such a double-Frenkel pair formation is smaller than that of a single pair creation. In the case of 10 MeV electrons for instance, there is an order of magnitude more single than multiple displacements. Therefore, there are di-vacancies in the material, as shown by Prigozhin et al. [63], but their concentration is small. Most of the vacancy-defects in the buried channel are therefore the inactive P-V centers, hence why interstitial defects mostly contribute to the CTI.

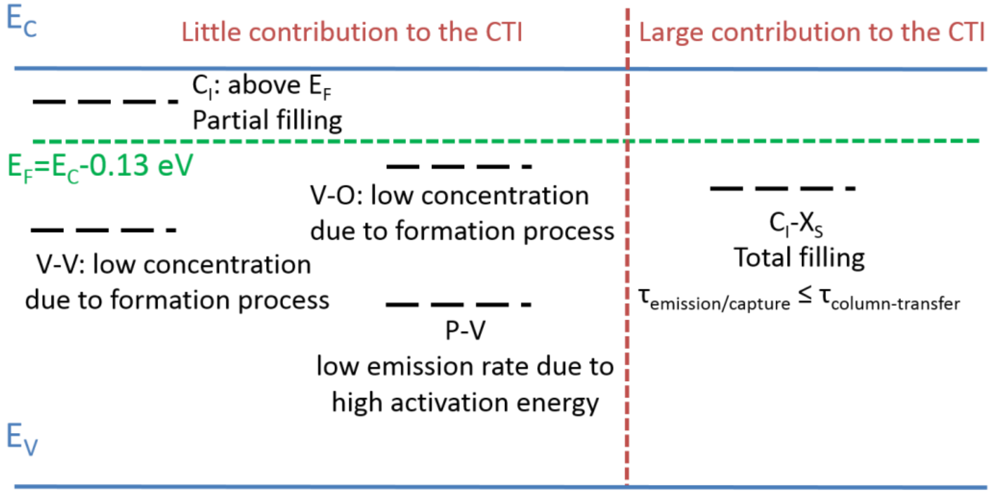

Figure 56: Various defects present in the active region of the Chandra CCDs. The defects on the left do not contribute to the CTI either because their states are above the Fermi energy and are only partially filled with charges, their chemical concentration is too small, or their emission rate is much slower than the transfer rate from column to column and once filled, they do not interact with new charges anymore. On the right is the C_I-X_S *complex which is the only contributor to the CTI after the reverse annealing.*

Only the C_I-X_S complexes are responsible for the reverse annealing and their formation is diffusion limited. A crucial assumption of this model is the existence of a high concentration of sinks for the carbon interstitials. This assumption is validated by the on-ground CCD irradiation study reported by Grant et al.[58]. In these experiments, a soft proton implantation could replicate the increase of CTI with doses of 10^8 protons cm^{-2} [58], which is equivalent to an introduction of 10^{13} cm^{-3} interstitials, as obtained from the Stopping and Range of Ions in Matter (SRIM) software (Table 6). Therefore, the carbon-interstitial concentration C_I ($\approx 10^{13}$ cm^{-3}) is indeed dilute compared to the concentration (10^{15-16} cm^{-3}) of the substitutional C or P impurities, confirming that post-anneal CTI saturates due to the consumption of all the carbon interstitials and not due to the consumption of the substitutional impurities. Consequentially, it also means that there are still plenty of sinks available in the CCD material to react with any new interstitials introduced over the last 15 years, leading to the conclusion that the previously observed reverse annealing is likely to occur again.

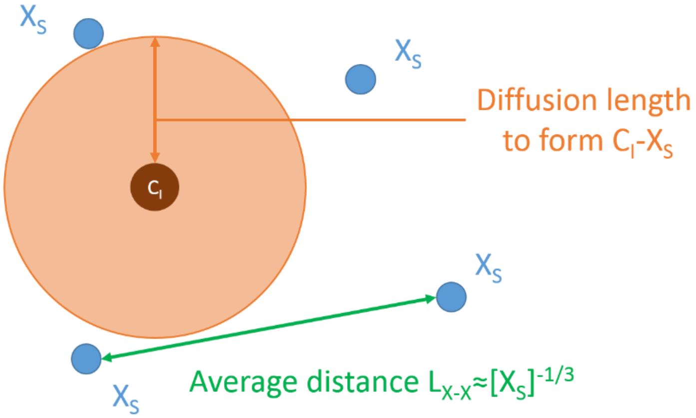

Figure 57: Schematic of the average distance between impurities and the diffusion length of C_I*. The formation* C_I*-*X_S *happens when the diffusion length is of the same order of magnitude as that of the average distance between* X_S*'.*

The formation of the general C_I-X_S complex is limited by the diffusion of the carbon interstitial, whose diffusivity is $D_{C_I} = 0.44 \exp\left(-\frac{0.87eV}{kT}\right) cm^2 s^{-1}$ [64]. For a diffusion-limited reaction in the limit where the concentration of C_I is small compared to the concentration of X_S, the formation of a C_I-X_S complex occurs when the diffusion length (given by Equation 17) is of the same order of magnitude as that of the average distance between X_S atoms: $L_D \approx [X_S]^{-\frac{1}{3}}$ (Figure 57).

$$L_D = \sqrt{D_{C_I} \tau_{annealing}} \qquad \text{(Equation 17)}$$

Figure 58 represents the distance travelled by diffusion of C_I as a function of annealing temperature for different annealing durations, as well as the typical distance between background impurities and the inter-atomic distance in a silicon crystal. This figure can be used to determine an upper limit for the annealing duration and temperature to prevent the diffusion to a sink of a certain concentration. It is consistent with the reverse annealing observed in the past, during which the CTI increased during a few hours at +30°C before saturating. Indeed, for such an anneal, the diffusion length of the carbon interstitial corresponds to the distance between background impurities. As the diffusion distance gets closer to the lattice parameter, this continuous model breaks down. The diffusion indeed becomes a discreet random walk, where the carbon-interstitial has a certain probability to hop from one site to another neighboring site. When the diffusion length of the continuous model falls below the inter-atomic distance, it means that the probability of even one jump of the C_I is low and that diffusion is effectively frozen. In order to prevent a further increase of CTI, the annealing parameters should hence be chosen to be in this "no-diffusion" regime. Figure 59 shows the onset of this regime as a function of annealing temperature. It defines the upper bound of annealing parameters to avoid the reverse annealing: below the blue curve, the C_I is not mobile, which corresponds to annealing durations shorter than a month at -65°C, a week at -60 °C or a day at -50°C.

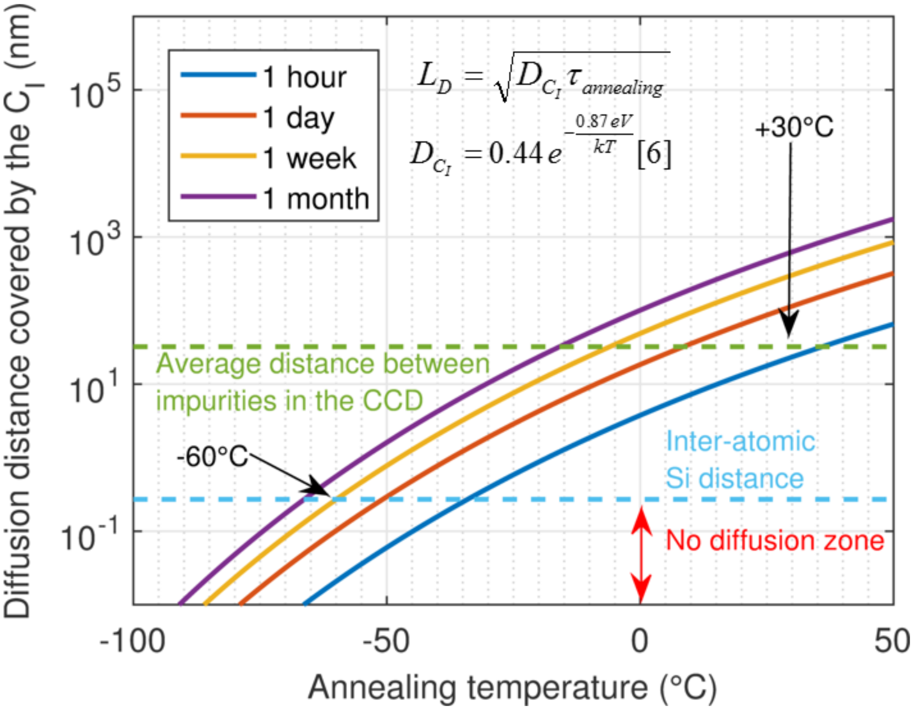

Figure 58: Diffusion length of the carbon interstitial as a function of the annealing temperature, for various annealing durations. The average distance between impurities in the CCDs (calculated to correspond to a concentration of 3×10^{16} cm^{-3}, the maximal concentration of phosphorus in the buried channel. It is also an upper bound for the background concentration of carbon and oxygen) and the inter-atomic distance of silicon atoms are indicated.

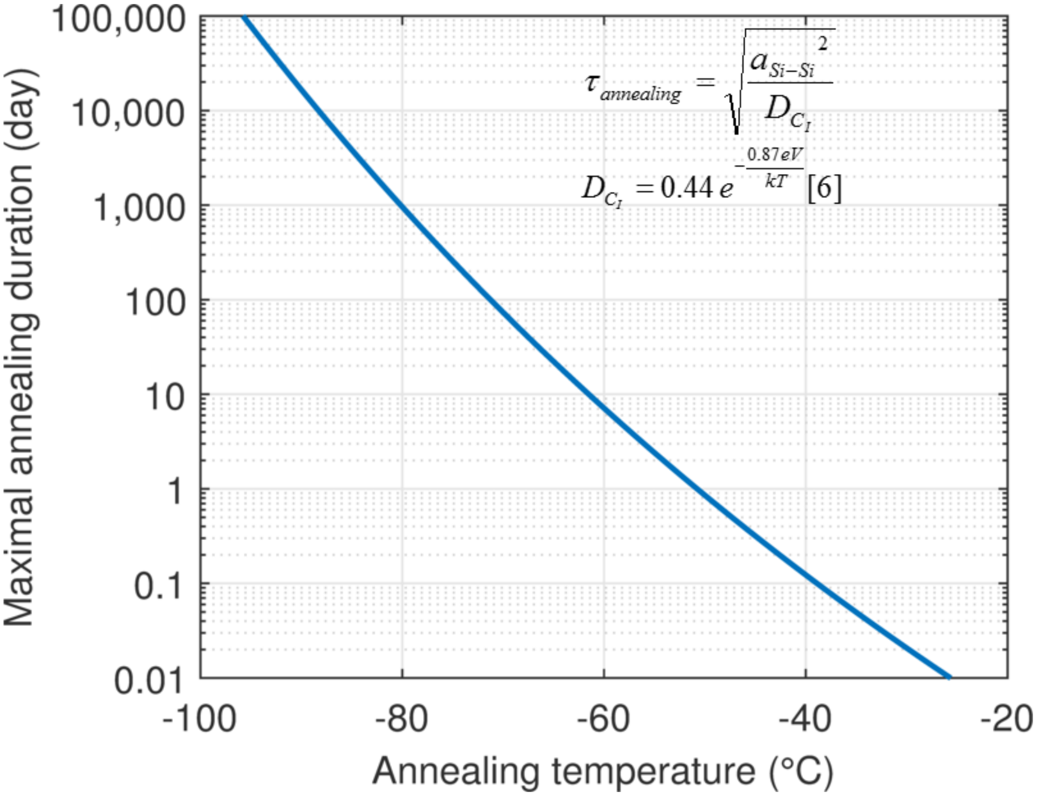

Figure 59: Maximal annealing duration versus annealing temperature to avoid diffusion of the C_I *and the formation of* C_I-X_S.

III. Comparison to similar work in other satellites in orbit

In addition to the work on the Chandra telescope, data on the degradation of CCDs of other telescopes (Hubble[71] [72]–[74], XMM Newton [75], ASCA [76]) show reverse annealing effects of the cells, but to a smaller extent than that observed in Chandra. Studies in the literature focused on the impact of high energy protons and vacancy defects, which are not the defects responsible for the CTI increase of the Chandra CCDs. Also, the X-ray telescope trajectory is different from that of the others making estimation by comparison difficult. For instance, the Hubble telescope is at an altitude of only 569 km (compared to the 14,000 km perigee and 135,000 km apogee of Chandra) and does not cross the Van Allen belt, which is the largest source of ionizing particles around the Earth. More importantly, the amount of shielding that protects the CCDs as well as the angle at which the incident particles strike are unknown. We can therefore not directly apply the conclusions of the articles describing the damage received in orbit by other satellites to the Chandra telescope.

IV. Summary:

Leveraging the existing knowledge on the point defects present in silicon, we could identify that the transformation of carbon interstitials into complexes made by the association of an impurity with a carbon interstitial is the mechanism causing the degradation of Charge Transfer Inefficiency which followed the annealing of the CCDs of the *Chandra* telescope. This reaction is diffusion limited. Therefore, in order to prevent further increase of the CTI, the formation the C_I-X_S can be prevented by annealing below temperatures at which the C_I is “frozen” on site, and does not diffuse. We showed that this can be done by not exceeding the following conditions: (i) a week long anneal at -60°C or (ii) a one day anneal at -50°C.

Chapter 7. Co-implantation of Fluorine and phosphorus for the passivation of vacancies in highly doped n-type germanium

I. Introduction

Drawing a map of the point defects that exist in germanium, their electronic signature, their relation, their annealing behavior, etc. is an important task that we have undertaken using DLTS and radiation studies. However, our goal is more than just characterizing defects. It is also to use them, design around them, engineer them, with the ultimate goal of creating better devices. Among them, low resistance ohmic contacts, lasers and MOSFETS are all applications whose operation depends critically on having very high free electron concentrations. In highly doped *n*-type germanium (for $n > 10^{19}$ cm^{-3}), regardless of the doping method employed (i.e. ion implantation, gas phase, in-situ, spin-on diffusion, multiple implantations et cetera [77]–[83]), the activation of donors in conventionally (i.e. furnace or rapid thermal) annealed films is only partially completed and apparently saturates well below 10^{20}cm^{-3} (~5x10^{19} cm^{-3} in the case of an industry standard dopant implantation), despite chemical concentrations often well in excess of this [77], [79], [80], [84], value. This partially activated concentration persists despite the fact that the solid solubility limit of many donor species in germanium (e.g. 2x10^{20}cm^{-3} for phosphorus [85]) is well above this apparent maximum active concentration.

The discrepancy between the measured chemical and electrically active (free carrier) concentrations in germanium is usually attributed to the formation of donor-vacancy cluster (D_nV_m) that are acceptor-like and prevent the donor occupation of substitutional lattice sites [79], [81], [86]. This is precisely the mechanism responsible for the observed *n-to-p* conversion of low doped germanium after gamma-ray irradiation [87]. In addition to electrical inactivation, the presence of a high concentration of vacancies in the material removes potential donors from the desired active region *via* vacancy-assisted enhanced diffusion [14, 15]. One way to limit the vacancy concentration is to annihilate them with a high temperature anneal process but this is not always compatible with the thermal budget of the device or process and can lead to broadening of the dopant profile, which is undesirable in shallow junction devices. There exist a number of defect engineering strategies that can be used to overcome some of these issues by minimizing donor-vacancy interactions; interstitial injection, strain engineering, irradiation [89] and co-doping [90]. Of these, co-doping is especially promising because it is straight-forward to implement in a standard semiconductor process flow. In this case, vacancies or interstitials bind preferentially to the co-doped element reducing its reactivity with substitutional donors. This is analogous to carbon (C) [21] and nitrogen (N) [18, 19] doping in silicon, both of which were employed, with some success, to limit dopant diffusion during thermal processing. However, these studies also revealed that, as well as binding to vacancies, both C and N will also readily form complexes with the donors themselves. Consequently, the successful blocking of donor diffusion comes at the relatively high price of limited electrical activation levels, because of the formation of electrically neutral defect states. A successful co-doping process should therefore selectively passivate the negatively charged vacancies without associating with the positively charged donor ions. Due to its strong electronegativity, a natural candidate for co-doping is fluorine. Table 7 summarizes the reported binding energies of specific D_nV_m and fluorine-vacancy (F_nV_m) complexes, some of which were determined experimentally and others obtained from Density Functional Theory (DFT) calculations [93]. Importantly, DFT predicts that a large fraction of the vacancies should be preferentially consumed within F_nV_m, rather than by D_nV_m or donor-fluorine complexes. There is also experimental evidence of the successful passivation of germanium-oxide interface states with fluorine [94]–[97], demonstrating, at the very least, a material compatibility and the possibility that a similar effect can be obtained for defects in the bulk of epitaxially grown germanium films.

Despite the positive outlook, attempts at using fluorine to passivate vacancies have so far only yielded relatively minor improvements over fluorine-free (donor-only) implanted material. In this chapter, we describe the challenges for co-implanted fluorine in germanium and discuss targeted approaches that have the potential to overcome them. The emphasis of this contribution highlights the strong interaction between fluorine and (i) the amorphous/crystalline (a/c) interface and (ii) the implanted end of range (EOR) damage region, as well as the corresponding diffusion and activation of donors. We discuss the critical aspects for consideration when co-implanting donor species with fluorine for highly efficient electrical activation in germanium.

Defect cluster	Binding Energy, E_b (eV)
PV	-0.52 [98]
PF	-0.55 [93]
AsV	-0.60 [98]
AsF	-0.52 [93]
SbV	-1.05 [80], [86] 0 to -0.80 (experimental) [16]
FV	-1.19 [93]
F_2V	-2.22 [93]
FV_2	-1.94 [93]

Table 7. Binding energies of various D_nV_m (D = P, As, Sb) and F_nV_m clusters, from a range of sources (indicated). The relatively large binding energies of the F_nV_m complexes indicates that a large fraction of the vacancies should be preferentially consumed within these, rather than in either donor-vacancy or donor-fluorine associates.

II. Fluorine in germanium

Following on from the seminal DFT study of F_nV_m clusters by Chroneos et al. [93], a number of experimental studies were undertaken to examine the effect of fluorine on the electrical activation of both phosphorus (P) and Arsenic (As) donors in germanium. Published experimental studies have tended to focus on ion-implanted germanium and so the analysis of the dopant diffusion is somewhat convolved with the effect of Transient Enhanced Diffusion (TED) and the advancing amorphous-crystalline interface during high temperature regrowth annealing.

a. Fluorine-free (Donor only) implantation

Before describing the impact of fluorine on the properties of implanted donors in germanium, we briefly review the case of fluorine-free (donor-only) implanted material. Ion implantation is now the industry standard technique for obtaining high, non-equilibrium dopant concentrations in semiconductors. Ion implantation is an extremely well documented process in both silicon and germanium and is used to reach concentrations beyond the solid solubility of the dopant species, which is normally the limiting factor in so-called ‘drive-in’ methods, such as diffusion doping [99], [100]. As the name suggests, ion implantation consists of bombarding a sample surface with isotopically pure ions to intentionally introduce impurities into the target volume at very specific depths and with well controlled concentrations, determined by the ion energy and the time integrated beam current, using state-of-the-art accelerator technology. One of the consequences of this process is lattice damage that results from collisions between the ions and the target atoms. Lattice damage is reasonably well understood and damage profiles can be predicted relatively accurately using *Monte-Carlo* simulations such as *Stopping and Range of Ions in Matter (SRIM* [36]*)*. Notably, if the energy transferred per atom is above a certain threshold (~5eV for germanium [101]), then the implanted region, i.e. that which extends from the surface to just past the ion projected range, or depth of implantation peak, will be completely amorphized. Following implantation, damage removal and proper incorporation of the implanted donors at substitutional lattice sites in the target (so that they are electrically 'active') therefore requires a subsequent high temperature annealing step, known as an 'activation' anneal. Where amorphization does occur during implantation, this annealing step leads to what is known as Solid Phase Epitaxy (SPE) during which recrystallization occurs, leading to a near perfect recovery of high quality crystalline material. The re-growth rate, or progress of the advancing a/c interface towards the implanted surface, is normally much faster than the rate at which the implanted species diffuse, which means that dopant redistribution can be minimal during full re-growth at high temperatures. For instance, in the case of germanium, a nominal 1 second anneal at 600^{o}C corresponds to a regrown length of 3 µm [101], while the corresponding diffusion length of phosphorus under intrinsic condition is only 0.2 nm [31]. Such a fast anneal is possible using Rapid Thermal Annealing (RTA) instead of conventional furnace annealing, and 1 second at this temperature is sufficient to complete SPE with little to no loss of donors by diffusion [77]. Generally, a higher annealing temperature also correlates with a higher activation of the donor [102], [103]. For donor concentrations in excess of $2x10^{19}$ cm^{-3}, there also exists an enhanced concentration-dependent diffusivity [77], [103], which results in box-shaped concentration profiles, especially for samples annealed for longer time periods. Unfortunately, as with conventional furnace annealing, there still appears to be a maximum achievable carrier concentration (~5x10^{19}cm^{-3}) in germanium for RTA, regardless of the chemical concentration of donors above this, which can be as high as 10^{21}cm^{-3} [77], [79], [103] [104]. Circumventing the detrimental effects of dopant out-diffusion and surpassing this upper bound for the electrically active concentration can be achieved using still faster dynamic annealing processes such as flash lamp [105] or laser annealing [106], [107]. However, these ultra-fast techniques come with their own limitations, such as sharp thermal gradients that can lead to ablation at the surface and a limited anneal depth, as well as large diffusion within the melt region for deeper implants and metastability of the donors above the solid solubility limit (and hence even more stringent thermal constraints for future processing).

b. Fluorine interaction with the a/c interface during the solid phase epitaxy of P+F implanted Ge

After regrowth annealing of a germanium sample co-implanted with fluorine and phosphorus, the profile of the halogen element is much more affected than the profile of the donor, even for short annealing durations. Figure 60 shows the chemical concentrations of fluorine and phosphorus, from Secondary Ion Mass Spectrometry (SIMS) in as-implanted samples and samples annealed at a peak temperature of 600°C for nominally 2 seconds (25 second ramp-up from room temperature to 600°C and 260 second ramp-down from peak temperature to 100°C), in a 1 µm epitaxially grown film of germanium on silicon, in-situ doped with phosphorus to a background level of 10^{19} cm^{-3} [108]. While the distribution of phosphorus is virtually unaffected by the RTA, most of the fluorine has out-diffused after this anneal (the background concentration of fluorine at

10^{17} cm^{-3} is an artefact and corresponds to the sensitivity limit of the SIMS measurement and as such the real concentration could be much smaller than this).

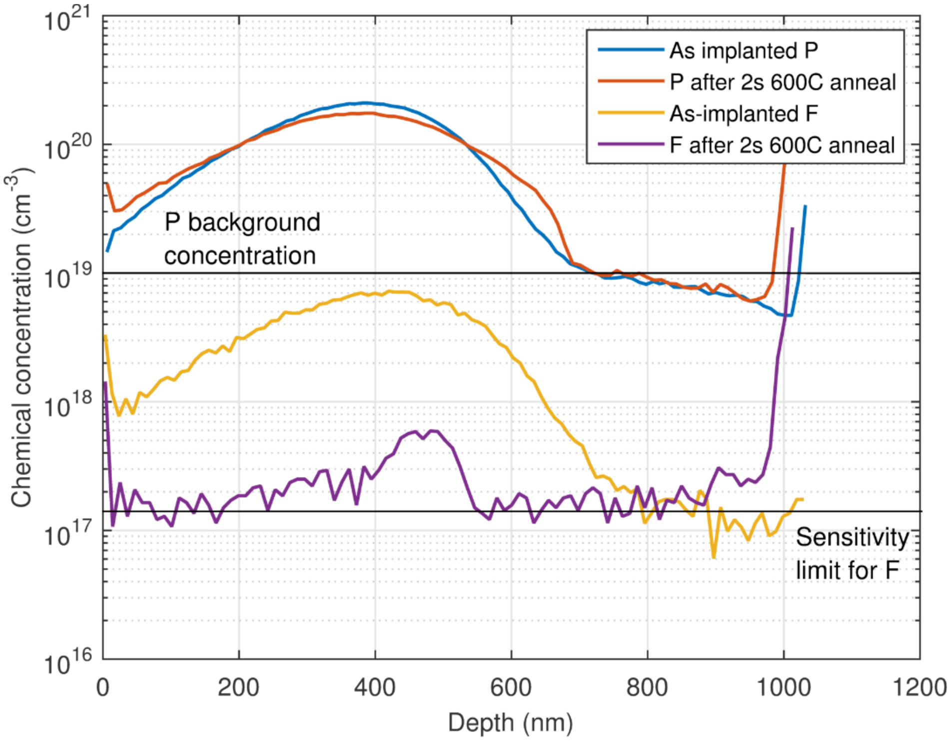

Figure 60. SIMS profiles of as-implanted and post-RTA concentrations of phosphorus (350 keV, 4.6x10^{15} cm^{-2}) and fluorine (210 keV, 2.5x10^{14} cm^{-2}) in a 1 µm epitaxial film of Ge-on-Si. The phosphorus profile is virtually unchanged after annealing, while most of the fluorine has out-diffused [108]. The spike of concentration at a depth of 1000 nm is an artefact from the germanium/silicon interface.

The efficient out-diffusion of fluorine is mainly due to a high segregation at the a/c interface. Figure 61 shows the fluorine concentration from SIMS data superimposed on a *Transmission Electron Microscopy* (TEM) image [36]. Fluorine that is preferentially bound to the amorphous material at the a/c interface [109]–[111] is ‘pushed’ towards the surface during SPE regrowth. This ’pinning’ of fluorine to the more damaged amorphous areas of the material is due to the high electronegativity of the halogen, which translates into a strong binding affinity for point defects and dangling bonds, which themselves segregate preferentially on the amorphous side of the a/c interface [112].

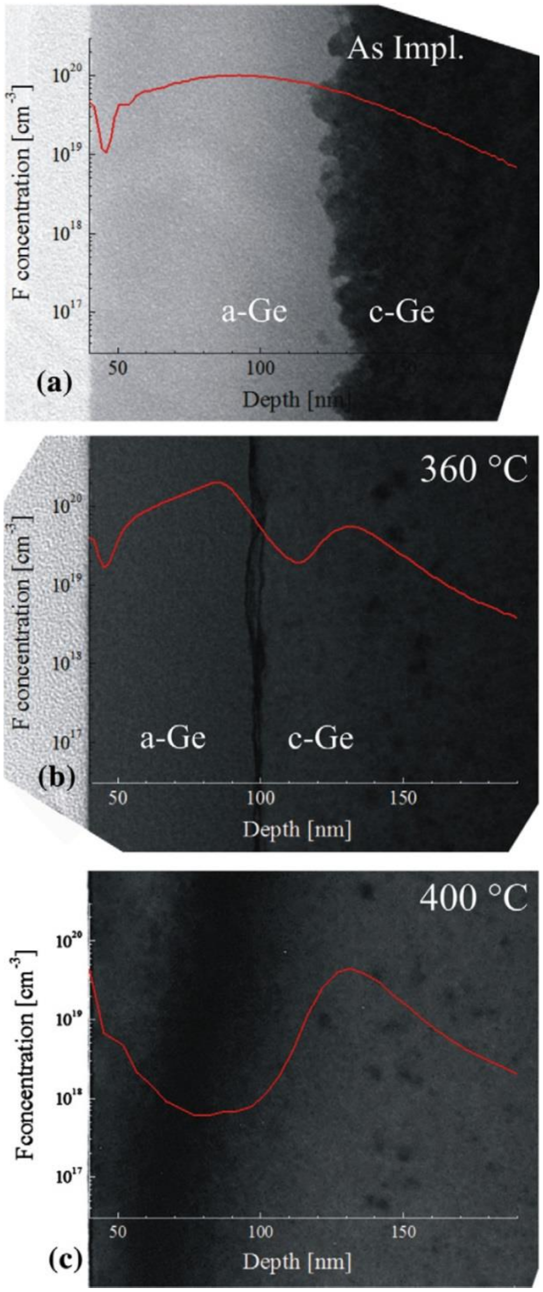

Figure 61: TEM micrographs superimposed with SIMS profiles of the fluorine concentration in germanium. The implant energy and dose were respectively 35 keV and $1x10^{15}cm^{-2}$ *for As-implanted (a) and annealed for 1 hour in* N_2 *at 360°C (b) and 400°C (c)* [109]. *The images demonstrate the fluorine segregation to the a/c interface and EOR regions. The apparent increase in fluorine concentration close to the surface is an artefact of the measurement. Reprinted from Ref.* [109], *Copyright 2012, with permission from Elsevier.*

In contrast, for samples implanted below the amorphization threshold and in which there is no SPE during the anneal (Figure 62) [111], no significant out-diffusion of fluorine was observed, even for a one hour anneal at 400°C. This indicates that the extremely high diffusion coefficient reported for fluorine in germanium ($\sim 10^{-10}$ cm^{2}s^{-1} at 400°C [113]), is rather the result of efficient segregation of fluorine to the a/c interface, mediated by point defects. This affinity of fluorine for point defects also results in a retardation of the SPE growth rate [109], and in an incomplete removal of the defects from the material, again confirming their stabilization by fluorine. Specifically, Positron Annihilation Lifetime Spectroscopy (PALS) studies [114] [111] [109] reveal that vacancies and vacancy clusters remain in regrown regions, even after anneals as high as 500ºC for fluorine co-implanted material, while no such defects could be detected using the same technique for identical annealing conditions in fluorine-free (donor-only) implanted material (in the case of a sub-amorphization threshold dose of fluorine, most of the defects can be removed, but for a thermal budget higher than in fluorine-free material). In samples that were implanted with an amorphizing dose of fluorine, the defects remaining after annealing also have a larger free volume (i.e. positrons exhibit longer lifetimes).

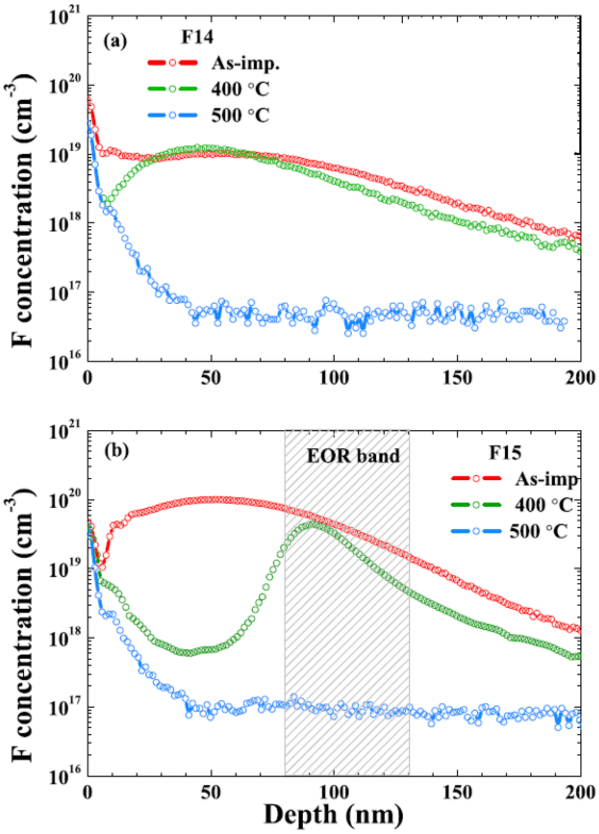

Figure 62: As-implanted (50 keV) and annealed (1 hour in N_2) SIMS fluorine profiles in germanium for doses of (a) 10^{14} cm^{-2} and (b) 10^{15} cm^{-2}. The higher (amorphizing) dose is followed by SPE during annealing, which carries much of the fluorine away, even for anneal temperatures as low as 400ºC. In contrast, the lower (non-amorphizing) dose is not followed by SPE, which leads to an unchanged fluorine concentration after the 400ºC anneal. At 500°C, the EOR is no longer stable and the fluorine out diffuses, regardless of the crystallinity. © IOP Publishing. Reproduced with permission from Ref. [111]. All rights reserved.

Defects introduced by implantation in germanium have an acceptor-like behavior [114], [115], and thus a measure of the concentration of free holes by Spreading Resistance Analysis (SRA) is also a measure of the amount of implantation damage. Impellizzeri et al. [114] and Jung et al. [115] both employed SRA to obtain post-annealing defect concentrations in samples that were implanted respectively above and below the amorphization threshold. Both studies confirmed that implantation damage results in the introduction of acceptors and therefore p-type conductivity. SRA data from [114] (Figure 63) appears consistent with the PALS data in that defects remain after annealing in fluorine implanted material. However, the free hole concentration (measured by

SRA) is not directly proportional to the chemical concentration of fluorine (measured by SIMS), which means that it is unlikely that all the acceptor defects (responsible for the free hole concentration) contain fluorine. In addition, a 450°C anneal counter-intuitively reveals a higher defect concentration than the samples annealed at 400°C, whereas for a 500°C anneal, fewer defects are observed (as well as a complete removal of fluorine). Fluorine thus appears to act as a catalyst for defect formation during SPE yet does not actually form part of the defects themselves.

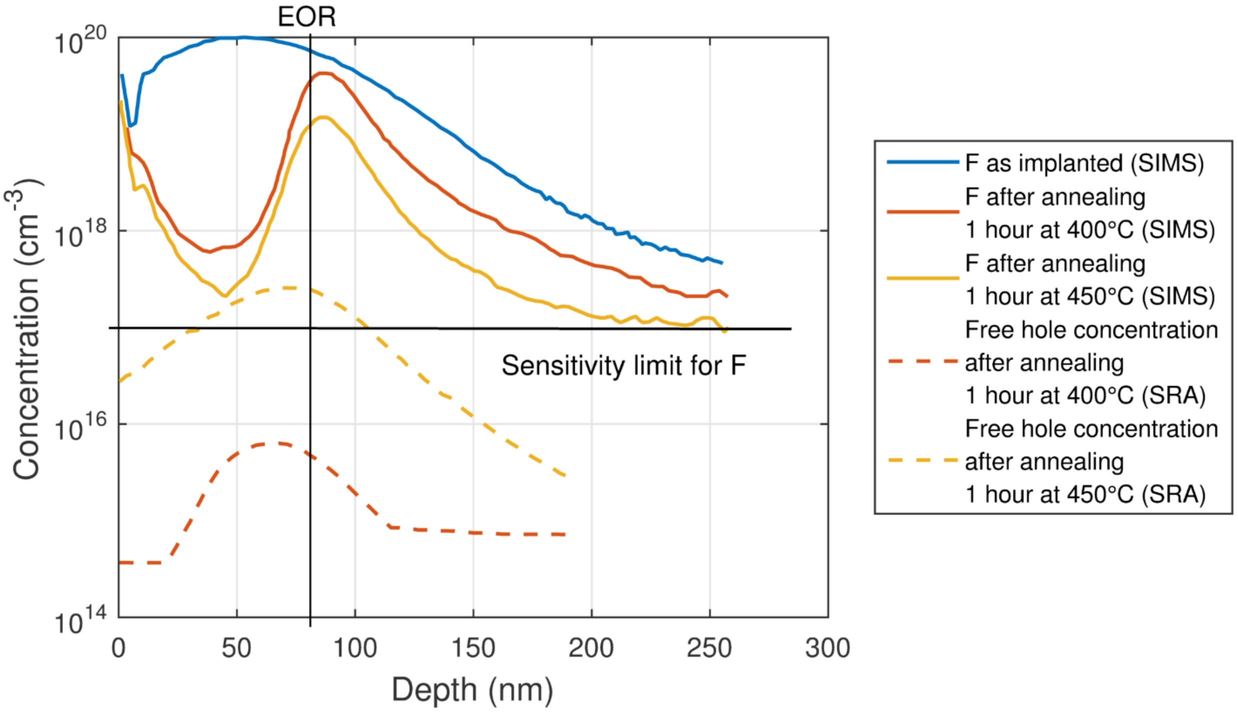

Figure 63: SIMS profiles and free hole concentrations (measured by Spreading Resistance Analysis) of as-implanted (fluorine at 35 keV to 10^{15}cm^{-2}) and annealed (400ºC and 450ºC for 1 hour in N_2) germanium, indicating p-type conductivity (data extracted and replotted from Ref. [114], FIG. 1 and FIG. 3). The apparent increase in fluorine concentration close to the surface is an artefact of the measurement. Reproduced with permission of The Electrochemical Society.

On the other hand, the data from Jung et al [115] (Figure 64) seems to contradict that reported by Impellizzeri et al [114], with the former observing a reduction of free hole concentration after annealing fluorine implanted material. This difference in behavior is likely due to the different experimental conditions employed in the two studies: (i) In Impellizzeri [114], a 1 hour long furnace anneal was employed, whereas in Jung [115], only a nominal 10 second RTA anneal (at higher temperature) was employed, which would have had the effect of minimizing the diffusion of the species and preventing the formation of low temperature defects; (ii) In Jung [115], a lower (non-amorphizing) dose of fluorine was employed and thus, unlike that of Impellizzeri [114], would not have incurred SPE during annealing, with no excess of acceptor-like defects, beyond those introduced by the implantation. It is likely that the defects reported in Impellizzeri [114] were catalyzed by the fluorine at the a/c interface during regrowth, a process which is absent in a fully crystalline sample. More precisely, the results of Jung [115] may be summarized as follows: RTA of a ‘control’ sample (self-implanted intrinsic germanium) for 10 seconds at 500°C was sufficient to recover the crystallinity of the material, but insufficient in removing all of the implantation defects. A subsequent sub-amorphization fluorine implant then yielded an increased hole concentration (as a result of irradiation damage), but after a 10 second RTA at 500°C, the number of electrically active defects in this sample was found to be much smaller than for the ‘control’, (Figure 64). In addition, the influence of a sub-amorphization threshold dose of fluorine in an epitaxially grown, lightly p-doped Ge-on-Si wafer was assessed (“blanket Ge + F + Anneal” curve of Figure 64) using SRA and this revealed a reduction of the free hole concentration. In both cases (self-implanted Ge and blanket film), the introduction of fluorine appears to have resulted in a passivation of the electrically active defects; the key to utilizing this will be to find ways to prevent the effective, SPE mediated out-diffusion of fluorine.

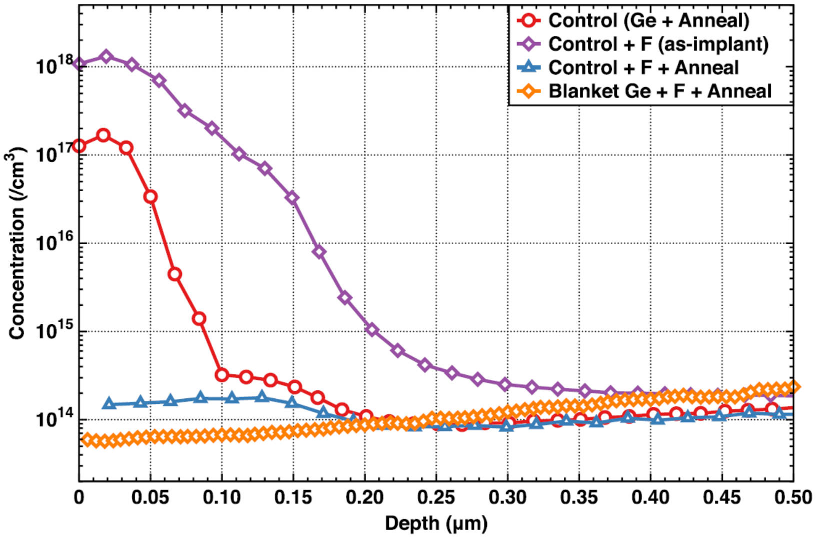

Figure 64: SRA of various fluorine implant combinations with annealing (RTA at 500°C for 10 seconds). The presence of vacancy type defects gives rise to the p-type conductivity, which can be seen to be suppressed in the ‘Control + F + Anneal sample, evidencing F passivation of vacancies. Reprinted with permission from Ref [115]. Copyright 2012, AIP Publishing LLC.

c. Interaction of fluorine with the end-of-range (EOR) defects

In addition to its segregation at the a/c interface, fluorine rapidly diffuses to the interstitial rich EOR region, as shown in Figure 61, Figure 62 and Figure 63, and remains there during subsequent anneals until the EOR itself dissolves. Similar to the retarding influence of fluorine on the SPE growth rate, the fluorine appears to stabilize the EOR [110] [109], as evidenced by the higher temperature required to dissolve defects in this region when the halogen is present. The EOR also seems to act as a diffusion barrier for the fluorine; as shown in Figure 61. After a one hour anneal at 400°C only one percent of the fluorine is left in the region that was amorphized by the fluorine implant (to a depth of 80 nm), while the concentration of fluorine in the most defective part of the EOR (between 80 nm and 100 nm) is virtually unaffected (and it is only halved for the region just past the EOR). This is surprising and demonstrates that the fluorine not only binds to vacancies, but also likely to interstitials (which are numerous in the EOR) and would explain why fluorine stabilizes this damaged region. This is, however, problematic for diffusion control and activation enhancement of the dopants because i) the interstitials are a sink for vacancies so stabilizing them inhibits any role they might play in annihilating vacancies and ii) fluorine atoms that passivate interstitials do not passivate vacancies and are effectively inactive. Therefore, care needs to be taken when designing the implantation conditions and it would appear beneficial to perform a pre-amorphization implant (PAI) prior to the fluorine implant to de-couple the EOR depth from the implantation peak of the fluorine (and the co-implanted donors). This would ensure that the fluorine does not diffuse out of the active region toward the EOR, although this alone would not solve the issue of fluorine following the a/c interface during regrowth.

d. Diffusion of fluorine and of donors

Due to the strong interaction of fluorine with the a/c interface and EOR damage regions, it is difficult to determine the diffusivity of fluorine in germanium. It has been estimated at around 10^{-10} $cm^2 s^{-1}$ [113] at 600°C because, at this temperature, it 'out-diffuses' from the implanted junction at a range of around 50 nm in less than a second. However, this particular study [113] does not appear to have taken into account the strong coupling of fluorine with the a/c interface and the transient effects of the SPE described earlier. An alternative estimate for the fluorine diffusivity in germanium can be extrapolated from the sub-amorphization implants reported by Sprouster et al. [111] (Figure 62), from which the diffusivity is determined to be closer to 10^{-15} cm^2s^{-1} at 400°C (diffusion over a few tens of nanometers for a one hour anneal) and around 10^{-13} cm^2s^{-1} at 500°C (total out-diffusion over hundreds of nanometers in one hour). These evaluations are consistent with the estimation of 10^{-15} $cm^2.s^{-1}$ and 10^{-14} $cm^2.s^{-1}$, respectively at 400°C and 450°C, that can be extracted from furnace anneal experiments by Impellizzeri et al. [110]. In this set of experiments, although the fluorine implant dose was amorphizing, which complicates any estimate of the diffusivity in the peak implanted region, the concentration profiles were also reported for the non-amorphized region, just past the EOR. Therefore, assuming a stable EOR region, the diffusion of fluorine in the 'bulk' of these samples would not likely have been affected by transient enhanced diffusion. Of course, because these approximations are performed in highly defective materials, they are only measurements of the diffusivity of fluorine in germanium under extrinsic conditions.

Regarding the impact of fluorine on the as-implanted profiles of donors in germanium, Mubarek et al. [116] compared phosphorus profiles in materials with and without pre-implanted fluorine. This work determined that the as-implanted phosphorus profiles were shallower in the presence of fluorine. However, in a comparative study of the effect of fluorine on the Arsenic (As) concentration in materials following a PAI, Impellizzeri et al. [110] observed similar As profiles with and without fluorine. This suggests that fluorine is not responsible for the difference of as-implanted donor profiles, and that the difference is due to different experimental parameters (especially the lack of a PAI in the former study) and perhaps the relative masses of P and As, which results in a higher backscattering rate (for the lighter element) during implantation. After (furnace) anneals below 500°C, both studies reported a contraction of the donor concentration profiles (due to out-diffusion of the donor), whether fluorine was present or not. Additional studies have reported that fluorine had no impact [102], [110], [113], [116] on the diffusivity of phosphorus at the implantation peak. However, this is not surprising given that those studies would all have been subject to the almost complete outgassing of fluorine occurring during the SPE, i.e. the effect of fluorine on the donor profiles is mooted by its removal during SPE. On the contrary, past the EOR, where fluorine is still present after SPE, the tail of the donor profiles are sharper in the sample co-implanted with fluorine, indicating that, when present, fluorine is indeed capable of reducing the donor diffusivity in germanium. In addition, even if much of the fluorine has diffused out of the implantation peak area, it may still be present in the EOR, where it can act as a diffusion barrier, which perhaps explains why materials co-implanted with the halogen also tend to display more 'box-like' dopant distributions.

e. Interaction between fluorine and donors

In addition to complicating the control of donor diffusivity, the rapid outgassing of fluorine during SPE presents a similar challenge to controlling the activation of donors in germanium. However, some clear trends do exist. For instance, contrary to other neutral species like carbon, fluorine does not readily cluster directly with donors [110]. Further, for sub-amorphization threshold implants in p-type germanium, where the free carrier concentration is largely influenced by the implantation defects (irradiation damage incurred prior to any fluorine implant), rather than by dopants [115], the introduction of fluorine reduces the concentration of free holes compared with control wafers, which means that the fluorine can be effective at passivating acceptor defects. That said, the interaction of fluorine with donors in the high concentration limit, remains as yet, unknown.

In order to estimate the fluorine dose required to increase the activation of donors in highly doped germanium ($n > 1x10^{19}$ cm^{-3}), we develop a model here to explain the chemical interactions between vacancies, fluorine and donors (we employ only phosphorus here, as an example). We assume a system at chemical equilibrium and consider the following reactions: association of a substitutional phosphorus atom with a vacancy (Equation 18), association of a fluorine atom with a vacancy (Equation 19) and association of two fluorine atoms with a vacancy (Equation 20). For consistency and because the binding energy of fluorine and vacancies in germanium is not determined experimentally, we use the binding energies previously calculated using *Density Functional Theory* by Chroneos et al. [93] (respectively 0.52 eV, 1.19 eV and 2.22 eV), with pre-factors (necessary for homogeneity reasons) equal to the coordination number in Ge (e.g. the number of ways the reactants can bind to one another) divided by the number of lattice sites. In the case of the phosphorus-vacancy (PV) complex, the reaction contains an additional $\frac{n}{n_i}$ term (with n the free carrier concentration and n_i the intrinsic carrier concentration), as shown in Equation 21, in order to describe the self-compensating effect that occurs at high dopant concentrations. We further assume that for highly n-type material, most of the single vacancies are in the double acceptor charge state [117], that the unbound fluorine atoms are in a single acceptor state (due to their high electro-negativity), that the PV centers are double acceptors [16], [43], that the FV complexes are in the single acceptor state and that the F_2V centers are neutral (decoration of the dangling bonds by the fluorine). These assumptions yield Equation 22, which defines the free electron concentration in the material. Equation 23 and Equation 24 describe the conservation of phosphorus and fluorine, respectively. Finally, in this framework, we cannot assume that the population of vacancies is at thermal equilibrium, because of the limited maximum free electron concentration that is observed experimentally, regardless of the chemical concentration of donors and annealing temperatures during RTA. To take account of this, we treat the total concentration of vacancies (Equation 25) as a fitting parameter to ensure that the system of equations yields a free electron concentration at this limit (i.e. $5x10^{19}$ cm^{-3} in the case of a single-step P ion implantation), in the absence of fluorine. Despite the simplicity of our model in neglecting the formation of any multi-vacancy clusters, the interaction of P and F, as well as any diffusion limited reaction, the data provides useful insight into the impact of fluorine on free carrier concentration in heavily phosphorus-doped germanium.

$$P^{+} + V^{2-} + e^{-} = PV^{2-} \quad \text{(Equation 18)}$$

$$F^{-} + V^{2-} = FV^{-} + 2e^{-} \quad \text{(Equation 19)}$$

$$2F^{-} + V^{2-} = F_2V + 2e^{-} \quad \text{(Equation 20)}$$

$$K_{P+V=PV} = \frac{[PV^{2-}]}{[P^{+}][V^{2-}]} = \frac{4}{N_0}\frac{n}{n_i}\exp\left(-\frac{0.52}{kT}\right) \quad \text{(Equation 21)}$$

$$n = [P^{+}] - 2[PV^{2-}] - 2[V^{2-}] - [F^{-}] - [FV^{-}] \quad \text{(Equation 22)}$$

$$P_{total} = [P^{+}] + [PV^{2-}] \quad \text{(Equation 23)}$$

$$F_{total} = [F^{-}] + [FV^{-}] + 2[F_2V] \quad \text{(Equation 24)}$$

$$V_{total} = [PV^{2-}] + [V^{2-}] + [FV^{-}] + [F_2V] \quad \text{(Equation 25)}$$

Figure 65 shows the result of this model in the absence of fluorine for a temperature of 600°C and a chemical concentration of phosphorus corresponding to its solid solubility in germanium (2x10^{20} cm^{-3}), treating the total number of vacancies as an unknown variable. For a small number of vacancies, most phosphorus atoms are substitutional, and the activation level is close to 100%. But as the number of vacancies increase, so does the number of PV associates, resulting in a drop in the free carrier concentration. When the free electron concentration becomes too low, the formation of PV centers becomes unfavorable, and mono-vacancies dominate the vacancy population. Experimentally, the free carrier concentration is capped at 5x10^{19} cm^{-3}, which for a phosphorus concentration of 2x10^{20} cm^{-3} corresponds to a total concentration of vacancies of 5x10^{19} cm^{-3} (intersection of the experimental and modeled free carrier concentrations in Figure 65), which serves as an approximation of the number of vacancies present in the material. Next, we model how the fluorine dose influences the free carrier concentration, for example in Figure 66, the free electron concentration is plotted as a function of the fluorine dose, for total vacancy concentrations of 2.5x10^{19} cm^{-3}, 5x10^{19} cm^{-3} and 7.5x10^{19} cm^{-3}, respectively. All three curves show a regime in which the free carrier concentration is linearly correlated with the fluorine dose, with a slope, dn/dF ~1.6. This indicates an enhanced activated fraction of the donors and is due to the fact that the conversion of a double negatively charged PV center into a substitutional donor and a single negatively charged FV (or neutral F_2V) complex results in the net gain of 2 (or 3) electrons, even though the unbound fluorine atoms (being acceptors) offset this positive effect. This is why, in Figure 66, the free electron concentration for V_{total}= 2.5x10^{19} cm^{-3} falls for fluorine doses in excess of 5x10^{19} cm^{-3}; there are no vacancies left to passivate and all the excess fluorine atoms behave as acceptors. The model therefore provides critically important design parameters for fluorine co-implanted materials; in order to have a significant effect on the activation of the donors, the concentration of fluorine must be above 10^{19} cm^{-3}, while not exceeding the vacancy concentration, which we estimate from the parameters we have used here, to be on the order of 5x10^{19} cm^{-3}.

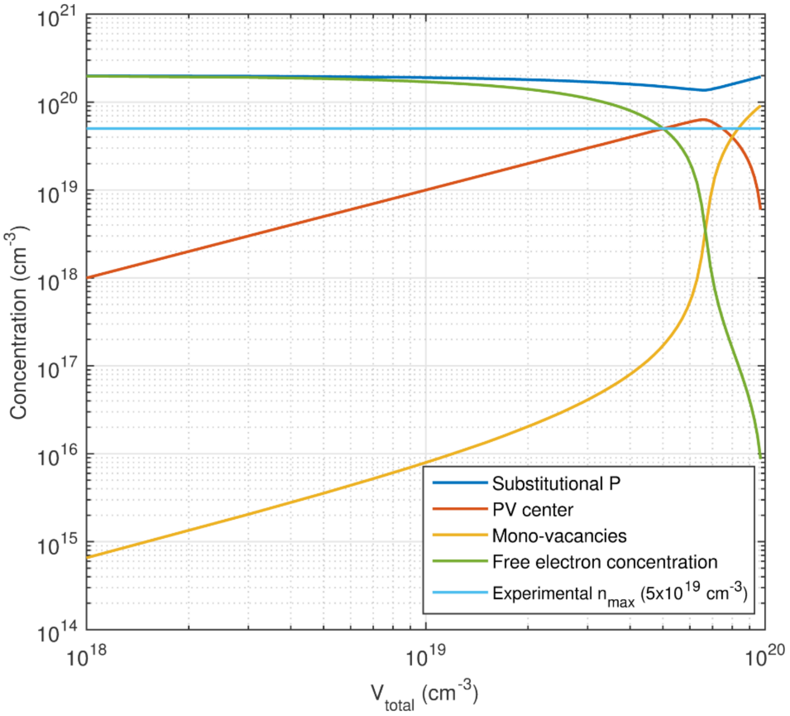

Figure 65: Repartition of P between substitutional sites and vacancy complexes, density of mono-vacancies and free electron concentration as a function of the total number of vacancies present in the sample ($P_{total} = 2x10^{20}$ cm^{-3}, no fluorine). The intersection between the calculated free electron concentration and the experimentally observed maximum of $5x10^{19}$ cm^{-3} for $V_{total} = 5x10^{19}$ cm^{-3} indicates that this is a reasonable estimate of the residual vacancy concentration in the sample after implantation and RTA.

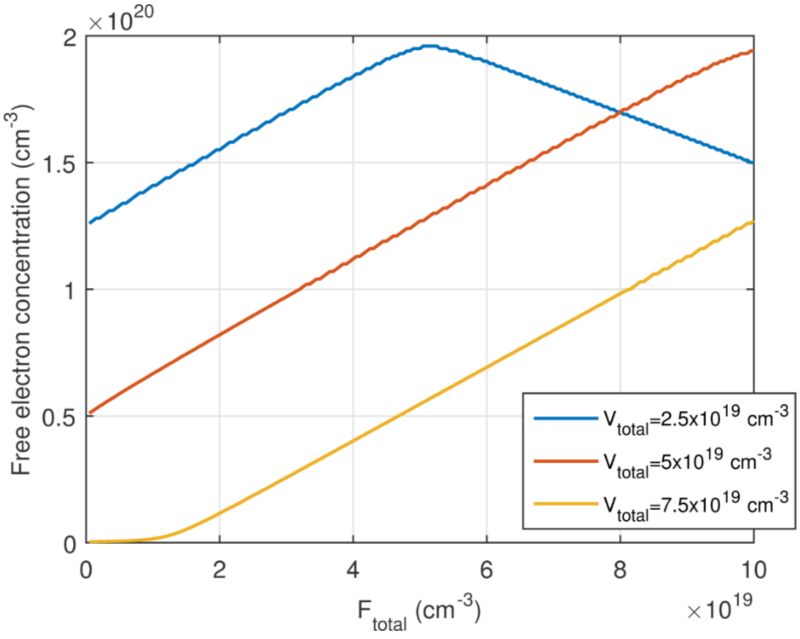

Figure 66: Free electron concentration versus fluorine concentration, for different vacancy concentrations. The influence of fluorine on the activation of phosphorus scales linearly with the dose until the concentration of fluorine exceeds the total number of vacancies, above which its acceptor-like characteristic results in a decrease of free electron concentration.

III. Implementation of strategies to prevent the fluorine out-diffusion

a) Experimental plan for an increased retention of fluorine

In the previous paragraphs, we have established that the major problem for an efficient passivation of point defects by fluorine is outdiffusion. It is obvious from Figure 60 that, even for extremely short (nominally 1s) RTAs at 600°C, the regrowth-mediated out-diffusion is difficult to control. One approach to circumvent this apparent rapid outgassing of the halogen is the use of much faster thermal annealing processes. For instance, Flash Lamp Annealing (FLA) and Pulsed Laser Melting (PLM) are ways to accelerate SPE dynamics, with melt durations in the millisecond and sub-microsecond ranges respectively. Indeed, early results [118] reveal that there is little diffusion of the halogen after PLM in a phosphorus and fluorine co-implanted sample, and that fluorine can prevent the ablation observed during high energy pulsed annealing of fluorine-free (donor-only) implanted material. Ultra-fast processing methods can be promising techniques, which have also been shown to preserve the strain in Ge-on-Si epitaxial thin films [118], particularly important for laser materials. However, these processes do come with their own limitations in terms of stability [119], partial defect removal [120] and thickness: higher energies are necessary for thicker films and ablation control can be highly dependent on defect densities in the starting material.

Another possible solution is the implementation of a two-step implant process; first the donor implant, followed by RTA to regrow the crystal before finally employing a non-amorphizing fluorine implant. Amorphization happens when the number of defects introduced in a material reaches a certain limit (Critical Point Defect Density [121]), which gives rise to a dose threshold below which the sample remains crystalline. This limit depends on the relative weight of the implanted ions and the lattice atoms, which determines the intensity of collision cascades. The threshold is 3×10^{21} vacancies/cm^3 [101] in the case of self-implanted germanium, and is likely higher for a fluorine implant, because it is a lighter element. The amorphization threshold can be increased by implanting into a hot wafer (100°C-200°C), in which the higher mobility of the germanium atoms can provide a dynamic annealing of the Frenkel pairs, which increases the rate at which the newly created interstitial and vacancy defects self-annihilate, hence preventing the damage build-up. We will refer to such samples as “hot wafer” implants. Another solution is to do multiple low dose implants, intertwined with RTA anneals to remove most of the irradiation damage between implants and thus never exceeding the Critical Point Defect Density. This method will be called an “intertwined” implant in the paragraphs that follow. These different approaches are presented schematically in Figure 67.

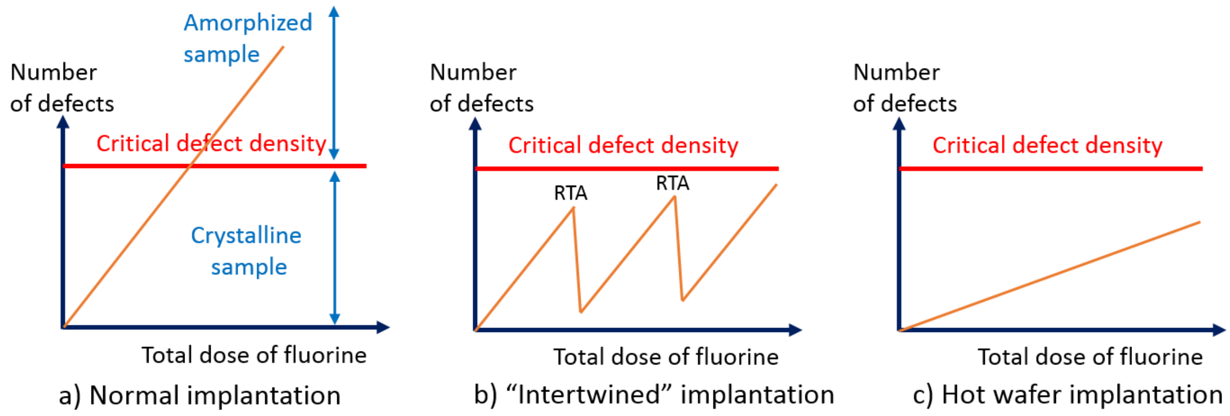

Figure 67: Schematic of the different strategies to avoid the amorphization critical density of defects in germanium, while implanting large doses of ions: a) classic implantation b) "Intertwined" implantation, where RTA is performed between sub-amorphization threshold dose implants and c) Hot wafer implantation, with a higher dynamic annealing of the Frenkel pairs resulting in a lower net defect generation rate.[108]

b) Methodology

We have experimentally tested 3 strategies to increase the retention of fluorine: the intertwined implant, the hot wafer implant, and the use of laser annealing after a shallow implant. This study was performed on germanium grown epitaxially on 6" silicon substrates, either by Ultra High Vacuum Chemical Vapor Deposition (UHVCVD) or Low Pressure Chemical Vapor Deposition (LPCVD) on a low-doped Czochralski p-type prime silicon wafer. In order to accommodate the 4% lattice mismatch between germanium and silicon, a two-step deposition process[50] is used: first a low temperature buffer layer is grown to prevent islanding of germanium, then a high temperature growth is used to produce good quality material and obtain higher growth rates. After the deposition, a cyclic annealing is done to reduce the threading dislocation density in the layer. As a result, only a small region at the Si-Ge interface (the first tens of nanometers above the germanium and silicon interface) is highly defective (misfit dislocations), and the rest of the germanium layer has a low threading dislocation density, in the 10^{7} cm^{-2}. The samples were grown undoped, but similar to the Ge-on-Si photodetectors from Chapter 5, the germanium layers have a p-type character due to dislocations and point defects, with an average free hole concentration of 10^{15} cm^{-3}, with a minimum at the free surface and a monotonic increase up to the buffer layer.

After the germanium growth, wafer 1 and wafer 2 were coated by a 30 nm Plasma Enhanced Chemical Vapor Deposition (PECVD) silicon dioxide layer. The role of this layer is to act as a cap and slow down the outdiffusion of fluorine during the multiple RTAs that the intertwined and hot wafer sample have to undergo. The third and last wafer of this study was used for shallower implantations compatible with Pulse Laser Melting (PLM) in which an out-diffusion cap is not necessary.

The germanium layers were implanted at the Ion Beam Centre in the University of Surrey. Prior to the phosphorus implantation, parts of the wafer 1 and wafer 2 were pre-amorphized 10^{14} cm^{-2} germanium ions of energy 900 keV, in order to test the influence of a pre-amorphization implant (PAI). Because the sheet conductivity of the sample that underwent a PAI had a systematically higher sheet conductivity, we are only reporting herein the results on these samples.

No PAI was performed on wafer 3. After the implantation of phosphorus, wafer 1 and 2 were annealed for 2 seconds at 600°C, before the implantation of fluorine. In the case of wafer 3, the fluorine was implanted right after the phosphorus, without intermediate RTA. Different doses of fluorine at different energies were implanted in the germanium epilayers, and the details of the implantations are summarized in Table 8. The four first samples were cut out of wafer 1, the four next out of wafer 2 and samples 9 to 12 originate from wafer 3. Sample 1 is a control sample, a simple phosphorus implantation. Sample 2 to 4 are intertwined implantations with increasing doses of fluorine. Sample 5 to 8 are hot wafer implantations and sample 9 to 12 are shallow implantation that were PLMed after the introduction of the fluorine. The RTAs were performed at a peak temperature of 600°C for 2 seconds, with a 25 second ramp-up and a 260 second cool-down to 100°C. The PLM anneal was performed by a NdYaG laser operating at a wavelength of 355 nm and with a pulse duration of 4 ns.

Sample	1	2	3	4	5	6	7	8	9	10	11	12
E_P (cm^{-3})	200								40			
D_P (x 10^{15} cm^{-2})	5								2			
E_F (cm^{-3})	120							150	23			
D_F (x 10^{14} cm^{-2})	0	0.5	2	4	2	4	10	10	0	0.62	1.6	3.2
Type	Control	Intertwined			Hot wafer implantation				Shallow implantation			

Table 8: Experimental parameters of the implantation. An "intertwined" implantation denotes an implantation of fluorine by dose increments of 5x10^{13} cm$^{-2,}$ with an RTA between implantation. A "hot wafer" implantation denotes an F implantation done in a wafer held at 200°C. An RTA was performed on samples 1 to 8 after the P implantation and prior the F implantation in order to recover the crystallinity of the sample before the F implantation.

c) F retention

Figure 68 shows the Secondary Ion Mass Spectroscopy (SIMS) profiles of samples 1, 4 and 6 (respectively a control fluorine-less sample, an "intertwined" sample and a "hot wafer" sample, the latter two implanted with the same dose of fluorine) after a final 2 seconds 600°C RTA. The measured concentration of fluorine in the control sample is 10^{17} cm^{-3} and corresponds to the noise level of the SIMS measurement. The distribution of fluorine is skewed toward the surface and there is some small accumulation of fluorine at the implantation depth, which coincides with the phosphorus implantation depth (190 nm). This accumulation is larger for higher doses of fluorine, as shown in Figure 70. The F retention is higher for "hot wafer" implants than for the "intertwined" ones. Despite the absence of amorphization and therefore solid phase epitaxy in these samples, the retention of fluorine is low, on the order of 10%. This confirms the low solubility of fluorine in crystalline germanium, which is also the cause of the segregation of the fluorine at the amorphous/crystalline interface, that we have discussed in the section II.b) of the current chapter.

The low solid solubility of fluorine in crystalline germanium is also apparent from the shape of the F profiles after annealing. A normal diffusion profile should have a Gaussian distribution, which gets broader as the annealing duration increases. However, the fluorine distributions after the unamorphizing fluorine implants are highly asymmetric and skewed toward the surface. This difference of behavior is not due to the presence of a SiO_2 cap to slow down out-diffusion: the sample from Figure 60 also had one, and its profile was not that asymmetric. Instead, the cause of this phenomenon is due to the difference of implantation damage. On the one hand, the sample from Figure 60 results from a straight forward co-implantation during which the germanium got amorphized. After SPE, there is little point defects left, and the fluorine that did not outgase has an isotropic diffusion coefficient. On the other hand, the samples from Figure 68 and the other following figures underwent a two-step process: first the phosphorus implant followed by an RTA to recover crystallinity, second a non-amorphizing implantation of fluorine. As a result, the defect profile is anisotropic, with a large concentration of point defects between the surface and the implantation peak (Figure 69). The fluorine distribution reflects the defect distribution: it is the point defect themselves that mediate the solubility of fluorine.

The ideas that fluorine is only soluble in the regions of the crystal with a lot of point defects can also be inferred from Figure 70, which shows the SIMS profile of three hot wafer implantations (after a final RTA), for different doses and ranges. Increasing the dose does not result in a linear increase in the F concentration, and implanting the fluorine further in the material also does not result in a deeper F profile. The as-implanted profiles have little connection with the final profile after annealing, because F redistributes to regions with higher defect concentrations. This is the reason why there is a larger concentration of F at the P concentration peak. F does not interact directly with P (else the distribution of F would be similar to this of P). What binds the fluorine to the region with the highest donor concentration is the presence of larger concentration of point defects, which are present because of the formation of donor-vacancy clusters when the concentration of dopants is higher than the mid 10^{19} cm^{-3} (these defect clusters are the reason why the free electron concentration saturates at around $5x10^{19}$ cm^{-3}, regardless of the chemical concentration of donors). This distribution of fluorine, which tracks point defects independently from implantation position, is further evidence of the low solubility of this element and also a sign of high diffusivity.

In contrast to the deeper implantations that require an RTA, which results in a large redisctribution of the F profiles, shallow implantation can be laser annealed by PLM. The extremely quick solidification dynamics of the melt (around 100 ns) prevents any outdiffusion of the fluorine, as shown in Figure 71. Both the phosphorus and fluorine profiles have barely been affected by the PLM with the fluorine retention staying close to 100%.

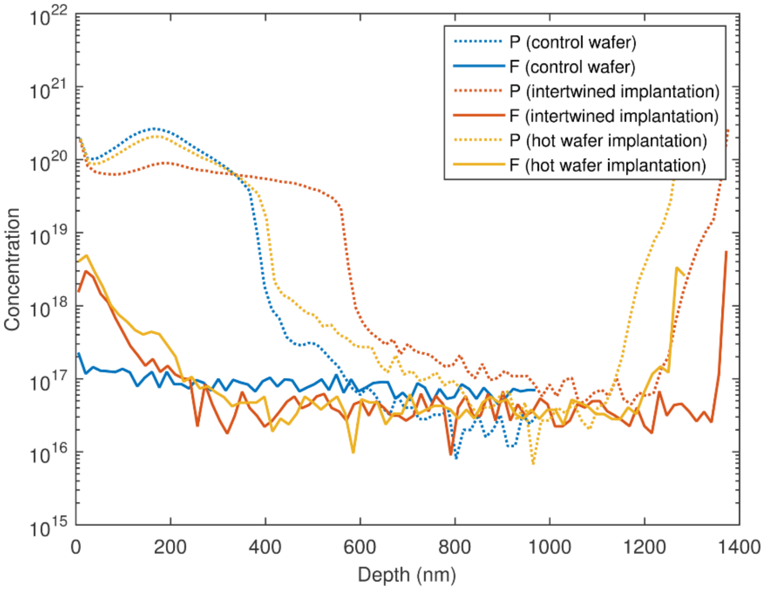

Figure 68: P and F profiles after the final 2 s 600 °C RTA of a "control", "intertwined" and "hot wafer" implantation (pre-amorphized samples, E_P=200 keV D_P= 5x10^{15} cm^{-2} E_F= 120 keV D_F=4x10^{14} cm^{-2}).The distribution of fluorine is skewed toward the surface and there is some accumulation of fluorine at the implantation depth (190 nm) in the hot wafer sample. No fluorine is accumulated at 190 nm in the intertwined scheme, possibly because of the higher thermal budget from the multiple RTAs.

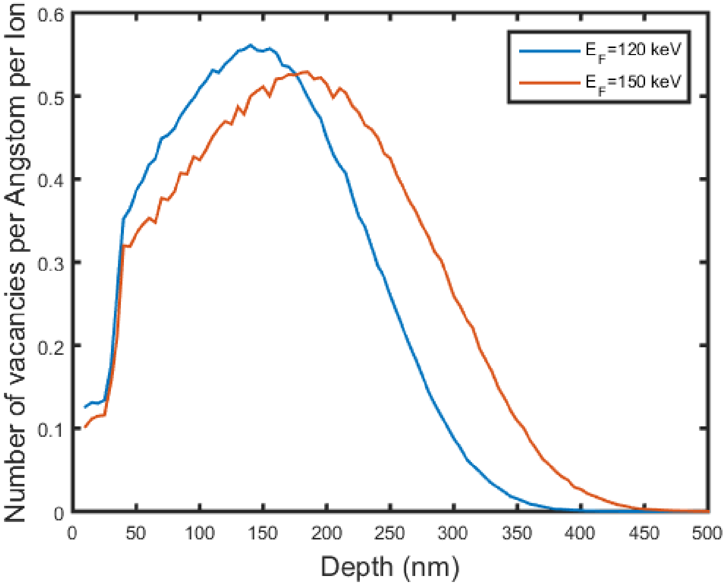

Figure 69: Vacancy distribution calculated by SRIM[36] after an implantation of fluorine in germanium at 120 keV and 150 keV, through a 30 nm layer of oxide. Most of the implantation damage is between the surface and the implantation peak.

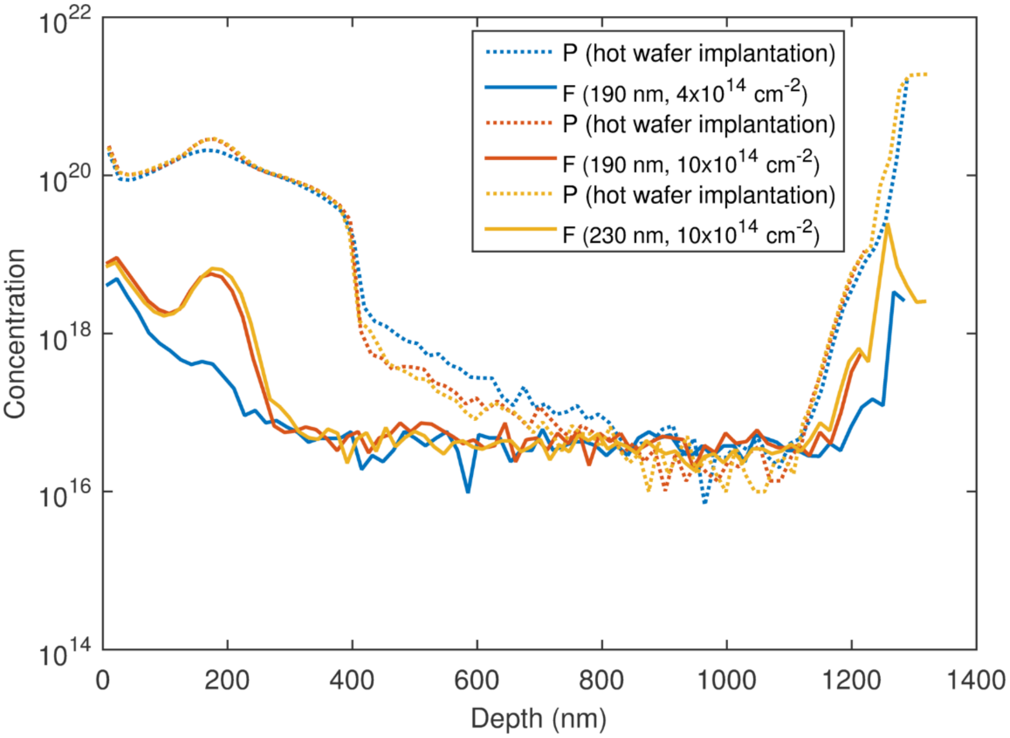

Figure 70: P and F profiles after the final 2 s 600 °C RTA on "hot wafer" implanted samples with different doses and energy of fluorine (pre-amorphized samples, E_P=200 keV D_P= 5x10^{15} cm^{-2}). There is a large concentration of fluorine at the implantation peak for the highest doses.

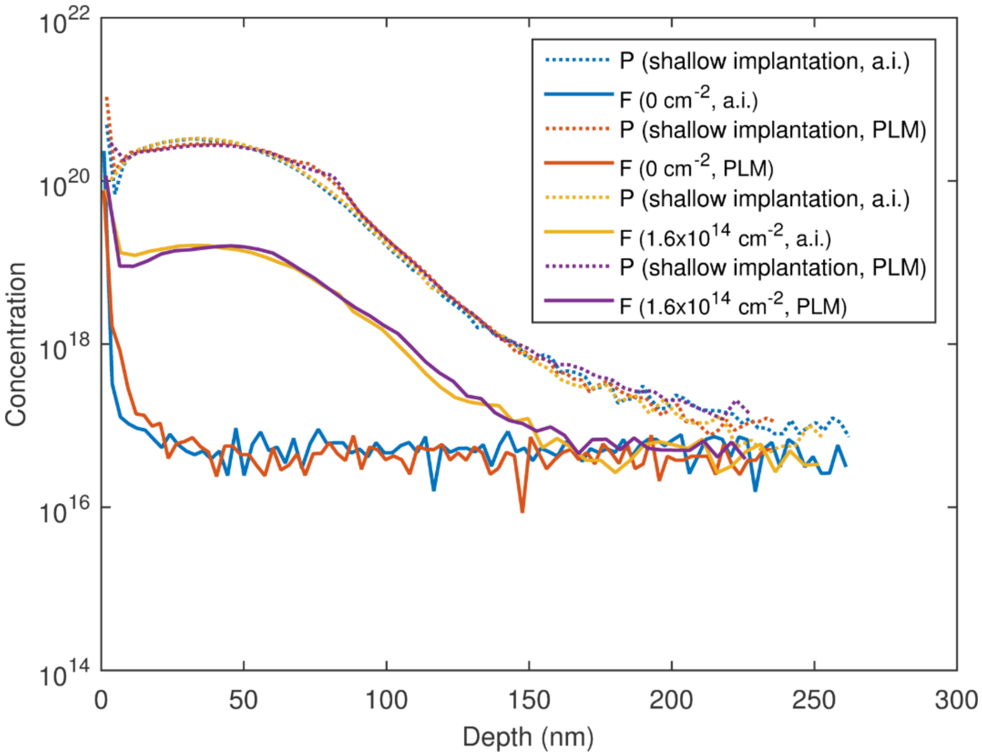

Figure 71: P and F profiles in as-implanted and after PLM (0.25 J.cm^{-2}) on shallow implantation samples (E_P=40 keV D_P= 2x10^{15} cm^{-2} E_F= 23 keV D_F=1.6x10^{14} cm^{-2}). The retention of fluorine is 100%.

d) P profile

In non-laser annealed samples, the different techniques to retain fluorine increases the thermal budget of the process. Compared to a normal implantation, an intertwined implantation requires as many RTAs as sub-amorphization implants need, while a hot wafer implantation requires keeping the sample at 200°C for extended periods of time. As a result, the P profiles resulting from these non-traditional implantations are broader than those of P-only implantations. As shown in Figure 68, the “hot wafer” phosphorus profile is similar to the “control” profile; a few nanometers broader, with a smaller concentration of phosphorus. This is in stark contrast with the intertwined sample which shows much more spread and the “box-like” phosphorus profile typical of concentration dependent diffusion[77], [103]. In this case, the low concentration of fluorine is not enough to passivate the vacancies and prevent the diffusion of the phosphorus induced by the increase of thermal budget. However, when more fluorine is present in the sample, the diffusion of phosphorus can be successfully reduced. A graph of the phosphorus and fluorine concentrations in a control wafer, a “hot implantation” wafer with a low fluorine dose and a “hot implantation” wafer with a high fluorine dose is shown in Figure 72. While the P profile is broader in the sample with the low dose of fluorine, the peak concentration of phosphorus is higher in the third sample than in the control sample in the region containing the most fluorine. Fluorine can slow down the diffusion of phosphorus, even when the fluorine to phosphorus ratio is 1 to 50.

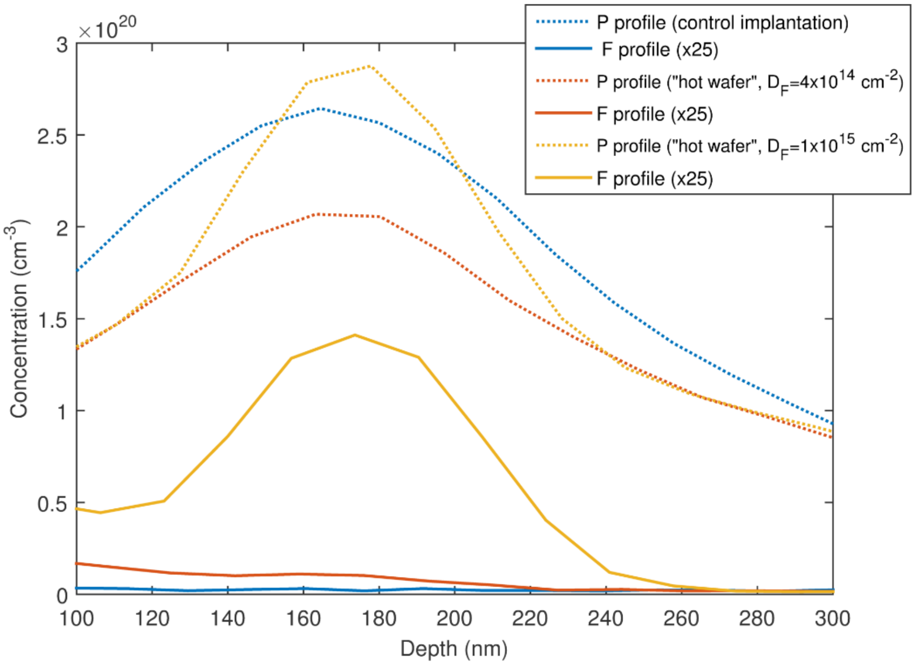

Figure 72: P and F profiles in different "hot wafer" implantations (pre-amorphized sample, E_P*=200 keV* D_P*= 5x10*^{15} *cm*$^{-2}$ E_F*= 120 keV). The sample with a significant concentration of fluorine also displays a pinning of phosphorus.*

e) Donor activation

Spreading Resistance Analysis (SRA) was performed complementing the SIMS measurement data, in order to estimate the level of activation of the phosphorus dopant. Figure 73 shows the free carrier concentrations in a control wafer, an intertwined wafer and a hot implantation wafer, whose SIMS profiles were shown in Figure 68. The activation levels of the control and hot implantation sample are similar in the highly doped region: there is not enough fluorine retained to passivate the vacancies, consistently with the model we developed in section II. e) of this chapter. However, the hot implantation wafer profile has a trailing tail between 400 nm and 700 nm and is therefore less abrupt than the control. This is in part due to a higher concentration of phosphorus due to the higher thermal budget of the hot wafer implantation, but is also due to a higher activation of the phosphorus (which can be measured by taking the ratio of free carrier concentration divided by chemical concentration of donor). The intertwined sample has a wider profile than the other two, due to the spread of phosphorus induced by the multiple anneals it has undergone, consistently with the SIMS profile. Comparing the SIMS to the SRA profile of the intertwined sample shows a counterintuitive effect. The maximal Phosphorus concentration is of $9x10^{19}$ cm^{-3} at 190 nm. Past this depth, it decreases slowly up to 400 nm ($n_P=5.5x10^{19}$ cm^{-3}) where it falls abruptly. However, at the same depths, the free carrier concentration increases from $4x10^{19}$ cm^{-3} to $7x10^{19}$ cm^{-3}. From 200 to 400 nm, the measured free carrier concentration is higher than the measured chemical concentration of donors due to experimental incertitude, and this shows that the activation of phosphorus in this region is close to 100%. This high activation is probably not due to a direct effect of fluorine, because its concentration is too low, but rather due to the defect concentration, which is smaller past the implantation peak. There are less vacancies in the 200 nm to 400 nm deep region, and therefore less vacancy-phosphorus compensating centers. It is unclear whether the presence of fluorine exacerbates this effect by pinning the vacancies introduced by the implantation in place, thus preventing their diffusion to the less defective deeper regions.

Besides the implanted region, the free carrier concentration deeper in the germanium layer is different in the control versus the fluorine containing samples. The base layer of epitaxial germanium is p-type at a level of 10^{15} cm^{-5}, due to electrically active defects. In the fluorine containing samples, the free hole concentration is smaller: fluorine is effective at passivating low concentrations of defects. The concentration of fluorine is below SIMS sensitivity, but there is no doubt that fluorine is present because high concentrations of fluorine are measured in the highly defective buffer layer at the germanium and silicon interface (similarly to what is shown in Figure 75), which means that, within our thermal budget, fluorine can diffuse in the entire germanium layer. Contrary to a traditional case of diffusion where a profile slowly broadens over time, fluorine diffuses quickly enough that its distribution is not determined by kinetics, but by its low solubility in germanium and the minimization of its free energy by associating with defect. Fluorine exhibits both a low solubility and a high diffusivity.

Hall effect was used to measure the electron mobility in the implanted layer. The samples that were RTAed all have a mobility in the 240 $cm^2.V^{-1}.s^{-1}$ to 280 $cm^2.V^{-1}.s^{-1}$, with a lower mobility as the free carrier concentration increases, consistently to the trend observed in germanium[122]. The conductivity of the samples was 5% to 10% higher in the wafers that were pre-amorphized. In the case of the PLM samples, Hall effect was also performed to assess what energy per pulse yields the lowest resistivity. Three energies were tested: 0.25 $J.cm^{-2}$, 0.5 $J.cm^{-2}$ and 0.8 $J.cm^{-2}$. The highest conductivity was observed for the lowest energy pulses in all the samples. The was no significant difference of conductivity in the layer for the different doses of fluorine, which were tested up to $3.2x10^{14}$ cm^{-2} (a peak concentration of $5x10^{19}$ cm^{-3}). Figure 74 shows the SRA and SIMS profiles of a control and a fluorine containing sample, both after a PLM of 0.25 $J.cm^{-2}$, which melts the first 120 nm of the germanium layer. Despite the similarity of phosphorus profile, the free electron distributions are different. The activation of phosphorus close to the surface is higher in the fluorine containing sample. This might be due to a stabilization of the surface by fluorine, and is consistent with reports that ablation was reduced and the surface smoother after PLM in a fluorine containing sample, with respect to a control fluorine-less sample. Because the depth accuracy of SRA is lower in regions were the doping changes abruptly, it is unclear whether the difference of SRA between the two profiles between 80 nm and 100 nm is due error in the depth measurement, or if it is real. In the latter case, it might be due to the interaction of fluorine with the solidification front at the beginning of the recrystallization of the sample.

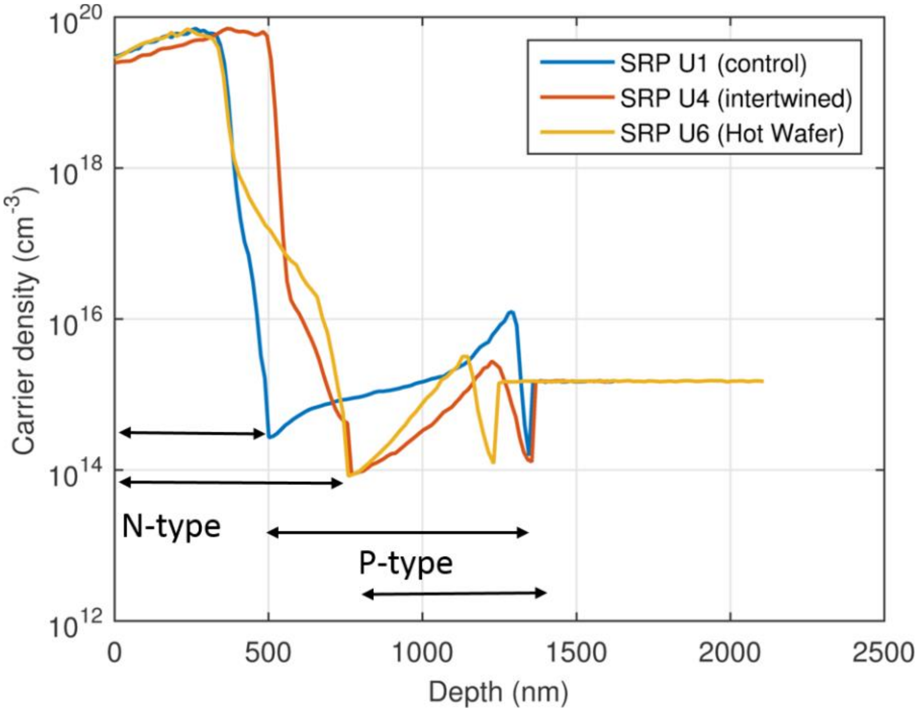

Figure 73: SRA profiles after the final 2 s 600 °C RTA of a "control", "intertwined" and "hot wafer" implantation (pre-amorphized samples, E_P=200 keV D_P= 5x10^{15} cm^{-2} E_F= 120 keV D_F=4x10^{14} cm^{-2}). The base layer is p-type. The discontinuity at 1300 nm is due to the Si/Ge interface. Note that the hot wafer implant was done in a thinner Ge layer.

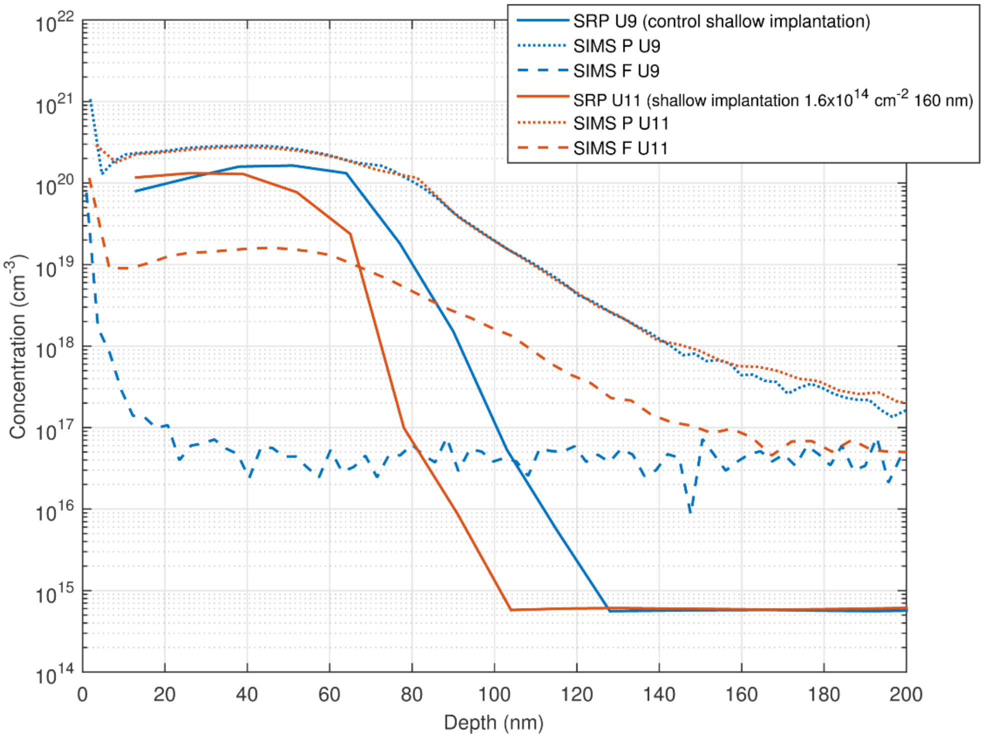

Figure 74: P and F SIMS profiles and SRA free carrier concentration after PLM (0.25 J.cm^{-2}) on shallow implantation samples (E_P=40 keV D_P= 2x10^{15} cm^{-2} E_F= 23 keV D_F=1.6x10^{14} cm^{-2}).

f) Implantation in ON$^+$ implanted samples

In order to investigate whether phosphorus (and not just the implantation damages induced by the P implantation) had an impact on the F profile, we have done similar implantations ("intertwined" and "hot wafer") in which a dimer of oxygen and nitrogen was implanted instead of phosphorus. The dimer was chosen because its mass approaches this of phosphorus and should therefore provide similar implantation damage. The dimers were implanted in a self-amorphized epi-layer of germanium, at an energy of 200 keV and a dose of 5x10^{15} cm^{-3}. After an RTA was performed to recover crystallinity, fluorine was implanted in the sample at an energy of 120 keV and for a total dose of 2x10^{14} cm^{-2} (by steps of 5x10^{13} cm^{-3} in the intertwined case). The SIMS fluorine profile of the different sample before and after a final RTA is provided in Figure 75. Contrary to the case of the phosphorus implanted samples, the fluorine retention after annealing is high, 52% for the intertwined strategy and 15% for the hot wafer implantation. This high retention is a sign that the defect complex that contain oxygen or nitrogen are more stable than these with phosphorus (less are annealed during the SPE) and/or that fluorine binds more readily with defect clusters containing oxygen or nitrogen.

Moreover, comparing the as implanted and after annealing profiles, some fluorine outgasses during the RTA, as expected, and the concentration of halogen in the implanted region gets lower. However, the concentration of fluorine in the highly dislocated buffer layer at the silicon/germanium interface increases, while the concentration remains below the sensitivity level in the less defective zone between the buffer and the implantation peak (consistently with the low solubility of fluorine in defect free material). This means that, given enough thermal budget, fluorine can experience long range (micrometric) diffusion and stabilization were point defects are aplenty. This long range diffusion also confirms the high diffusivity of fluorine in germanium, of at least 10^{-10} $cm^{-2}.s^{-1}$ (1 µm covered in 2 seconds) at 600°C, a figure consistent with the estimates made in section II. d) of this chapter, of 10^{-15} $cm^{-2}.s^{-1}$ at 400°C and 10^{-13} $cm^{-2}.s^{-1}$ at 500°C. At this RTA temperature (600°C), the fluorine distribution is not diffusion limited but instead controlled by the minimization of free energy at defect sites. It also consistent with the F profiles in the phosphorus co-implanted samples (Figure 68), which were asymmetric and displayed a higher fluorine concentration in more defective region closer to the surface.

The difference of fluorine retention between the two non-amorphizing implantation strategies is due to the number of defects generated by each method. In Figure 76, the F profiles of as-implanted and annealed samples are super-imposed on a cross-sectional TEM micrograph. The as-implanted concentrations are similar, but the difference of fluorine profiles after annealing is due to the visibly higher concentration of extended point defects in the intertwined sample. This further demonstrates that the solubility of fluorine in crystalline germanium is mediated by point defects.

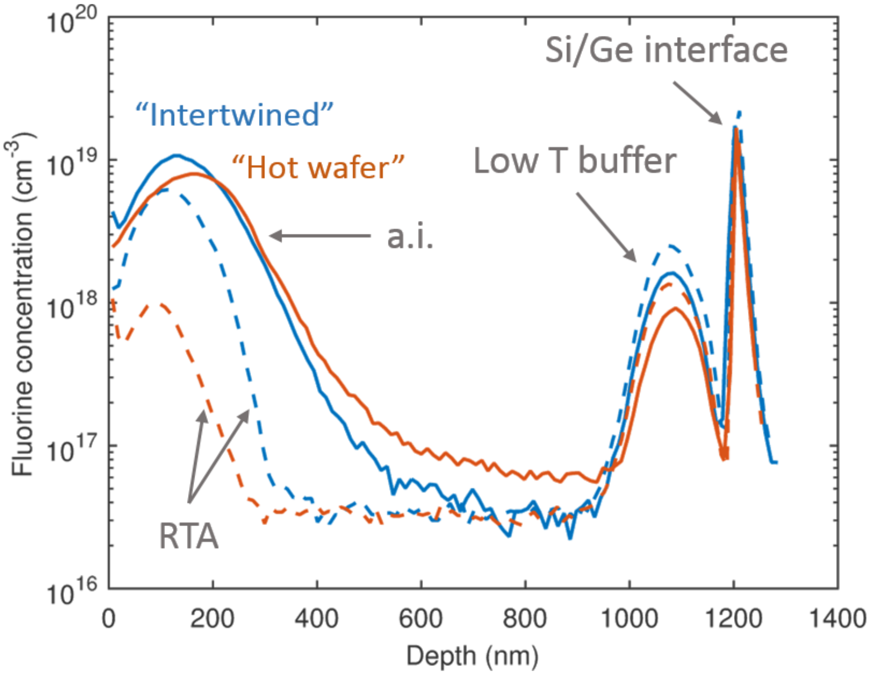

Figure 75: F profile after a co-implantation of ON dimers and fluorine (E_{ON}=200 keV D_P= $2x10^{15}$ cm^{-2} E_F= 120 keV D_F=$2x10^{14}$ cm^{-2}).

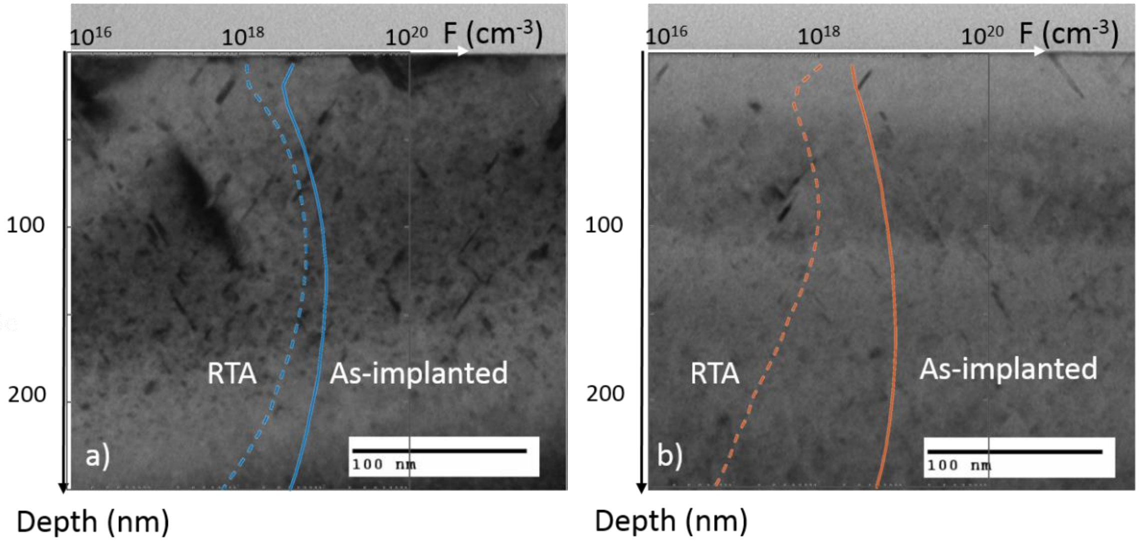

Figure 76: Superposition of F profiles before and after RTA on a TEM micrograph of an as-implanted a) "intertwined" sample and b) "hot wafer" sample that underwent a ON+F implantation (E_{ON}*=200 keV* D_P*= 2x*10^{15} *cm*$^{-2}$ E_F*= 120 keV* D_F*=2x*10^{14} *cm*$^{-2}$*). The fluorine retention is higher in the "intertwined" sample, which has the highest concentration of defects.*

IV. Summary

The use of fluorine as a bond terminator to passivate vacancies in highly doped germanium is an interesting defect engineering strategy. However, the interaction between the fluorine and the amorphous/crystalline interface during the solid phase epitaxy that follows a high dose implant drives most of the fluorine out of the sample. To avoid this issue, we have proposed alternative methods. On the one hand, a two-step implantation can be implemented: an RTA can be done after the phosphorus implantation to recover the crystallinity of the layer, and then fluorine can be implanted, in a way that does not amorphize the germanium (either by the "intertwined" or the "hot wafer" scheme), in order to avoid the SPE all together. On the other hand, ultra-fast annealing such as PLM can be used. In this case, the SPE kinetics is so fast that there is no out-diffusion. The retention of fluorine then is 100%, but at the dose of fluorine that we used, we did not detect a major difference of activation between a control sample and one with fluorine. The retention is much lower in the samples on which was performed a two-step implantation and which underwent some RTA, because the diffusivity of fluorine is high, in the 10^{-10} $cm^{-2}.s^{-1}$ at 600°C, while its solubility in crystalline germanium is mediated by point defects and therefore low in good quality material. For these samples, we have shown that the fluorine profile is determined by the implantation damage distribution, and that fluorine does not interact with phosphorus. As a result, the more fluorine we want to introduce, the more implantation damage is needed, which is counter-productive. Therefore, a better way to use the electro-negativity of fluorine to passivate point defects is to uncouple the implantation damage from the active area where fluorine is desired. This is possible due to the high diffusivity of fluorine and its affinity for point defects: the halogen will go to the defective areas, regardless of where it is implanted. This approach can be especially appropriate to passivate defects in lower concentrations and or spread through the sample, such as dislocations and growth defects.

Chapter 8. Conclusion

I. Summary

The goal of this doctoral work was to remedy the lack of understanding on the point defects of germanium and to use this newly acquired knowledge to design better devices. We have extensively relied on Deep-Level Transient Spectroscopy to measure the electronic properties of point defects. We have used gamma rays, alpha particles and neutrons to introduce different point defects in various form of germanium, from Czochralski bulk germanium to fully processed and integrated in a device Germanium on silicon. The result is a survey of the states populating the otherwise forbidden bandgap of the group four element.

In chapter 3, we have analyzed Czochralski-grown bulk n-type germanium, irradiated by ^{60}Co gamma ray. By a combination of high temperature annealing, cryogenic irradiation and introduction rate considerations, we were able to characterize multiple defects. First, the double acceptor state of a vacancy-donor complex (also called E-center), which is the only vacancy containing defect in such a n-type sample. We showed that the three other defects are all interstitials, including one di-interstitial. One of them was unstable at room temperature, and it is the association of two of them that yields the di-interstitial defect. Above 100°C, this di-interstitial splits itself to generate two stable single-interstitial point defects [16].

In chapter 4, we have used the same pristine n-type material but irradiated it with alpha particles and neutrons. These particles interact directly by nuclear force with germanium in the lattice and, instead of only generating single displacement, can produce collision cascades. As a result, in addition to the defects observed after a gamma ray irradiation, the alpha particle and neutron irradiated samples contain more complex defects, some containing two or more interstitials and vacancies. By investigating the dependence of their introduction rate on the dose and nature of the particle, we have been able to sort out the primary defects from those that form by diffusion and association, and to recognize the defects that contain interstitials and these that contain vacancies. In particular, we could identify a triple interstitial defect. Furthermore, in addition to the generation of more complex defects, the irradiation by alpha particles and neutrons has another consequence: the defects are not uniformly distributed, but instead concentrated close to one another inside defect clusters generated during collision cascades. This proximity of the defects has consequences on their properties: their annealing is changed and their cross-sections are affected by the capture of charges by neighboring defects.

In chapter 5, we have investigated the defects present after a ^{60}Co gamma irradiation of commercially available Ge-on-Si photodetectors. This was an opportunity to study multiple subjects: p-type germanium, the difference between bulk and thin film germanium and the influence of point defects on the macroscopic performance of a device. In this section, we have shown that point defects in Ge-on-Si layers decorate the dislocations, which are present to accommodate the lattice mismatch between silicon and germanium. This association with the dislocation affects the capture cross-section of the traps and results in a “logarithmic” capture process. Using injection DLTS, we were able to probe both side of the bandgap of the germanium and also could measure defects whose electronic signature matches those of defects we observed in bulk n-type germanium. Furthermore, the dislocations are the major cause of leakage current in these devices, making them radiation hard even for doses of gamma rays in the 100 Mrad.

The study of point defects is a fundamental science, and leveraging this knowledge is critical to developing better devices and insuring they work optimally during their lifetime. This is defect engineering. In chapter 6, we have used the extensive knowledge existing on the point defects in silicon to find the reason why the charge transfer inefficiency of the CCDs on-board the *Chandra* spatial telescope increased significantly first after launch and then after an annealing was performed to tentatively remove point defects. We have determined that the mechanism that was the cause of this performance degradation is the association of a carbon interstitial with an impurity. Interstitials were introduced by a soft proton irradiation during the launch. These interstitials then diffused to carbon atoms, forming carbon interstitials. Finally, the annealing activated the diffusion of the carbon interstitials to form a much more active point defect by reacting with another impurity. In addition to the identification of this mechanism, we have proposed upper bounds for the annealing temperature and durations that can be used to prevent such a phenomenon to happen again.

In chapter 7, we have investigated how fluorine can be used as a bond terminator to passivate the vacancies that prevent a full activation of donors in highly doped germanium. We have confirmed that a traditional co-implantation of a donor and fluorine is bound to fail, because the fluorine segregates at the amorphous/crystalline interface and outgasses too quickly during the Solid Phase Epitaxy (SPE) phase, which is necessary for the sample to recover crystallinity after the implantation. We have developed strategies to get around this limitation: either using ultra-fast laser processing or implementing a two-step implantation, in which the crystallinity of the sample is recovered after the donor implantation, prior to a non-amorphizing implantation of fluorine, to avoid the SPE. We have investigated different non-amorphizing implant methods, by implanting in a hot wafer and by alternating annealing and implantation of low doses of fluorine. We could improve the retention of fluorine, but at the price of a higher implantation damage density, as we showed that the solubility of crystalline germanium is low and mediated by point defects. We also noticed that fluorine can undergo long distance diffusion and passivate point defects and dislocations in regions far from the implantation peak.

II. Future work

Our objective in this project was double: map the point defects in germanium and use this knowledge to engineer better devices. The “mapping” work should be continued by increasing our measuring capabilities. In our study of n-type CZ-germanium, we only used Schottky junctions and were thus restricted to studying the upper side of the bandgap. The other side could be investigated either by using PN junctions instead of Schottky junctions and pulse injection DLTS (which is an approach that we have leveraged with the germanium pin-photodetectors) or by implementing optically pulsed DLTS. The ability to measure defects on both sides of the bandgap would greatly improve the quality of the defect mapping. Furthermore, this capability would allow for the measurement of the capture cross-section for electrons and holes of the same defect state. This would help developing more accurate models to connect the point defect population to the macroscopic properties of a device, such as the leakage current.

Another natural continuation of this work is to leverage the point defect map by using the very defects in devices. For instance, because all the defects have a precise position in the bandgap, sub-bandgap photodetector could be developed that uses a band-to-defect light absorption mechanism to be sensitive to a chosen wavelength[123]. In addition, our knowledge of point defect introduction rates, formation mechanisms and annealing behaviors should be used to make a connection between processing and defect generation, in order to prevent the formation or remove the most active defects during the fabrication of devices. To this end, it would be interesting to investigate how fluorine interacts with processing defects and dislocations, using the high diffusivity of fluorine to uncouple the location of the implantation damage from where we want the fluorine to diffuse.

Bibliography

[1] R. E. Camacho-Aguilera, Y. Cai, N. Patel, J. T. Bessette, M. Romagnoli, L. C. Kimerling, and J. Michel, "An electrically pumped germanium laser," *Opt. Express*, vol. 20, no. 10, pp. 11316–11320, May 2012.

[2] R. Koerner, M. Oehme, M. Gollhofer, M. Schmid, K. Kostecki, S. Bechler, D. Widmann, E. Kasper, and J. Schulze, "Electrically pumped lasing from Ge Fabry-Perot resonators on Si," *Opt. Express*, vol. 23, no. 11, p. 14815, Jun. 2015.

[3] D. Ahn, C. Hong, J. Liu, W. Giziewicz, M. Beals, L. C. Kimerling, J. Michel, J. Chen, and F. X. Kärtner, "High performance, waveguide integrated Ge photodetectors," *Opt. Express*, vol. 15, no. 7, pp. 3916–3921, Apr. 2007.

[4] J. Michel, J. Liu, and L. C. Kimerling, "High-performance Ge-on-Si photodetectors," *Nat. Photonics*, vol. 4, no. 8, pp. 527–534, Aug. 2010.

[5] C. T. DeRose, D. C. Trotter, W. A. Zortman, A. L. Starbuck, M. Fisher, M. R. Watts, and P. S. Davids, "Ultra compact 45 GHz CMOS compatible Germanium waveguide photodiode with low dark current," *Opt. Express*, vol. 19, no. 25, p. 24897, Dec. 2011.

[6] J. E. Roth, O. Fidaner, R. K. Schaevitz, Y.-H. Kuo, T. I. Kamins, J. S. Harris, and D. A. Miller, "Optical modulator on silicon employing germanium quantum wells," *Opt. Express*, vol. 15, no. 9, p. 5851, 2007.

[7] J. Liu, M. Beals, A. Pomerene, S. Bernardis, R. Sun, J. Cheng, L. C. Kimerling, and J. Michel, "Waveguide-integrated, ultralow-energy GeSi electro-absorption modulators," *Nat. Photonics*, vol. 2, no. 7, pp. 433–437, Jul. 2008.

[8] J. L. Bowman, W. C. Myers, and R. S. Ricks, "Snap-off diode containing recombination impurities," US3337779 A, 22-Aug-1967.

[9] "Band structure and carrier concentration of Germanium (Ge)." [Online]. Available: http://www.ioffe.ru/SVA/NSM/Semicond/Ge/bandstr.html. [Accessed: 10-May-2016].

[10] E. Holmström, K. Nordlund, and A. Kuronen, "Threshold defect production in germanium determined by density functional theory molecular dynamics simulations," *Phys. Scr.*, vol. 81, no. 3, p. 35601, 2010.

[11] V. Emtsev, "Point defects in germanium: Reliable and questionable data in radiation experiments," *Mater. Sci. Semicond. Process.*, vol. 9, no. 4–5, pp. 580–588, Aug. 2006.

[12] A. Mesli, L. Dobaczewski, K. B. Nielsen, V. Kolkovsky, M. C. Petersen, and A. N. Larsen, "Low-temperature irradiation-induced defects in germanium: In situ analysis," *Phys. Rev. B*, vol. 78, no. 16, p. 165202, Oct. 2008.

[13] G. H. Kinchin and R. S. Pease, "The Displacement of Atoms in Solids by Radiation," *Rep. Prog. Phys.*, vol. 18, no. 1, p. 1, 1955.

[14] L. C. Kimerling, "Compensation of germanium by radiation defects.," Thesis, Massachusetts Institute of Technology, 1969.

[15] G L Miller, D V Lang, and L. C. Kimerling, "Capacitance Transient Spectroscopy," *Annu. Rev. Mater. Sci.*, vol. 7, no. 1, pp. 377–448, 1977.

[16] N. S. Patel, C. Monmeyran, A. Agarwal, and L. C. Kimerling, "Point defect states in Sb-doped germanium," *J. Appl. Phys.*, vol. 118, no. 15, p. 155702, Oct. 2015.

[17] D. L. Trueblood, "Electron Paramagnetic Resonance in Electron-Irradiated Germanium," *Phys. Rev.*, vol. 161, no. 3, pp. 828–833, Sep. 1967.

[18] R. J. Elliott, "Theory of the Effect of Spin-Orbit Coupling on Magnetic Resonance in Some Semiconductors," *Phys. Rev.*, vol. 96, no. 2, pp. 266–279, Oct. 1954.

[19] G. W. Ludwig and H. H. Woodbury, "Electron Spin Resonance in Semiconductors," in *Solid State Physics*, vol. 13, 1962.

[20] A. Mesli and A. Nylandsted Larsen, "Irradiation induced defects in Si1−xGex: The effect of alloying," *Nucl. Instrum. Methods Phys. Res. Sect. B Beam Interact. Mater. At.*, vol. 211, no. 1, pp. 80–90, Sep. 2003.

[21] N. Fukuoka and H. Saito, "Radiation Defects in n-Type Germanium Studied by Deep Level Transient Spectroscopy," *Jpn. J. Appl. Phys.*, vol. 20, no. 7, p. L519, Jul. 1981.

[22] F. Poulin and J. C. Bourgoin, "Characteristics of the electron traps produced by electron irradiation in n-type germanium," *Phys. Rev. B*, vol. 26, no. 12, pp. 6788–6794, Dec. 1982.

[23] P. M. Mooney, F. Poulin, and J. C. Bourgoin, "Annealing of electron-induced defects in n-type germanium," *Phys. Rev. B*, vol. 28, no. 6, pp. 3372–3377, Sep. 1983.

[24] V. Nagesh and J. W. Farmer, "Study of irradiation-induced defects in germanium," *J. Appl. Phys.*, vol. 63, no. 5, pp. 1549–1553, Mar. 1988.

[25] J. Fage-Pedersen, A. N. Larsen, and A. Mesli, "Irradiation-induced defects in Ge studied by transient spectroscopies," *Phys. Rev. B*, vol. 62, no. 15, pp. 10116–10125, Oct. 2000.

[26] V. P. Markevich, A. R. Peaker, V. V. Litvinov, V. V. Emtsev, and L. I. Murin, "Electronic properties of antimony-vacancy complex in Ge crystals," *J. Appl. Phys.*, vol. 95, no. 8, pp. 4078–4083, Apr. 2004.

[27] F. D. Auret, W. E. Meyer, S. Coelho, and M. Hayes, "Electrical characterization of defects introduced during electron beam deposition of Pd Schottky contacts on n-type Ge," *Appl. Phys. Lett.*, vol. 88, no. 24, p. 242110, Jun. 2006.

[28] V. P. Markevich, I. D. Hawkins, A. R. Peaker, K. V. Emtsev, V. V. Emtsev, V. V. Litvinov, L. I. Murin, and L. Dobaczewski, "Vacancy-group-V-impurity atom pairs in Ge crystals doped with P, As, Sb, and Bi," *Phys. Rev. B*, vol. 70, no. 23, p. 235213, Dec. 2004.

[29] C. H. Henry and D. V. Lang, "Nonradiative capture and recombination by multiphonon emission in GaAs and GaP," *Phys. Rev. B*, vol. 15, no. 2, pp. 989–1016, Jan. 1977.

[30] V. Kolkovsky, M. C. Petersen, A. Mesli, J. Van Gheluwe, P. Clauws, and A. N. Larsen, "Gallium interstitial in irradiated germanium: Deep level transient spectroscopy," *Phys. Rev. B*, vol. 78, no. 23, p. 233201, Dec. 2008.

[31] S. Brotzmann and H. Bracht, "Intrinsic and extrinsic diffusion of phosphorus, arsenic, and antimony in germanium," *J. Appl. Phys.*, vol. 103, no. 3, p. 33508, Feb. 2008.

[32] J. R. Weber, A. Janotti, and C. G. Van de Walle, "Dangling bonds and vacancies in germanium," *Phys. Rev. B*, vol. 87, no. 3, p. 35203, Jan. 2013.

[33] K. T. Roro, P. J. Janse van Rensburg, F. D. Auret, and S. Coelho, "Effect of alpha-particle irradiation on the electrical properties of n-type Ge," *Phys. B Condens. Matter*, vol. 404, no. 22, pp. 4496–4498, Dec. 2009.

[34] A. Carvalho, R. Jones, C. Janke, J. P. Goss, P. R. Briddon, J. Coutinho, and S. Öberg, "Self-Interstitial in Germanium," *Phys. Rev. Lett.*, vol. 99, no. 17, p. 175502, Oct. 2007.

[35] H. C. Schweinler, "Some Consequences of Thermal Neutron Capture in Silicon and Germanium," *J. Appl. Phys.*, vol. 30, no. 8, pp. 1125–1126, Aug. 1959.

[36] J. F. Ziegler, M. D. Ziegler, and J. P. Biersack, "SRIM – The stopping and range of ions in matter (2010)," *Nucl. Instrum. Methods Phys. Res. Sect. B Beam Interact. Mater. At.*, vol. 268, no. 11–12, pp. 1818–1823, Jun. 2010.

[37] D. Lister and A. B. Smith, "Fast-Neutron Scattering from Germanium," *Phys. Rev.*, vol. 183, no. 4, pp. 954–963, Jul. 1969.

[38] N. US Department of Commerce, "NIST Stopping-Power and Range Tables: Electrons, Protons, Helium Ions." [Online]. Available: http://www.nist.gov/pml/data/star/. [Accessed: 19-Jul-2016].

[39] V. Nagesh and J. W. Farmer, "Study of irradiation-induced defects in germanium," *J. Appl. Phys.*, vol. 63, no. 5, pp. 1549–1553, Mar. 1988.

[40] I. Capan, B. Pivac, I. D. Hawkins, V. P. Markevich, A. R. Peaker, L. Dobaczewski, and R. Jacimovic, “Neutron-irradiation-induced defects in germanium: A Laplace deep level transient spectroscopy study,” *Vacuum*, vol. 84, no. 1, pp. 32–36, Aug. 2009.

[41] V. P. Markevich, S. Bernardini, I. D. Hawkins, A. R. Peaker, V. Kolkovsky, A. Nylandsted Larsen, and L. Dobaczewski, “Electrically active defects induced by hydrogen and helium implantations in Ge,” *Mater. Sci. Semicond. Process.*, vol. 11, no. 5–6, pp. 354–359, Oct. 2008.

[42] F. Poulin and J. C. Bourgoin, “Threshold energy for atomic displacement in electron irradiated germanium,” *Rev. Phys. Appliquée*, vol. 15, no. 1, pp. 15–19, 1980.

[43] J. Fage-Pedersen, A. N. Larsen, and A. Mesli, “Irradiation-induced defects in Ge studied by transient spectroscopies,” *Phys. Rev. B*, vol. 62, no. 15, pp. 10116–10125, Oct. 2000.

[44] V. Kolkovsky, M. C. Petersen, and A. N. Larsen, “Alpha-particle irradiation-induced defects in n-type germanium,” *Appl. Phys. Lett.*, vol. 90, no. 11, p. 112110, Mar. 2007.

[45] K. T. Roro, P. J. Janse van Rensburg, F. D. Auret, and S. Coelho, “Effect of alpha-particle irradiation on the electrical properties of n-type Ge,” *Phys. B Condens. Matter*, vol. 404, no. 22, pp. 4496–4498, Dec. 2009.

[46] J. Coutinho, V. J. B. Torres, R. Jones, A. Carvalho, S. Öberg, and P. R. Briddon, “Calculation of deep carrier traps in a divacancy in germanium crystals,” *Appl. Phys. Lett.*, vol. 88, no. 9, p. 91919, Feb. 2006.

[47] V. Kolkovsky, M. Christian Petersen, A. Nylandsted Larsen, and A. Mesli, “No trace of divacancies at room temperature in germanium,” *Mater. Sci. Semicond. Process.*, vol. 11, no. 5–6, pp. 336–339, Oct. 2008.

[48] L. C. Kimerling and J. R. Patel, “Defect states associated with dislocations in silicon,” *Appl. Phys. Lett.*, vol. 34, no. 1, pp. 73–75, Jan. 1979.

[49] T. Figielski, “Electron emission from extended defects: DLTS signal in case of dislocation traps,” *Phys. Status Solidi A*, vol. 121, no. 1, pp. 187–193, Sep. 1990.

[50] H.-C. Luan, D. R. Lim, K. K. Lee, K. M. Chen, J. G. Sandland, K. Wada, and L. C. Kimerling, “High-quality Ge epilayers on Si with low threading-dislocation densities,” *Appl. Phys. Lett.*, vol. 75, no. 19, pp. 2909–2911, Nov. 1999.

[51] P. Omling, L. Samuelson, and H. G. Grimmeiss, “Deep level transient spectroscopy evaluation of nonexponential transients in semiconductor alloys,” *J. Appl. Phys.*, vol. 54, no. 9, pp. 5117–5122, Sep. 1983.

[52] P. Omling, E. R. Weber, L. Montelius, H. Alexander, and J. Michel, “Electrical properties of dislocations and point defects in plastically deformed silicon,” *Phys. Rev. B*, vol. 32, no. 10, pp. 6571–6581, Nov. 1985.

[53] V. P. Markevich, A. R. Peaker, V. V. Litvinov, V. V. Emtsev, and L. I. Murin, “Electronic properties of antimony-vacancy complex in Ge crystals,” *J. Appl. Phys.*, vol. 95, no. 8, pp. 4078–4083, Apr. 2004.

[54] C. E. Lindberg, J. L. Hansen, P. Bomholt, A. Mesli, K. B. Nielsen, A. N. Larsen, and L. Dobaczewski, “The antimony-vacancy defect in p-type germanium,” *Appl. Phys. Lett.*, vol. 87, no. 17, p. 172103, Oct. 2005.

[55] N. Fukuoka and H. Saito, “Radiation Defects in n-Type Germanium Studied by Deep Level Transient Spectroscopy,” *Jpn. J. Appl. Phys.*, vol. 20, no. 7, pp. L519–L522, Jul. 1981.

[56] J. Coutinho, S. Öberg, V. J. B. Torres, M. Barroso, R. Jones, and P. R. Briddon, “Donor-vacancy complexes in Ge: Cluster and supercell calculations,” *Phys. Rev. B*, vol. 73, no. 23, p. 235213, Jun. 2006.

[57] M. Bautz, G. Prigozhin, S. Kissel, B. LaMarr, C. Grant, and S. Brown, “Anomalous annealing of a high-resistivity CCD irradiated at low temperature,” *IEEE Trans. Nucl. Sci.*, vol. 52, no. 2, pp. 519–526, Apr. 2005.

[58] C. E. Grant, B. LaMarr, G. Y. Prigozhin, S. E. Kissel, S. K. Brown, and M. W. Bautz, “Physics of reverse annealing in high-resistivity Chandra ACIS CCDs,” 2008, vol. 7021, pp. 702119-702119–9.

[59] B. E. Burke, J. A. Gregory, M. W. Bautz, G. Y. Prigozhin, S. E. Kissel, B. B. Kosicki, A. H. Loomis, and D. J. Young, “Soft-X-ray CCD imagers for AXAF,” *IEEE Trans. Electron Devices*, vol. 44, no. 10, pp. 1633–1642, Oct. 1997.

[60] R. A. Bredthauer, J. H. Pinter, J. R. Janesick, and L. B. Robinson, “Notch and large-area CCD imagers,” 1991, vol. 1447, pp. 310–315.

[61] W. F. Kosonocky, “Charge-coupled device channel structure,” US4667213 A, 19-May-1987.

[62] R. D. Nelson, “Potential troughs for charge transfer devices,” US4185292 A, 22-Jan-1980.

[63] G. Y. Prigozhin, S. E. Kissel, M. W. Bautz, C. Grant, B. LaMarr, R. F. Foster, and J. Ricker George R., “Characterization of the radiation damage in the Chandra x-ray CCDs,” 2000, vol. 4140, pp. 123–134.

[64] A. K. Tipping and R. C. Newman, “The diffusion coefficient of interstitial carbon in silicon,” *Semicond. Sci. Technol.*, vol. 2, no. 5, p. 315, 1987.

[65] M. Yoshida, E. Arai, H. Nakamura, and Y. Terunuma, “Excess vacancy generation mechanism at phosphorus diffusion into silicon,” *J. Appl. Phys.*, vol. 45, no. 4, pp. 1498–1506, Apr. 1974.

[66] L. F. Makarenko, M. Moll, F. P. Korshunov, and S. B. Lastovski, “Reactions of interstitial carbon with impurities in silicon particle detectors,” *J. Appl. Phys.*, vol. 101, no. 11, p. 113537, Jun. 2007.

[67] L. C. Kimerling, M. T. Asom, J. L. Benton, P. J. Drevinsky, and C. E. Caefer, “Interstitial defect reactions in silicon,” in *Materials Science Forum*, 1991, vol. 38, pp. 141–150.

[68] T. Hardy, R. Murowinski, and M. J. Deen, “Charge transfer efficiency in proton damaged CCD’s,” *IEEE Trans. Nucl. Sci.*, vol. 45, no. 2, pp. 154–163, Apr. 1998.

[69] E. Gurer, B. Benson, and G. Watkins, “Configurational Metastability of Carbon-Phosphorus Pair Defects in Silicon,” in *Proceedings of the 16th International Conference on Defects in Semiconductors, Pts 1-3*, vol. 83, G. Davies, G. G. Deleo, and M. Stavola, Eds. Stafa-Zurich: Trans Tech Publications Ltd, 1992, pp. 339–344.

[70] G. D. Watkins and J. W. Corbett, “Defects in Irradiated Silicon: Electron Paramagnetic Resonance and Electron-Nuclear Double Resonance of the Si-E Center,” *Phys. Rev.*, vol. 134, no. 5A, pp. A1359–A1377, Jun. 1964.

[71] M. Sirianni, M. Mutchler, R. Gilliland, J. Biretta, and R. Lucas, “Radiation Damage in Hubble Space Telescope Detectors,” in *2007 IEEE Radiation Effects Data Workshop*, 2007, vol. 0, pp. 9–15.

[72] R. A. Kimble, P. Goudfrooij, and R. L. Gilliland, “Radiation damage effects on the CCD detector of the space telescope imaging spectrograph,” 2000, vol. 4013, pp. 532–544.

[73] A. Waczynski, E. J. Polidan, P. W. Marshall, R. A. Reed, S. D. Johnson, R. J. Hill, G. S. Delo, E. J. Wassell, E. S. Cheng, and others, “A comparison of charge transfer efficiency measurement techniques on proton damaged n-channel CCDs for the Hubble Space Telescope wide-field camera 3,” *IEEE Trans. Nucl. Sci.*, vol. 48, no. 6, pp. 1807–1814, 2001.

[74] J. Holtzman, J. J. Hester, S. Casertano, J. T. Trauger, A. M. Watson, G. E. Ballester, C. J. Burrows, J. T. Clarke, D. Crisp, R. W. Evans, J. S. Gallagher, R. E. Griffiths, J. G. Hoessel, L. D. Matthews, J. R. Mould, P. A. Scowen, K. R. Stapelfeldt, and J. A. Westphal, “The Performance and Calibration of WFPC2 on the Hubble Space Telescope,” *Publ. Astron. Soc. Pac.*, vol. 107, no. 708, pp. 156–178, 1995.

[75] A. Holmes-Siedle, A. Holland, and S. Watts, “The impact of space protons on X-ray sensing with charge coupled devices (CCDs),” *IEEE Trans. Nucl. Sci.*, vol. 43, no. 6, pp. 2998–3004, Dec. 1996.

[76] A. Yamashita, T. Dotani, M. Bautz, G. Crew, H. Ezuka, K. Gendreau, T. Kotani, K. Mitsuda, C. Otani, A. Rasmussen, G. Ricker, and H. Tsunemi, “Radiation damage to charge coupled devices in the space environment,” *IEEE Trans. Nucl. Sci.*, vol. 44, no. 3, pp. 847–853, Jun. 1997.

[77] A. Satta, T. Janssens, T. Clarysse, E. Simoen, M. Meuris, A. Benedetti, I. Hoflijk, B. D. Jaeger, C. Demeurisse, and W. Vandervorst, “P implantation doping of Ge: Diffusion, activation, and recrystallization,” *J. Vac. Sci. Technol. B*, vol. 24, no. 1, pp. 494–498, Jan. 2006.

[78] M. Koike, Y. Kamata, T. Ino, D. Hagishima, K. Tatsumura, M. Koyama, and A. Nishiyama, “Diffusion and activation of n-type dopants in germanium,” *J. Appl. Phys.*, vol. 104, no. 2, p. 23523, Jul. 2008.

[79] J. Vanhellemont and E. Simoen, “On the diffusion and activation of n-type dopants in Ge,” *Mater. Sci. Semicond. Process.*, vol. 15, no. 6, pp. 642–655, Dec. 2012.

[80] J. Coutinho, V. J. B. Torres, S. Öberg, A. Carvalho, C. Janke, R. Jones, and P. R. Briddon, “Early stage donor-vacancy clusters in germanium,” *J. Mater. Sci. Mater. Electron.*, vol. 18, no. 7, pp. 769–773, Dec. 2006.

[81] A. Chroneos, R. W. Grimes, B. P. Uberuaga, S. Brotzmann, and H. Bracht, “Vacancy-arsenic clusters in germanium,” *Appl. Phys. Lett.*, vol. 91, no. 19, p. 192106, Nov. 2007.

[82] G. Capellini, W. M. Klesse, G. Mattoni, M. Y. Simmons, and G. Scappucci, “(Invited) Alternative High n-Type Doping Techniques in Germanium,” *ECS Trans.*, vol. 64, no. 11, pp. 163–171, Aug. 2014.

[83] J. Kim, S. W. Bedell, and D. K. Sadana, “Multiple implantation and multiple annealing of phosphorus doped germanium to achieve n-type activation near the theoretical limit,” *Appl. Phys. Lett.*, vol. 101, no. 11, p. 112107, Sep. 2012.

[84] E. Simoen, M. Schaekers, J. Liu, J. Luo, C. Zhao, K. Barla, and N. Collaert, “Defect engineering for shallow n-type junctions in germanium: Facts and fiction,” *Phys. Status Solidi A*, p. n/a-n/a, Jul. 2016.

[85] *BSTJ 39: 1. January 1960: Solid Solubilities of Impurity Elements in Germanium and Silicon. (Trumbore, F.A.)*. 1960.

[86] J. Coutinho, C. Janke, A. Carvalho, V. J. B. Torres, S. Öberg, R. Jones, and P. R. Briddon, “Strong compensation of n-type Ge via formation of donor–vacancy complexes,” *Phys. B Condens. Matter*, vol. 401–402, pp. 179–183, Dec. 2007.

[87] H. Y. Fan, W. Kaiser, E. E. Klontz, K. Lark-Horovitz, and R. R. Pepper, “Energy Levels and Photoconductivity in Electron-Bombarded Germanium,” *Phys. Rev.*, vol. 95, no. 4, pp. 1087–1088, Aug. 1954.

[88] E. Vainonen-Ahlgren, T. Ahlgren, J. Likonen, S. Lehto, J. Keinonen, W. Li, and J. Haapamaa, “Identification of vacancy charge states in diffusion of arsenic in germanium,” *Appl. Phys. Lett.*, vol. 77, no. 5, pp. 690–692, Jul. 2000.

[89] S. Schneider and H. Bracht, “Suppression of donor-vacancy clusters in germanium by concurrent annealing and irradiation,” *Appl. Phys. Lett.*, vol. 98, no. 1, p. 14101, Jan. 2011.

[90] A. Chroneos, “Defect engineering strategies for germanium,” *J. Mater. Sci.-Mater. Electron.*, vol. 24, no. 6, pp. 1741–1747, Jun. 2013.

[91] D. Skarlatos, M. Bersani, M. Barozzi, D. Giubertoni, N. Z. Vouroutzis, and V. Ioannou-Sougleridis, “Nitrogen Implantation and Diffusion in Crystalline Germanium: Implantation Energy, Temperature and Ge Surface Protection Dependence,” *ECS J. Solid State Sci. Technol.*, vol. 1, no. 6, pp. P315–P319, Jan. 2012.

[92] C. Thomidis, M. Barozzi, M. Bersani, V. Ioannou-Sougleridis, N. Z. Vouroutzis, B. Colombeau, and D. Skarlatos, “Strong Diffusion Suppression of Low Energy-Implanted Phosphorous in Germanium by N-2 Co-Implantation,” *ECS Solid State Lett.*, vol. 4, no. 6, pp. P47–P50, 2015.

[93] A. Chroneos, R. W. Grimes, and H. Bracht, “Fluorine codoping in germanium to suppress donor diffusion and deactivation,” *J. Appl. Phys.*, vol. 106, no. 6, p. 63707, Sep. 2009.

[94] H. Lee, D. H. Lee, T. Kanashima, and M. Okuyama, “Characteristics improvement of HfO(2)/Ge gate stack structure by fluorine treatment of germanium surface,” *Appl. Surf. Sci.*, vol. 254, no. 21, pp. 6932–6936, Aug. 2008.

[95] C. X. Li, C. H. Leung, P. T. Lai, and J. P. Xu, “Effects of fluorine incorporation on the properties of Ge p-MOS capacitors with HfTiON dielectric,” *Solid-State Electron.*, vol. 54, no. 7, pp. 675–679, Jul. 2010.

[96] R. Xie, M. Yu, M. Y. Lai, L. Chan, and C. Zhu, “High-k gate stack on germanium substrate with fluorine incorporation,” *Appl. Phys. Lett.*, vol. 92, no. 16, p. 163505, Apr. 2008.

[97] R. Xie, W. He, M. Yu, and C. Zhu, “Effects of fluorine incorporation and forming gas annealing on high-k gated germanium metal-oxide-semiconductor with GeO(2) surface passivation,” *Appl. Phys. Lett.*, vol. 93, no. 7, p. 73504, Aug. 2008.

[98] A. Chroneos, B. P. Uberuaga, and R. W. Grimes, “Carbon, dopant, and vacancy interactions in germanium,” *J. Appl. Phys.*, vol. 102, no. 8, p. 83707, Oct. 2007.

[99] C. M. Polley, W. R. Clarke, J. A. Miwa, G. Scappucci, J. W. Wells, D. L. Jaeger, M. R. Bischof, R. F. Reidy, B. P. Gorman, and M. Simmons, “Exploring the Limits of N-Type Ultra-Shallow Junction Formation,” *ACS Nano*, vol. 7, no. 6, pp. 5499–5505, Jun. 2013.

[100] K. Morii, T. Iwasaki, R. Nakane, M. Takenaka, and S. Takagi, “High performance GeO2/Ge nMOSFETs with source/drain junctions formed by gas phase doping,” in *Electron Devices Meeting (IEDM), 2009 IEEE International*, 2009, pp. 1–4.

[101] A. Claverie, S. Koffel, N. Cherkashin, G. Benassayag, and P. Scheiblin, “Amorphization, recrystallization and end of range defects in germanium,” *Thin Solid Films*, vol. 518, no. 9, pp. 2307–2313, Feb. 2010.

[102] R. Duffy, M. Shayesteh, M. White, J. Kearney, and A.-M. Kelleher, “The formation, stability, and suitability of n-type junctions in germanium formed by solid phase epitaxial recrystallization,” *Appl. Phys. Lett.*, vol. 96, no. 23, p. 231909, Jun. 2010.

[103] C. O. Chui, K. Gopalakrishnan, P. B. Griffin, J. D. Plummer, and K. C. Saraswat, “Activation and diffusion studies of ion-implanted p and n dopants in germanium,” *Appl. Phys. Lett.*, vol. 83, no. 16, pp. 3275–3277, Oct. 2003.

[104] C. O. Chui, L. Kulig, J. Moran, W. Tsai, and K. C. Saraswat, “Germanium n-type shallow junction activation dependences,” *Appl. Phys. Lett.*, vol. 87, no. 9, p. 91909, Aug. 2005.

[105] C. Wündisch, M. Posselt, B. Schmidt, V. Heera, T. Schumann, A. Mücklich, R. Grötzschel, W. Skorupa, T. Clarysse, E. Simoen, and H. Hortenbach, “Millisecond flash lamp annealing of shallow implanted layers in Ge,” *Appl. Phys. Lett.*, vol. 95, no. 25, p. 252107, 2009.

[106] G. Thareja, J. Liang, S. Chopra, B. Adams, N. Patil, S.-L. Cheng, A. Nainani, E. Tasyurek, Y. Kim, S. Moffatt, R. Brennan, J. McVittie, T. Kamins, K. Saraswat, and Y. Nishi, “High Performance Germanium N-MOSFET with Antimony Dopant Activation Beyond 1x10(20) cm(-3),” *2010 Int. Electron Devices Meet. - Tech. Dig.*, 2010.

[107] G. Thareja, S. Chopra, B. Adams, Y. Kim, S. Moffatt, K. Saraswat, and Y. Nishi, “High n-Type Antimony Dopant Activation in Germanium Using Laser Annealing for Junction Diode,” *IEEE Electron Device Lett.*, vol. 32, no. 7, pp. 838–840, Jul. 2011.

[108] C. Monmeyran, Y. Cai, R. M. Gwilliam, I. F. Crowe, J. Michel, A. Agarwal, and L. C. Kimerling, “Fluorine and phosporus co-implantation for high electrical activation of n-type germanium,” *In: Program: Symposium EP7: Material and Device Frontiers for Integrated Photonics MRS; 28 March 2016-01 Apr. 2016; Phoenix. MRS; 2016.*, 31-Mar-2016. .

[109] S. Boninelli, G. Impellizzeri, F. Priolo, E. Napolitani, and C. Spinella, “Fluorine in Ge: Segregation and EOR-defects stabilization,” *Nucl. Instrum. Methods Phys. Res. Sect. B-Beam Interact. Mater. At.*, vol. 282, pp. 21–24, Jul. 2012.

[110] G. Impellizzeri, S. Boninelli, F. Priolo, E. Napolitani, C. Spinella, A. Chroneos, and H. Bracht, “Fluorine effect on As diffusion in Ge,” *J. Appl. Phys.*, vol. 109, no. 11, p. 113527, Jun. 2011.

[111] D. J. Sprouster, C. Campbell, S. J. Buckman, G. Impellizzeri, E. Napolitani, S. Ruffell, and J. P. Sullivan, “Defect complexes in fluorine-implanted germanium,” *J. Phys. -Appl. Phys.*, vol. 46, no. 50, p. 505310, Dec. 2013.

[112] S. A. Harrison, D. Yu, T. F. Edgar, G. S. Hwang, T. A. Kirichenko, and S. K. Banerjee, “Origin of vacancy and interstitial stabilization at the amorphous-crystalline Si interface,” *J. Appl. Phys.*, vol. 96, no. 6, pp. 3334–3338, Sep. 2004.

[113] M. Shayesteh, V. Djara, M. Schmidt, M. White, A.-M. Kelleher, and R. Duffy, “Fluorine implantation in germanium for dopant diffusion control,” in *AIP Conference Proceedings*, 2012, vol. 1496, pp. 115–118.

[114] G. Impellizzeri, E. Napolitani, S. Boninelli, J. P. Sullivan, J. Roberts, S. J. Buckman, S. Ruffell, F. Priolo, and V. Privitera, “Role of F on the Electrical Activation of As in Ge,” *Ecs J. Solid State Sci. Technol.*, vol. 1, no. 3, pp. Q44–Q46, 2012.

[115] W.-S. Jung, J.-H. Park, A. Nainani, D. Nam, and K. C. Saraswat, “Fluorine passivation of vacancy defects in bulk germanium for Ge metal-oxide-semiconductor field-effect transistor application,” *Appl. Phys. Lett.*, vol. 101, no. 7, p. 72104, Aug. 2012.

[116] H. a. W. El Mubarek, “Reduction of phosphorus diffusion in germanium by fluorine implantation,” *J. Appl. Phys.*, vol. 114, no. 22, p. 223512, Dec. 2013.

[117] J. R. Weber, A. Janotti, and C. G. Van de Walle, “Dangling bonds and vacancies in germanium,” *Phys. Rev. B*, vol. 87, no. 3, p. 35203, Jan. 2013.

[118] H. G. David Pastor, C. Monmeyran, Y. Cai, R. M. Gwilliam, I. F. Crowe, L. C. Kimerling, J. Michel, A. Agarwal, E. Mazur, and M. J. Aziz, “N Type Doping of Strained Epitaxial Germanium Films Using Ion Implantation Followed by Nanosecond Pulse Laser Melting,” *In: Program: Symposium GG ? Emerging Materials and Platforms for Optoelectronics: MRS; 30 Nov 2015-04 Dec 2015; Boston. MRS; 2015.*, 01-Dec-2015. [Online]. Available: https://www.escholar.manchester.ac.uk/uk-ac-man-scw:281342. [Accessed: 11-Feb-2016].

[119] A. Satta, A. D’Amore, E. Simoen, W. Anwand, W. Skorupa, T. Clarysse, B. Van Daele, and T. Janssens, “Formation of germanium shallow junction by flash annealing,” *Nucl. Instrum. Methods Phys. Res. Sect. B Beam Interact. Mater. At.*, vol. 257, no. 1–2, pp. 157–160, Apr. 2007.

[120] A. Satta, E. Simoen, R. Duffy, T. Janssens, T. Clarysse, A. Benedetti, M. Meuris, and W. Vandervorst, “Diffusion, activation, and regrowth behavior of high dose P implants in Ge,” *Appl. Phys. Lett.*, vol. 88, no. 16, p. 162118, Apr. 2006.

[121] G. Hobler and G. Otto, “Status and open problems in modeling of as-implanted damage in silicon,” *Mater. Sci. Semicond. Process.*, vol. 6, no. 1–3, pp. 1–14, Feb. 2003.

[122] V. Fistul, M. Iglitsyn, and E. Omelyanovskii, “Mobility of Electrons in Germanium Strongly Doped with Arsenic,” *Sov. Phys.-Solid State*, vol. 4, no. 4, pp. 784–785, 1962.

[123] Y. Liu, C. W. Chow, W. Y. Cheung, and H. K. Tsang, “In-line channel power monitor based on helium ion implantation in silicon-on-insulator waveguides,” *IEEE Photonics Technol. Lett.*, vol. 18, no. 17, pp. 1882–1884, Sep. 2006.